Development of non-invasive MRI to measure water permeability across the blood-brain interface

Yolanda Ohene

A thesis presented in partial fulfilment of the requirements for the degree of Doctor of Philosophy to

University College London

Centre for Advanced Biomedical Imaging

Division of Medicine

University College London

This thesis is dedicated, in loving memory, to Barbara Baddoo

Declaration

‘I, Yolanda Ohene confirm that the work presented in this thesis is my own. Where information has been derived from other sources, I confirm that this has been indicated in the thesis.’

Abstract

The blood-brain interface (BBI) is a physical and biochemical barrier that protects and maintains healthy brain function. Disruption of the BBI is indicative of the early stages of certain neurodegenerative diseases, such as Alzheimer’s Disease. However, there is currently a lack of sensitive tools available to accurately quantify the early alterations to the integrity of the BBI.

This thesis describes the development and implementation of multiple echo time arterial spin labelling (multi-TE ASL) MRI technique in the mouse brain to measure vascular water permeability across the BBI. The technique was implemented in two high-field MRI system to demonstrate the consistency of the imaging protocols and the sensitivity of the measures of BBI water permeability.

The multi-TE ASL technique was used to probe the function of aquaporin-4 (AQP4) water channels, which play a key role in the clearance of the deleterious proteins from the brain. This non-invasive technique was able to demonstrate its sensitivity to targeting AQP4 by measuring a 31% slowing of cortical BBI water permeability with the removal of the AQP4 water channels. The technique also measured a 34% slowing in the BBI water permeability in the cerebellum brain region with a reduction of AQP4 channels at the BBI.

Finally, the technique measured a 32% increase in cortical BBI permeability to water in a mouse model of ageing. The non-invasive imaging measurements were associated with a 2-fold increase in mRNA expression of pericytes, while other BBI markers such as tight junction proteins were maintained.

Overall, this work has demonstrated the scope of novel MRI technique to target changes to BBI water permeability, with potential for clinical translation for the early detection and understanding of neurodegenerative disease.

Impact Statement

The increasing prevalence of neurodegenerative diseases in our ageing population means that dementia is now one of the biggest healthcare problems of our time. A major limitation for understanding dementia is that there are insufficient biomarkers that are able to distinguish neurodegenerative pathology at an early stage of the disease. This thesis is dedicated to the development of a non-invasive MRI technique to measure water permeability across the blood-brain interface, and the assessment of its sensitivity to several biological mechanisms that are associated with ageing and neurodegenerative diseases.

The work presented in this thesis will have direct benefit to academic centres (both national and international) that are working on understanding the basic mechanisms of early changes that occur in neurodegenerative disease. Furthermore, the successful clinical translation of this MRI technique could form a valuable tool for clinical diagnosis of Alzheimer's Disease. A collaboration with the University of Auckland has arisen from this work, and we now are beginning to use this technique to assess potential changes in patients with Mild Cognitive Impairment. Overall, the data presented in this thesis proposes a novel imaging tool that may be an early detection technique for neurodegenerative diseases.

Acknowledgements

I never thought that I could write an entire thesis, but here it is, and it couldn't have done it without the many incredible people in my life.

First of all, I can't thank my supervisor, Jack Wells, enough. He has taught me basically everything that I know, as well as being so kind, light-hearted and inspiring throughout this PhD journey. Much thanks go to, Mark Lythgoe, who taught me to be bold and to find the story within the science. I am sincerely grateful to Dave Thomas, who has such deep insight into all of this work, thank you for pushing my thinking. Thank-you all for your time and belief in me as a budding scientist.

I have spent a big part of my PhD doing science communication and outreach events and without Oz Ismail and Heather Fitzke, this wouldn't have been the same. You two have truly inspired me to think about science in ways that I had never considered before, as well as being unwavering emotional support throughout the PhD. I would like to thank the Alzheimer's group at Cabi for all the support over the years. Especially, Ian Harrison who introduced me to biology (and stats!), to Payam Nahavandi, my classmate, and Phoebe Evans for our early morning breakfasts and MAC stop-offs at the airports. And to the rest Cabi, past and present, for being such a special lab with a special shout out to Tammy Kalber, Tom Roberts, Laurence Jackson, Val Taylor, and everyone who has ever brought me or a snack in the scan room or a drink at the pub.

The PhD CDT lunch crew at UCL, Mikael, Aaron and Lizzie, have been there through it all with our shared successes and sufferings. You lot brought the light back into perspective of that dark tunnel. And I must holla to all the bros and gals in the Minorities in STEM network, who have made me feel like there is a room for me in the scientific arena.

I can’t put into words how much my friends mean to me. My best pals, Lauren, Emma and Beth, thank you for trying to keep me grounded, making me laugh and still being there through thick and thin all of these years. The other members of ASOC, Blane and Sarah, who know when to crack out the wine. To Fi, Jess and Rose for being lovely humans. I stand shoulder to shoulder with the Imperial lads: Carmen BP, Alice Jacques, Amy Hughes and Jess Spake, who never fail to inspire, support and encourage me. And to my adopted sister, Holly Farrer. I salute you all.

And finally, to the outspoken and outrageous Ohene famalan, I really couldn’t have done it without you. Huge love to my sisters, Maz and Lil L, who just keep.me.fierce. Quite honestly, I don’t know how our parents have put up with us for all of these years. But most of all, thank you, Muv and Dad for your unwavering support. You taught us to believe that we could do whatever we dreamed of, and then never stopped believing in it too.

Publications

<u>Y. Ohene</u>, I.F. Harrison, O. Ismail, P. Nahavandi, P.G. Evans, O.P. Ottersen, E.A. Nagelhaus. D.L. Thomas, M.L Lythgoe, J.A Wells. Increased blood-brain interface permeability to water in the ageing brain detected using non-invasive multi-TE ASL. *Under preparation.*

P.G. Evans, M. Sokolska, A. Alves, I.F. Harrison, **<u>Y. Ohene,</u>** P. Nahavandi, O. Ismail, E. Miranda, M.L. Lythgoe, D.L. Thomas, J.A. Wells. Non-invasive MRI of Blood-Cerebrospinal Fluid Barrier Function. Nature Communications. *Under review.*

I.F. Harrison, O. Ismail, A. Machhada, N. Colgan, J.A. Wells, **<u>Y. Ohene</u>**, P. Nahavandi, Z. Ahmed, A. Fisher, S. Meftah, T.K. Murray, R.A. Johnson, E.C. Collins, M.J. O'Neill, M.F. Lythgoe. Impaired Glymphatic Function and Clearance of Tau in an Alzheimer's Disease Model. Brain. *Submitted.*

<u>Y. Ohene</u>, I.F. Harrison, O. Ismail, P. Nahavandi, E.V. Bird, O.P. Ottersen, E.A. Nagelhaus. D.L. Thomas, M.L. Lythgoe, J.A. Wells. Non-invasive assessment of brain clearance pathways using multi-echo time arterial spin labelling: An Aquaporin-4 Study. NeuroImage (2019); **188**.

I.F. Harrison, B. Siow, A.B Akilo, P.G. Evans, O. Ismail, **<u>Y. Ohene,</u>** P. Nahavandi, D.L. Thomas, M.L. Lythgoe, J.A. Wells. Non-invasive imaging of CSF-mediated brain clearance pathways via assessment of perivascular fluid movement with diffusion tensor MRI. e-Life 2018; **7**:e34028.

Conference Proceedings & Awards

October 2019 **Jocelyn Bell Burnell Medal and Prize, Institute of Physics**

The work of this thesis, along with the contribution made to encouraging other into physics, has been awarded the Jocelyn Bell Burnell Medal 2019 for exceptional early career contribution to physics by a female physicist.

July 2019 Regional Assessment of Aquaporin-4 Polarisation dependent vascular water permeability mouse brain using non-invasive multi-echo time arterial spin labelling MRI.
Y. Ohene, I.F. Harrison, O. Ismail, P. Nahavandi, P. Evans, E.V Bird, O.P. Ottersen, E.A. Nagelhaus. D.L. Thomas, M.L. Lythgoe, J.A. Wells. BRAIN & BRAIN PET 2019, Yokahoma, Japan. Poster Presentation.
Award: Early Careers Investigator Award

May 2019 Regional Variation of Water Permeability at the Blood-Brain Interface in the Mouse Brain using Multi-TE ASL – The Role of Aquaporin-4.
Y. Ohene, I.F. Harrison, O. Ismail, P. Nahavandi, P. Evans, E.V Bird, O. P. Ottersen, E.A. Nagelhaus. D.L. Thomas, M.L. Lythgoe, J.A. Wells. ISMRM 19, Montreal, Canada. Power Pitch & Poster Presentation.

April 2019 Increased Blood-Brain Barrier Permeability to Water in a Mouse Model of Ageing using non-invasive Multiple Echo Time Arterial Spin Labelling.
Y. Ohene, I.F. Harrison, O. Ismail, P. Nahavandi, P. Evans, D.L. Thomas, M.L. Lythgoe, J.A Wells. Postgraduate Symposium BC-ISMRM, Birmingham. Oral Presentation.
Award: Best Oral Presentation

July 2019 Non-invasive Imaging of Brain Waste Clearance Pathways using Multiple Echo Time ASL: An Aquaporin-4 Study.
Y. Ohene, I.F. Harrison, O. Ismail, P. Nahavandi, E.V. Bird, O.P. Ottersen, E.A. Nagelhaus. D.L. Thomas, M.L. Lythgoe, J.A. Wells. Alzheimer's Association International Conference, Chicago, USA. Poster Presentation. Alzheimer's Imaging Consortium, Oral Presentation.
Award: Best Oral Presentation (Alzheimer's Imaging Consortium)

June 2018 Non-invasive Imaging of Brain Clearance Pathways using Multiple Echo Time ASL: An Aquaporin-4 Study.

Y. Ohene, I.F. Harrison, O. Ismail, P. Nahavandi, P. Evans, E.V Bird, O.P. Ottersen, E.A. Nagelhaus. D.L. Thomas, M.L. Lythgoe, J.A. Wells. ISMRM 2018, Paris, France. e-Poster Presentation

Award: Best ASL Poster, Perfusion Study Group

March 2018 Non-invasive Imaging of Brain Waste Clearance Pathways using Multiple Echo Time ASL: An Aquaporin-4 Study. Alzheimer's Research UK, London, UK. Power pitch & poster presentation

Y. Ohene, I.F. Harrison, O. Ismail, P. Nahavandi, E.V. Bird, O.P. Ottersen, E.A. Nagelhaus. D.L. Thomas, M.L Lythgoe, J.A Wells.

Award: David Darwin Best Poster Prize

September 2017 Characterising Blood-Brain Permeability to Water in Mouse brain using Multiple Echo Time Arterial Spin Labelling

Y. Ohene, I.F. Harrison, O. Ismail, P. Nahavandi, D.L. Thomas, M.L Lythgoe, J.A Wells. . BC-ISMRM 2017, Liverpool. Oral Presentation.

Award: 2nd Best Oral Presentation

June 2017 Characterising Blood-Brain Permeability to Water in Mouse brain using Multiple Echo Time Arterial Spin Labelling.

Y. Ohene, I.F. Harrison, O. Ismail, P. Nahavandi, D.L. Thomas, M.L Lythgoe, J.A Wells. Imaging Cerebral Physiology 2017, Cardiff, UK. Poster Presentation.

April 2017 Non-invasive Assessment of Vascular Water Permeability in the Mouse Brain using multi-TE ASL.

Y. Ohene, I.F. Harrison, O. Ismail, P. Nahavandi, D.L. Thomas, M.L Lythgoe, J.A Wells. ISMRM 2017, Honolulu, U.S.A. Oral Presentation.

March 2017 Characterising Blood-Brain Permeability to Water in Mouse brain using Multiple Echo Time Arterial Spin Labelling.

Y. Ohene, I.F. Harrison, O. Ismail, P. Nahavandi, D.L. Thomas, M.L Lythgoe, J.A Wells. Postgraduate symposium BCISMRM 2017, London. Oral Presentation.

Award: Best Oral Presentation

Selected Science Communication talks arisen from this work

October 2019

Body Imaging by Number, Maths Inspiration, St Swithun's School, Winchester

August 2019

Finding My Inner Selfie, The Omni Tent, GreenMan festival, Wales

June 2019

Being an imaging scientist, St. Saviour & St Olaves School, London

February 2018

Imagining the invisible, King Soloman Academy, London

December 2017

BBC Tomorrow's World Live, Glasgow Science Museum, Glasgow

October 2017

UCL Institute of Healthcare Engineering, New Science Live, London

August 2017

Imaging the Universe, Wilderness Festival, Oxfordshire

July 2017

Brainwash Live, Cheltenham Science Festival, Cheltenham

June 2017

Brain Food, Gayhurst Primary School, London

July 2016

Brain Control Live, Cheltenham Science Festival, Cheltenham

Table of Contents

Chapter 1

Chapter 2

Chapter 3

Chapter 4

Chapter 5

Chapter 6

Chapter 7

Index of Figures

Figure 1.1: Schematic of the neurovascular unit (NVU). The NVU consists of endothelial cells held together by tight junctions and adherens junctions, next to the basal lamina (also referred to as the basement membrane), surrounded by pericytes and astrocytes, neurons and microglial.

Figure 1.2: Healthy and diseased blood-brain interface. Schematic of a healthy BBI (left) with the endothelium, basement membrane, pericytes, brain extracellular space (ECS) and astrocytes that maintain the transport of vital molecules into the brain parenchyma. The disrupted BBI in diseased condition (right), shows breaks in the endothelium, degrading and detachment of the pericytes and astrocytes, which prevents the normal distribution of molecules into the brain tissue.

Figure 1.3: Disruptive and non-disruptive changes that occur at the blood-brain interface. Schematic of disruptive changes to the BBI (left) such as tight junction deterioration, endothelial damage and breakdown of the glial limitans (GL) and non-disruptive changes to the BBI (right) such as changes to transporters and receptors and changes to the enzymes and astrocytes.

Figure 1.4: Goldmann's Trypan Blue Injection experiments. **A.** 1st experiment – adult rat following a systemic injection of trypan blue solution. **B.** 2nd experiment – brain and spinal cord of adult rat following lumbar subarachnoid injection.

Figure 2.1: Schematic of FAIR Labelling Scheme. **A.** Position of the imaging slice in the mouse brain in this work. **B.** Control image generated from a non-selective global inversion pulse **C.** Labelled image generated from a slice selective inversion in the region of the image slice.

Figure 2.2: Relaxation rates. T_1 recovery, is the longitudinal relaxation and T_2 decay is the transverse relaxation that occurs simultaneously but, *in-vivo*, T_2 is much faster than T_1.

Figure 2.3: Schematic for the approximate timescales for the ASL imaging and physiological parameters, where δ_a is arterial transit time, δ is tissue transit time, τ is temporal width of the tagged bolus and TI is inflow time (selected for each imaging protocol).

Figure 2.4: Flowchart for the analysis pipeline to determine exchange time (T_{ex}^{w}) from multi-TE ASL data, multi-TI ASL data and control data.

Figure 2.5: Effect of air mixture on T2$_{app}$. **A.** Oxygen saturation level in air mixture conditions: 1.0ml/min medical air and 1.0ml/min oxygen **B.** Apparent transverse

relaxation $T2_{app}$ and **C.** extravascular tissue transverse relaxation ($T2_{EV}$), for individual animals breathing two air mixtures with mean value and associated error (± std) indicated on plot.

Figure 2.6: Modelling the multi-TE ASL signal. **A.** Representative $T2_{app}$ map at increasing inflow times (indicated on each image) for a single subject, with an anatomical reference image shown with cortical ROI in red, for illustration purposes. **B.** $T2_{app}$ at increasing inflow times fitted to single compartment model for individual subjects, $p = 0.003$. **C.** The mean cortical signal across all subjects fitted to the two-compartment model at TI = 1000ms and 1500ms. **D.** The intravascular fraction of the ASL signal determined for the individual subjects at TI = 1000 ms and 1500 ms using the two-compartment model. The mean parameter and associated error (± std) are displayed with each marker representing the individual animals. *** indicates $p < 0.001$.

Figure 2.7: Modelling ASL signal at short inflow times. **A.** The normalised mean cortical signal across all subjects fitted to a linear model with mean value and associated error (± std) displayed. **B.** Representative arterial transit time (δ_a) map for an individual subject. **C.** Representative cerebral blood flow (CBF) map for an individual subject. Respective scale bars are displayed.

Figure 2.8: Lookup table for predicted intravascular fraction plotted as a function of water exchange rate (K_w)/ min^{-1} generated for PASL sequence.

Figure 3.1: Schematic of ASL labelling scheme and labelled blood water transfer from intravascular space to extravascular tissue space. **A.** Labelled blood water molecules exchange into the extravascular space via all water transport mechanisms including aquaporin-4 (AQP4) water channels in wild-type (WT) mice. **B.** In the absence of AQP4, in AQP4-deficent mice (*Aqp4*$^{-/-}$), the water transport mechanisms are restricted and only occur through cotransport with organic molecules and by diffusion through the lipid bilayer of the plasma membrane.

Figure 3.2: Time of exchange of labelled blood water into cortical tissue. **A.** Average exchange time maps for all animals (scale bar shown) and an anatomical reference of the cortical brain region for individual analysis, for illustration purposes. **B.** The mean cortical exchange time measurements for individual animals. **C.** Mean cortical arterial transit time (δ_a) for individual animals. **D.** Mean cortical CBF for individual animals **E.** Mean cortical ADC measured in individual animals. Group mean parameter and associated error (± std) are displayed on each plot, (n=9). * indicates $p < 0.05$.

Figure 3.3: Cortical *Aqp4* mRNA expression of wildtype (WT) and *Aqp4*$^{-/-}$ mice. Normalised to the WT cortex (n = 3 in each group).

Figure 4.1: Analysis Pipeline for Exchange Time (T_{ex}^{w}) measurements. Step-wise approach for calculating the intravascular fraction and the exchange time from the ASL data.

Figure 4.2: Example of ASL images acquired a representative animal using the 9.4T Bruker at increasing echo time (indicated on images) with the optimised imaging parameters.

Figure 4.3: ASL signal decay from the two 9.4T imaging systems. **A.** Mean ASL signal fitted to bi-exponential model for the optimised 9.4T Agilent system imaging protocol (n = 5) and the 9.4T Bruker system imaging protocol (n = 5). **B.** Intravascular fraction for individual animals at inflow time (TI) = 1500 ms. The mean value and the associated error (± std) are displayed on both plots. NB. In some cases the error bars may not be visible they are very small.

Figure 4.4: Stability of the ASL signal decay. The mean/ standard deviation (μ/σ) of the ASL signal across the repetitions for the individual animals with the mean and the associated error displayed for both of the imaging systems.

Figure 4.5: Example of poor quality ASL images. This is an example of ASL data containing artefacts with a low stability (μ/σ).

Figure 4.6: ASL signal decay for the cortical region and the cerebellar brain region at inflow times, TI = 800 ms and TI = 1500 ms, with the mean parameter and the associated error indicated in the plot with the mean values and the associated errors (± std) (n = 5).

Figure 4.7: Multi-TE ASL in cortical and cerebellar brain regions. **A**. Intravascular fractions maps for cortical and cerebral slice of the mouse brain with inflow times indicated for each image, and anatomical reference image with ROI in red. **B.** Intravascular fraction derived from the cortical and cerebellar brain regions for individual subjects at inflow times TI = 800 ms and 1500 ms. The mean parameter and associated error (± std) are displayed. * indicates $p < 0.05$.

Figure 4.8: BBI Permeability to water and perfusion in cortical and cerebellar brain regions. **A.** Exchange time measurements and **B.** Cerebral blood flow (CBF) measurements in the cortical and cerebellar regions for individual animals with the mean value and the associated error (± std) indicated on each of the plot.

Figure 4.9: *Aqp4* mRNA expression from paired cortical and cerebellar brain regions of C57/Bl6 WT mice (n = 6). ** indicates $p < 0.01$.

Figure 4.10: Schematic of Pulse Sequence **A.** Flow-alternating inversion recovery (FAIR) sequence for single echo time**. B.** FAIR-T2-EPI sequence with multiple echo time acquisition displaying timings including: inflow time (TI), echo time (TE) and repetition time (TR), radio-frequency (RF) pulses and gradients: slice selective (G_{SS}), phase encoding (G_{PE}) and readout (G_{RO}).

Figure 4.11: Simulated FAIR-T2-EPI sequence. Radiofrequency (RF) pulses (in red) for non-selective and selective inversion and for spin echoes, slice selective gradient (blue), phase encode gradient (red) and readout gradient (green) with sequence parameters: TI = 100ms; TR = 1156ms; Echo Spacing = 20ms; Echoes = 5. Bottom inset: magnification of the RF pulses with flip angle indicated and magnetic gradients demonstrating the multiple echo acquisition.

Figure 4.12: $T2_{app}$ measurements from FAIR-T2-EPI sequence. ASL images at increasing echo time (marked on images) for calculation of $T2_{app}$ maps (right) for the same animal at **A.** TI = 800ms **B.** TI = 1500ms. ASL signal, for individual repetitions with mean value marked on plot, derived from the cortical region of interest for quantitative measurement of $T2^{app}$ at **C.** TI = 800ms **D.** TI = 1500ms with the red line to indicate the mono-exponential fitting.

Figure 5.1: Anchoring of the AQP4 molecule to the perivascular location. **A.** The dystrophin-associated protein complex (DAPC) consisting of α-Syntrophin (α-Syn), α-dystrobrevin (α-DB), 71kD isoform of dystrophin (DP71), β-dystroglcan (β-DG) and α-dystroglycan (αDG), the AQP4 interacts directly or indirectly with the PDZ domain of α-syntrophin. **B.** Wild-type (WT) mouse and **C.** α-syntrophin KO (*Syn*$^{-/-}$) mouse of brain slice from the hippocampus demonstrating perivascular AQP4 immunogold labelling (black circles) in with the arrow indicating the membrane abutting the endothelium (end), the capillary lumen (L) and part of the pericytes (colored green with asterisk).

Figure 5.2: ASL images with severe artefacts that were excluded from the final analysis for **A.** Cortical slice and **B.** Cerebellar slice from a representative animal.

Figure 5.3: ASL signal decay and intravascular fraction of cortical brain region. ASL signal decay at TI = 800 ms and 1500 ms at increasing echo time for **A.** Wild-type (WT) mice and **B.** α-syntrophin-deficient mice (*Syn*$^{-/-}$). **C.** Intravascular fraction for individual animals at inflow times (800 ms and 1500 ms) with mean value and associated error (± std) indicated on the plots.

Figure 5.4: ASL signal decay and intravascular fraction of cerebellum brain region. ASL signal decay at TI = 800 ms and 1500 ms at increasing echo times for **A.** Wild-type (WT) mice and **B.** α-syntrophin-deficient (*Syn*$^{-/-}$) mice **C.** Intravascular fraction for individual animals at inflow times (800 ms and 1500 ms). The mean values and associated error (± std) are displayed on the plot.

Figure 5.5: Exchange Time measurements from the cortical and cerebellum brain region. **A.** Exchange time maps of the cortex and the cerebellum in a representative wild-type (WT) and α-Syntrophin-deficient (*Syn*$^{-/-}$) mice, with an anatomical image on left (with ROI shown in red). **B.** Mean exchange time measurements in individual WT *and Syn*$^{-/-}$ mice in cortical and cerebellar brain regions**.** ** indicates $p < 0.01$.

Figure 5.6: Cerebral haemodynamics in the cortical and cerebellum brain regions. **A.** Arterial transit time measurements for individual WT and *Syn*$^{-/-}$ mice and **B.** Cerebral blood flow (CBF) measurements for cortex and cerebellum brain regions of the WT mice and *Syn*$^{-/-}$ mice. All plots display the mean parameter and associated error (± std). * indicates $p < 0.05$.

Figure 6.1: Analysis pipeline for exchange time (T_{ex}^{w}) calculation. Stepwise process outlining the modelling process using the ASL data to measure the exchange time (T_{ex}^{w}), from a defined region of interest, using the adapted two compartment kinetic perfusion model and the arterial transit time measurements.

Figure 6.2: Mean cortical ASL signal intensity decay as a function of TE for the adult (blue) and aged (grey) across all mice **A.** TI = 800ms and **B.** TI = 1500ms. C. The intravascular fraction ($\Delta M_{IV} / \Delta M_{IV} + \Delta M_{EV}$) determined for the individual animal at both inflow times, mean and error (± std) and p-values are indicated on the plots.

Figure 6.3: Cortical region measurements. **A.** Exchange time maps from a representative adult and aged mice, with an anatomical reference image on the left with the cortical ROI in red. **B.** Cortical exchange time measurements. **C.** Cortical arterial transit time measurements **D.** Cortical cerebral blood flow (CBF) measurements. Each plot shows individual animal measurements along with mean values and the associated error (± std). * indicating $p < 0.05$.

Figure 6.4: Intravascular T2 ($T2_{IV}$) measurements for individual mice at inflow times, 800 ms and 1500 ms **A.** Adult mice **B.** Aged mice. * indicates $p < 0.05$.

Figure 6.5: Cortical mRNA expression of aquaporin-4 (*Aqp4*), α-syntrophin protein (SNTA1), platelet derived growth factor receptor- β (PDGFRβ), occludin (*Occl*) and Claudin-5 (*Cld5*) with mean values and associated error (± std) displayed as fold change from the cortical region of the adult mice is shown on the plot. * indicates $p < 0.05$ for the adjusted p values.

Figure 6.6: Mean cerebellar ASL signal intensity decay as a function of TE for the adult (blue) and aged (grey) across all mice, at inflow times: **A.** TI = 800ms and **B.** TI

= 1500ms **C.** The intravascular fraction (ΔM_{IV} / ΔM_{IV} + ΔM_{EV}) determined for the individual animal at both inflow times, mean and error (± std) and p values are indicated on the plots.

Figure 6.7: Cerebellum measurements. **A.** Exchange time maps for representative adult and aged mice with anatomical reference on left with ROI in red **B.** Exchange time measurements for individual adult mice and aged mice. **C.** Arterial transit time measurements for individual adult and aged mice **D.** Cerebellar CBF measurements for the individual adult and aged mice. For all plots, the mean value and the associated error (± std) are shown on plot. ** indicates $p < 0.01$.

Figure 6.8: Cerebellar mRNA expression of aquaporin-4 (*Aqp4*), α-syntrophin protein (*SNTA1*), platelet derived growth factor receptor-β (*PDGFR-β*), occludin (*Occl*) and Claudin-5 (*Cld5*) in the individual adult mice and aged mice with mean values and associated error (± std) displayed as fold change from the cerebellar region of the adult mice is shown on the plot. * indicates $p < 0.05$ for adjusted p-values.

Chapter 1

Introduction

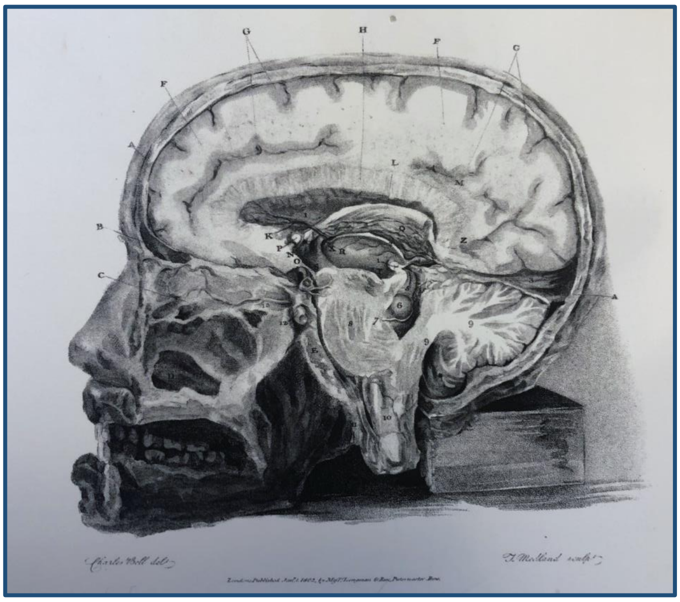

The human brain, Sir Charles Bell

Introduction

The blood-brain interface (BBI) is a physical and biochemical barrier that protects and regulates the brain from the molecules and nutrients in the blood. The BBI is compromised in several pathologies, which alters the cerebral homeostasis and can lead to many deleterious neurological conditions. Brain tumours cause the vasculature to become tortuous and leaky and disrupts the integrity of the BBI. Multiple sclerosis (MS) is characterised by inflammation and the transient appearance of white matter lesions which affect the BBI during the different stages of disease progression. The onset of ischemic stroke induces disruption of the BBI that contributes to the development of brain injury, subsequently leading to neurological impairment. These are just some of the pathologies that can induce gross disruption to the integrity of the BBI.

In recent years, it has been increasingly recognised that BBI dysfunction is also an important feature of many neurodegenerative conditions; but it manifests as subtle and diffuse changes to the BBI relative to that observed in the conditions described above [1-5]. The number of people who are currently affected by dementia is 50 million worldwide, and this number is expected to triple by 2050, which would make it the largest global healthcare problem of our time [6]. Consequently, there is a pressing need to be able to detect and better understand the biological mechanisms behind the subtler alterations that occur at the BBI in neurodegenerative disorders.

A major limitation in our understanding of dementia is that there are insufficient biomarkers that are able to distinguish neurodegenerative pathology at an early stage of the disease [7, 8]. However, there is increasing evidence to suggest that BBI dysfunction is expected to occur early in the pathogenesis of neurodegenerative diseases [2, 9-11]. Hence, developing sensitive tools to probe changes to the BBI could be especially important as a potential target for therapeutic interventions. There are many technical challenges that hinder the development of techniques able to probe more subtle changes to the BBI that occur in neurodegenerative conditions. Thus, the work in this thesis aims to develop and implement a novel MRI technique that might be sensitive to early changes at the BBI.

1.1 Blood-Brain Interface Permeability in the healthy brain and in disease

1.1.1 Components of the Blood-Brain Interface

The neurovascular unit (NVU) consists of the cerebral microvascular endothelium, astrocytes, pericytes, neurons and the extracellular matrix. Its healthy function is vital to maintain homeostasis in the central nervous system (CNS), **Figure 1.1**. The blood-brain interface (BBI) encompasses the blood-brain barrier (BBB), which includes the endothelial cells and the basement membrane, and also the surrounding pericytes and the endfeet of astrocytes. All of the components of the BBI play a role in the regulation of the vital molecules that are able to pass to and from the blood and into the brain parenchyma to maintain homeostasis of the brain.

Regulation of the BBI is maintained by the tight-junctions (TJ) and adherens junctions that seal together the endothelial cells, the pericytes that surround the endothelium and basement membrane, and the astrocytic endfeet that maintain the barrier with the microglia that protect neuronal cells from cytotoxic stress, **Figure 1.2** (left). Changes to the barrier function can be characterised by many features including reduced TJ integrity holding together the endothelium, disruption to the basement membrane, dysfunction or detachment of pericytes, impaired transport functions, loss of astrocytes or swollen end-feet, **Figure 1.2** (right). The physical disruption can be coupled with, or triggered by, oxidative stress at the BBI causing an immune response which can lead to further damage to the BBI [12]. Each of the components can potentially contribute to alterations in BBI permeability, altering the well-regulated flux of molecules across the BBI, which can be indicative of disease [13].

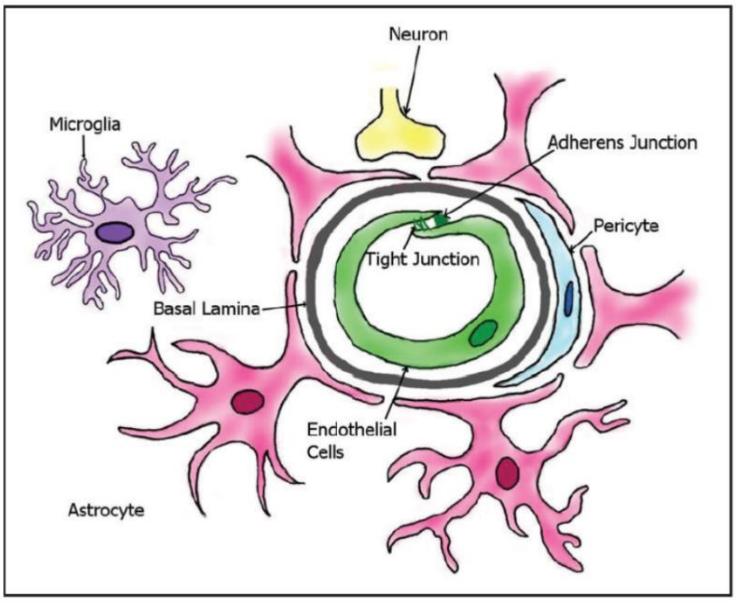

Figure 1.1: Schematic of the neurovascular unit (NVU). The NVU consists of endothelial cells held together by tight junctions and adherens junctions, next to the basal lamina (also referred to as the basement membrane), surrounded by pericytes and astrocytes, neurons and microglial. Source: [14].

The endothelial cells are held together by TJs and junction adhesion molecules (JAMs). The transmembrane TJ proteins make the endothelial cell membrane in the brain distinct from the other cell membranes across the body, as they selectively restrict the paracellular diffusion of molecules from the blood into the brain tissue. Occludin was the first TJ protein to be identified. It is thought to be involved in the regulation of paracellular permeability, though much of its specific barrier function remains elusive [15, 16]. Claudin-5 is the most abundantly expressed protein of the claudin family, and forms a mechanical link between individual endothelial cells to maintain the structural integrity of the vasculature [17]. There are numerous studies indicating that degradation of TJs, particular claudin-5, causes leakage of small molecules from the blood, into the brain [18, 19]. Many studies attribute an increase in BBI permeability to a breakdown of the TJs as they serve a key function for maintaining the regulation of the molecules passing into the brain tissue. However, there are also other mechanisms, cell types and molecular transports that will have an impact on BBI permeability.

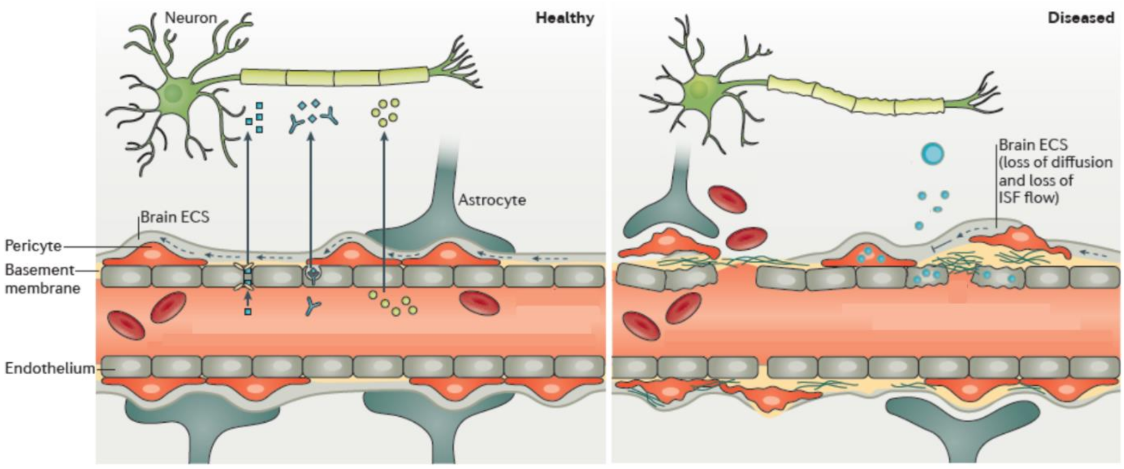

Figure 1.2: Healthy and diseased blood-brain interface. Schematic of a healthy BBI (left) with the endothelium, basement membrane, pericytes, brain extracellular space (ECS) and astrocytes that maintain the transport of vital molecules into the brain parenchyma. The disrupted BBI in diseased condition (right), shows breaks in the endothelium, degrading and detachment of the pericytes and astrocytes, which prevents the normal distribution of molecules into the brain tissue. Schematic adapted from: [20].

Pericytes surround the endothelium cells and form a further physical barrier to molecules transferring from the blood into the extracellular space. Pericytes are contractile cells that are responsive to their environment and react to the changes in the cerebrovasculature. Pericytes are a vital requirement for the development of BBI integrity and contribute to TJ formation during embryogenesis [21]. The genetic removal of pericytes in mice is fatal, which further highlights the critical role of these cells [21]. There is increasing evidence to suggest that pericytes play a key role in causing changes to BBI permeability which can trigger or exacerbate the development of certain neurodegenerative disease [22-24].

The endfeet of astrocytes lie next to the extracellular space (ECS) and are another important component for the regulation and function of the BBI [25]. Aquaporin-4 (AQP4) water channels reside at astrocytic endfeet to facilitate the bi-directional transport of water across the BBI [26]. The discovery of the aquaporin water channel family by Peter Agre in 1991 has significantly furthered our knowledge about water permeability in biological membranes [26]. AQP4 are the most abundant of the water channels within the brain. They are found to cover approximately 50% of the surface area of the endfeet of astrocytes at the BBI, noting that astrocytic endfeet cover 99% of the surface area of vasculature [27, 28].

AQP4 channels are selective specifically to water molecules, and they allow the rapid transfer of water into the brain parenchyma when the water has passed through the endothelium and basement membrane. The rate of transfer of the water molecules through the AQP4 is significantly faster than when water molecules are crossing the BBI via diffusion alone [29, 30]. This provide a unique pathway ‘of least resistance’ for water molecules which has been demonstrated to be important in pathological situations such as cytotoxic or vasogenic brain edema, where the absence of AQP4 water channel can, respectively, have a protective or deleterious outcome [31, 32].

The development of AQP4 knockout (*Aqp4*$^{-/-}$) mice has improved our understanding about the role of AQP4 in the healthy brain and in disease [33]. *Aqp4*$^{-/-}$ mice have been successfully developed, with slight phenotype variations due to the different genetic strategies for deleting AQP4, in three laboratories: Verkman’s group at the University of San Francisco [34], Hu’s group at Nanjing Medical University [35] and by Ottersen and Nagelhus’ group at The University of Oslo [36]. The Nanjing group *Aqp4*$^{-/-}$ mice show disruption to the integrity of the BBI, so careful interpretation of BBI studies using this particular knockout is recommended [37]. Generally, *Aqp4*$^{-/-}$ mice have a relatively subtle phenotype with an intact BBI [36]. To date, the phenotype of *Aqp4*$^{-/-}$ mice has only been evident in pathophysiological conditions, such as induced meningitis or brain edema [38, 39]. But, nonetheless, these studies highlight that AQP4 channels are vital for maintaining water homeostasis in the brain, as the removal of these channels can have deleterious consequences.

Taken together, the BBI consists of several vital cells, in addition to molecular and water transporters, to protect the brain parenchyma from molecules in the blood and maintain the homeostasis of the brain tissue. The BBI is tightly regulated to maintain a healthy brain. However, there are many external as well as biological factors that can cause alterations to the components of the BBI, making the brain susceptible to dysfunction which could lead to devastating pathology.

1.1.2 Blood-Brain Interface function in neurodegenerative disease

Barrier dysfunction can either be disruptive, where a physical anatomical alteration has occurred such as TJ breakdown or endothelium cell damage, or non-disruptive, where there is a change in function of the cells, transporters or receptors without any gross structural changes, **Figure 1.3**. Both cases can induce a pathological change to the function of the NVU, and can lead to increasing the brain's vulnerability to disease [40-42]. Experimental methods designed to investigate changes to the barrier function are usually sensitive to either disruptive or non-disruptive changes. Disruptive changes can be easier to detect as there are many well established techniques, such as a biochemical test of the cerebrospinal fluid (CSF) or dynamic contrast enhanced magnetic resonance imaging (DCE-MRI), that are able to assess the ingress of endogenous or exogenous molecules into the brain parenchyma. Assessment of non-disruptive changes currently use immunohistological techniques, targeted approaches to specific molecular transporters or radioactive probes [43, 44].

As previously mentioned, there are many neurological diseases that will cause changes to the BBI including traumatic brain injury (TBI), brain edema, stroke, brain tumour and MS. Gross disruption to the BBI is often found in these conditions, and alterations to BBI permeability can be detected using several existing techniques that will be described later in this chapter. It is thought that changes to BBI permeability in neurodegenerative disease, such as Alzheimer's Disease (AD), are an order of magnitude smaller than the permeability change detected in stroke [5] or brain tumours [4]. Therefore, there is a need for more sensitive biomarkers to be able to detect these subtle and potentially early changes.

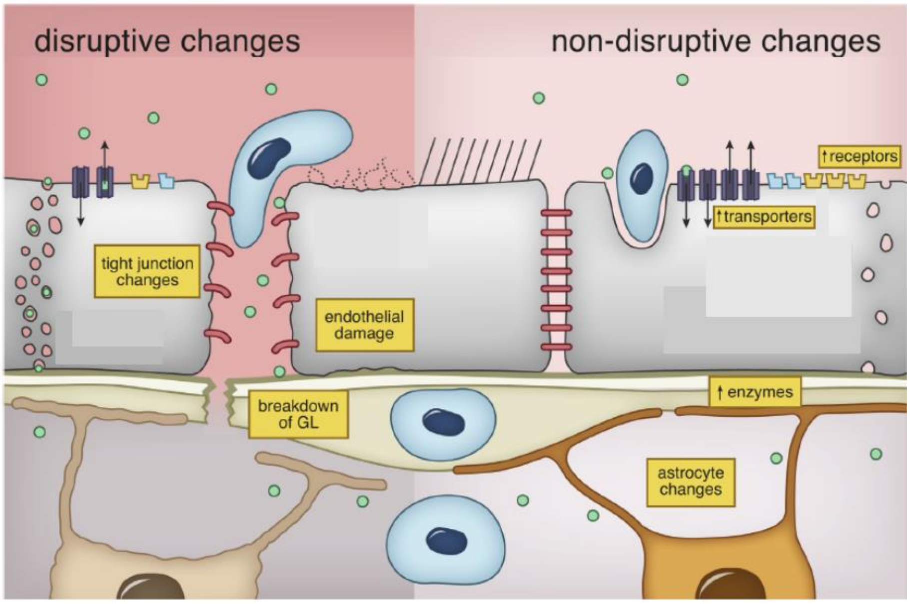

Figure 1.3: Disruptive and non-disruptive changes that occur at the blood-brain interface. Schematic of disruptive changes to the BBI (left) such as tight junction deterioration, endothelial damage and breakdown of the glial limitans (GL) and non-disruptive changes to the BBI (right) such as changes to transporters and receptors and changes to the enzymes and astrocytes. Schematic adapted from: [42].

There is increasing evidence to suggest that astroglial AQP4 plays a key role in brain clearance pathways, via BBI permeability and glymphatic function, which help to mediate the removal of deleterious proteins from the brain. The recently discovered glymphatic system is a brain-wide pathway that describes the convective exchange between the CSF and interstitial fluid (ISF) [45]. The fluid movement between compartments which is facilitated by AQP4 channels, which occurs between the perivascular space and brain parenchyma [46, 47]. Impairment of the glymphatic clearance system has been shown to aggravate progressive aberrant protein accumulation of amyloid-β (Aβ) [45, 48, 49]. More specifically, removal of the AQP4 water channel has been shown to impair glymphatic function in *Aqp4*$^{-/-}$ mice which likely contributed to the 55% increase in the accumulation of Aβ measured in these animals [45]. As such, this raises the exciting possibility that targeting glymphatic impairment via the dysfunction of AQP4, may be an early biomarker of neurodegenerative disease.

AQP4 can be found in a regular assembly located on the endfeet of astrocytes that make up the BBI, which is known as AQP4 polarisation. There are several proteins, including α-syntrophin (α-Syn) and α-dystrobrevin (α-DB), which anchor the AQP4 channel to the perivascular location at the BBI. The polarisation of AQP4 is a key element of the glymphatic pathway, and also this structure enables the optimal function of the water channels [50]. The reduction of AQP4 polarisation at the BBI has been found to correlate with the extent of cognitive decline in AD sufferers [51]. Therefore, AQP4 polarisation effect on water permeability across the BBI could be a key component in the pathogenesis of neurodegeneration.

AQP4 channels are central to BBI water permeability due to the rapid transfer of water that occurs through them [31, 52, 53]. A marked reduction of BBI water permeability has been recorded, in several studies in mice when AQP4 was absent [36, 38]. In these studies, BBI water permeability was assessed by a reduced brain water content of *Aqp4*$^{-/-}$ mice following water intoxication by the intraperitoneal injection of water [38]. Also there was no dye staining observed in the *Aqp4*$^{-/-}$ mouse brains' following an injection on Evan blue dye [36]. To date, there are limited studies that have investigated changes in BBI water permeability associated with AQP4 in the context of neurodegeneration.

It is increasingly recognised that vascular dysfunction is the first measurable pathological change that occurs in certain neurodegenerative diseases [20, 54, 55]. Additionally, there is growing evidence to suggest that loss of integrity in the BBI is an early event in AD [1, 20]. The two-hit vascular hypothesis of AD proposes that vascular risk factors cause breakdown to the BBI (hit one) and allow the influx of pathogens and neurotoxins into the brain, which will induce a local immune response. The immune response precedes amyloid-β (Aβ) deposition (an early characteristic feature that can be detected in AD), which reduces Aβ clearance by the liver and kidneys, as well as bulk flow of CSF [44], consequently, causing an increase in Aβ deposition (hit two) that ultimately lead to brain atrophy, neurodegeneration and cognitive decline [1, 3, 10, 56]. Therefore, techniques that are able to target the early changes to the BBI may give an indication of the toxic molecules, such as Aβ, that are moving into the brain parenchyma and could help to elucidate mechanistic changes that might serve as a novel early biomarker for neurodegenerative diseases.

1.2 Techniques for the Assessment of Blood-Brain Interface Permeability

1.2.1 Invasive Techniques for assessing Blood-Brain Interface Permeability

Over the last century there has been increasing research to better understand the permeability mechanisms of the BBI to maintain brain health and homeostasis [57, 58]. Goldmann is often accredited to be one of the first to demonstrate that the brain is protected from the influx of exogeneous molecules [59]. He injected a dye, trypan blue, into a rat and observed that all of the endogenous tissues including those of the spinal cord turned blue (**Figure 1.4A**), while the brain itself remained its normal colour (**Figure 1.4B)**. Since the early experiments, dyes and probes (fluorescent or otherwise) have been used extensively to understand how the BBI closely regulates the molecules that are able to pass into the brain.

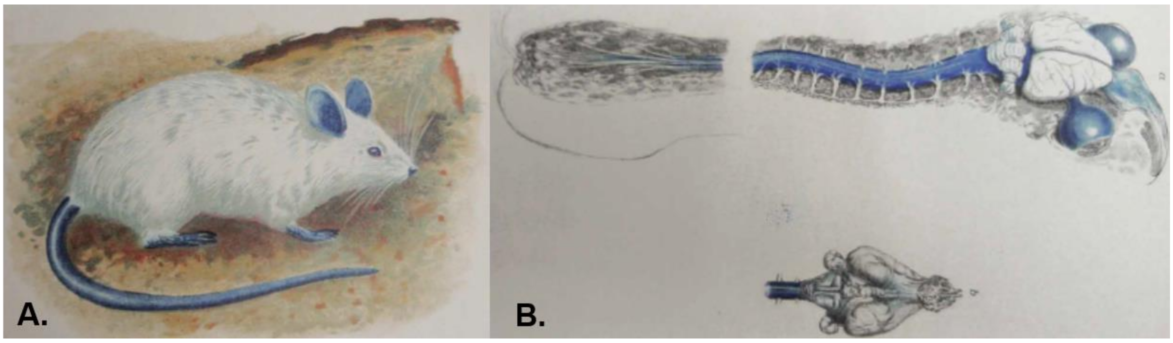

Figure 1.4: Goldmann's Trypan Blue Injection experiments. **A.** 1st experiment – adult rat following a systemic injection of trypan blue solution take from: [59]. **B.** 2nd experiment - brain and spinal cord of adult rat following lumbar subarachnoid injection take from: [60].

Fluorescence microscopy can be used, with different sized molecular probes, to assess the permeability of the BBI. Since the BBI is highly regulated, the size and the polarity of the molecules is very important for the successful passage into the brain parenchyma. *In-vivo* two-photon imaging is also able to examine the permeability of the BBI, to different sized fluorescently labelled tracers, in various pathological conditions [61, 62]. These techniques, such as immunohistology and fluorescence imaging, are often non-recovery as the techniques require slices of brain tissue to be analysed. However, understanding the properties of the BBI via the assessment of the delivery of fluorescently labelled particles to the brain has been key to better understanding drug delivery to the brain [63].

Barrier properties can also be probed *in-vitro.* Crone & Olsen discovered that an electrical resistance could be measured across microvascular endothelium which correlated with the permeability of the endothelium cells. This discovery led to the development of a technique called transendothelial electrical resistance (TEER) to assess the permeability of the BBI *in-vitro* [64]. Increasingly complex cell cultures have been developed to incorporate astrocytes and pericytes alongside the endothelial cells to fully assess the interaction of the components of the BBI [65]. Recent studies have shown that mutations associated with neurodegenerative diseases are able to independently cause BBI dysfunction and subtle changes to the barrier function over time that could lead to more substantial damage to the BBI [66].

Disruption of the BBI has been routinely reported *in-vivo* using biochemical studies of the cerebrospinal fluid (CSF)/ plasma albumin ratio used to determine BBI permeability and function [67]. CSF/ plasma albumin ratio is a comparison between of the level of albumin in the CSF and in the blood plasma as an indicator of BBI permeability. Albumin is an abundant protein which is usually found in the blood, unless there is disruption to the BBI when it can also be detected in the CSF, giving a measure of the integrity of the BBI. Previously, CSF/ plasma albumin ratio have been found to be significantly increased in patients with vascular dementia with multiple infarcts, but no changes were found with those diagnosed with early-onset AD [68]. Measuring the extent of the BBI damage using this technique may be limited by the large size of the albumin molecules (~ 67 kDa), meaning that only gross defects in the BBI are detectable. Further, a lumbar puncture is required for retrieval of CSF, which can lead to complications and side effects, especially for vulnerable older patients. This technique also does not provide any *in-vivo* spatial information about the defects to the BBI integrity.

There are several immunostaining techniques that are able to detect endogenous, blood-derived proteins, such as fibrinogen, thrombin and plasminogen, in post-mortem tissue that would be indicative of damage to the BBI. These are blood proteins that are not found in the brain parenchyma in normal conditions, but only when there has been disruption to the BBI. Fibrinogen has been found to interact with amyloid-β (Aβ) that correlates with a reduced cognitive performance in mice, and is associated with an increased risk of vascular dementia and AD [69, 70]. A limitation of these invasive techniques, is that they are performed *ex-vivo* and there can be complex tissue preparation processes that may degrade or distort data to be misrepresentative of the *in-vivo* processes.

The CSF/ plasma albumin ratio and immunostaining techniques only give information about an increase in permeability shown as a “leaky” BBI which might not be the only mechanism that is associated with pathological changes in the brain. There are conditions where the BBI may become less permeable to particular molecules which could also have deleterious consequences for the brain. It is difficult to accurately and comprehensively describe BBI dysfunction in AD *in-vivo or in-situ*, since the majority of the studies derive from animal models or from *post-mortem* analysis [71, 72]. However, moving towards minimally invasive methods such as brain imaging techniques may provide functional and spatial information about BBI permeability in human AD.

1.2.2 Imaging Techniques for Assessment of Blood-Brain Interface Permeability

Brain imaging techniques such as positron emission tomography (PET), computer tomography (CT), and magnetic resonance imaging (MRI) have been established to measure BBI permeability, crucially reporting additional spatial information about the barrier properties [67]. These techniques can be applied to humans, and also to rodent models for technique characterisation ahead of clinical translation.

BBI permeability can be measured using PET imaging, by analysing the signal from a radioactive tracer transferring between the blood and the brain. Generally, PET imaging has been used to measure permeability at the BBI or for the evaluation of therapeutic molecules passing into the brain parenchyma. This technique also has the capacity to provide highly specific information about the transporters found at the BBI such as GLUT1 or P-Glycoprotein (P-gp) which help to facilitate the movement of molecules across the BBI, and whose function seems to changes in AD [73, 74]. A novel PET tracer, [^{11}C]TGN-020, has been developed by Nakamura *et al.* that targets AQP4 and this group have demonstrated proof-of-principle that AQP4 can be imaged in the human brain [75]. This allows the spatial distribution of AQP4 to be characterised non-invasively, but it is not specific to AQP4 function to assess the mechanisms such as impairment to the glymphatic system. A drawback of PET imaging is that it requires the availability of a cyclotron to produce the customised radioisotopes that are injected intravenously into the patient.

CT imaging is a technique that uses x-rays and an electronic detector array to produce an image. To measure BBI permeability, a contrast enhanced CT scan is needed, that requires an intravenous injection of a tracer followed by the acquisition of images sequentially, to monitor the concentration of tracer in the tissue and the feeding artery over time [76]. Kinetic perfusion models are applied to the time-course of the CT data to extract physiological permeability information [77]. CT scans are routinely used in the clinic as they provide a cheaper option compared to other imaging techniques such as MRI. However, patients are exposed to radiation and also include a tracer injection which is not always viable. CT imaging has mainly been applied to acute stroke and brain tumour when substantial disruptive change to the BBI has occurred [76].

MRI provides a minimally invasive option, with an increased spatial resolution compared to PET imaging, also without the need for the injection of a radioactive tracer into the patient for the measurement of BBI permeability. Both PET and CT use ionising radiation which is potentially harmful especially with repeated exposure. Therefore, MRI has distinct advantages for conditions such as neurodegenerative disease when it is necessary to assess the disease progression longitudinally, over many years or even decades. Hence, MRI is highly suitable as a technique to measure BBI permeability.

Dynamic contrast enhanced (DCE) MRI is generally considered as the ‘gold standard’ MR technique for the assessment of BBI permeability. This technique requires a MR contrast agent, often a gadolinium-based contrast agent (GBCA), which is administered intravenously. The GBCA shortens the longitudinal relaxation rate (T1) of the tissue by penetrating into the brain parenchyma where the BBI is leaky or damaged, which will appear as enhanced signal in a T1-weighted MR image.

Currently there are conflicting ideas about whether it is possible to estimate the permeability of the BBI in healthy tissue using this method since it is not possible for the GBCA to transfer across an intact BBI [78].

The MR signal intensity in DCE measurements is acquired over a time-course and kinetic models are applied to the detected signal to quantify the contrast agent transferring into the tissue and to obtain an estimate of BBI permeability. The first theoretical framework that was established using DCE techniques was the Tofts model which uses a single parameter, K^{trans}, a volume transfer constant to describe an index of permeability. K^{trans} encompasses the permeability surface product (PS) and tissue density, therefore it reflects a combination of permeability and perfusion (or flow) [79]. Either an increase in permeability or an increase in flow will increase the K^{trans} parameter. In a regime where there is a high flow, the limiting factor would be the permeability, therefore the K^{trans} would more closely reflect the permeability. Conversely in a regime of low flow, the limiting factor would be the flow therefore in this situation the K^{trans} parameter would be more reflective of the flow.

The theoretical models have been developed to the extended Tofts model which incorporates the volume/ concentration of the intravascular compartment. A further permeability model that has been established is the Patlak model [80], which assumes that there is no backflow, and may be most suitable for measuring low levels of BBI permeability [81]. More recently, the kinetic models have been extended to a two-compartment exchange model be able to separate capillary permeability (PS) and the cerebral blood flow (CBF) from K^{trans}, as well as estimating the capillary volume and the extravascular tissue volume. Overall the extended models are intended to reduce the assumptions of BBI permeability estimations using DCE-MRI method [82]. But ultimately, the choice of the theoretical model will depend on the quality of the DCE data and the desired parameters necessary for the evaluation of the pathology [83].

In recent years, DCE-MRI techniques are becoming increasingly sophisticated and technical development in the MRI sequences have enabled the technique to be used, not only in local regions with significant damage to the BBI, but in neurodegenerative conditions where small but diffuse global changes in permeability have occurred. Zlokovic *et al*. were able to detect an increase in BBI permeability in the hippocampus of mild cognitive impairment (MCI) patients relative to age-matched healthy controls using an advanced DCE-MRI platform [2]. While there remains a debate about the robustness of estimates for K^{trans} in healthy tissue, this emerging evidence suggests that the BBI within certain brain regions such as the hippocampus and the caudate nucleus becomes more leaky with normal physiological ageing and suggests that certain brain regions may have different barrier properties or different vulnerability to age-related changes in the brain [2]. Another DCE-MRI study found that the extent of diffuse BBI leakage, particularly in the grey matter regions of the brain, was correlated with the degree of cognitive impairment [3].

1.2.3 Imaging water permeability at the blood-brain interface

DCE-MRI techniques have evolved to be able to probe the dynamics of the water molecules, transferring across the intact BBI, while interacting with the GBCA that remains in the vascular compartment. There are several techniques that can be implemented to use contrast agents within a steady state to model the magnetisation of the water molecules transferring from the vascular compartment into the extravascular compartment. These techniques are thought to have increased sensitivity to early changes at the BBI before substantial disruption has occurred.

The first technique to estimate water permeability across the BBI was developed by Schwarzbauer *et al.*, using a stepped GBCA infusion technique in rats to acquire T1 measurements that were sensitive to BBI water exchange [84]. This technique was successfully implemented in the cortex, hippocampus and the jaw muscle of the rodent, though the imaging protocol was lengthy (2 hours). The T1-dependent method was then extended to a first pass technique to measure the water permeability, and was later optimised and applied to the human brain to assess BBI water permeability [85]. The same group also applied the technique to patients with glioblastoma multiforme, using superparamagnetic iron oxide nanoparticles (SPIONs) as a contrast agent, which showed a reduction in the water permeability [85]. Anderson *et al.* proposed that these techniques may be sensitive to BBI abnormalities that occur in early AD [86].

The water exchange index (WEI) is a further method that can give a surrogate estimate of the water permeability across the BBI that was developed by Kim *et al.* [87]. WEI is based on the principle that the cerebral blood volume (CBV) estimates vary with different excitation pulse flip angles and measurements are taken before and after the injection of a contrast agent [88]. This technique has detected changes in the WEI in mice following a middle cerebral artery occlusion (MCAo). Also, an increase in the water permeability was measured in a transient stroke model using the WEI method [89]. These techniques have yet to be applied to models of neurodegeneration.

A recent study implemented a multi-flip angle multi-echo (MFAME) MRI technique to measure the vascular water exchange across the BBI. This study reported an increase in vascular water exchange, as measured using the MFAME-MRI technique, in a rat model of AD which also correlated with a breakdown of occludin, a TJ protein [90]. This technique was performed alongside the conventional DCE-MRI method to model the K^{trans} variable where no measurable differences were reported in the AD rat brain. This would imply that water exchange measurements are able to detect more subtle BBI dysfunction which may occur before a gross physical breakdown is present, that would allow GBCA into the brain parenchyma to enable a measurement of K^{trans}. This highlights the prospect of water exchange measurements to give an index of BBI permeability to water of being a sensitive, early biomarker for diseases such as AD.

While the use MR contrast agents are routine in the clinical setting, there is increasing speculation to the potential harm that repeated doses may have in the long term [91]. Therefore, techniques for assessing BBI permeability without the need for intravascular MR contrast agents are highly beneficial.

1.2.4 Non-contrast techniques for imaging blood-brain interface water permeability

Arterial spin labelling (ASL) imaging techniques have been developed to target water permeability across the BBI, as a novel, endogenous pathway that may be able to elucidate physiological changes in BBI structure/function that cannot be detected using the larger contrast agents for DCE-MRI techniques [87]. Water is highly desirable as a contrast agent because of its small size (~18Da), and especially when it can be targeted endogenously in the body. ASL was originally developed as a non-invasive alternative for imaging cerebral perfusion [92, 93]. The early ASL studies assume that the MR signal measured derives from a single, well-mixed compartment, and therefore water permeability measurements could not be extracted. However, new theoretical frameworks have been established, and technical developments in the MRI hardware allows for a higher precision and SNR with the data acquisition. This means that ASL techniques can be extended when combined with other contrast mechanisms to separate intravascular (IV) and extravascular (EV) compartments, and surrogate index of BBI permeability to water can be measured by estimating the rate of water exchange across the two compartments. Two compartment kinetic models are used to extract dynamic parameters such as tissue transit time (δ) or water exchange rate (K_w) that quantify BBI water permeability between the IV/ EV compartments.

There are several general kinetic models that can be used to separate the derived signal into two IV/ EV compartments, to extract a parameter that represents an index of BBI permeability to water [94-98]. These models consider the arterial input for the labelled blood water, with water exchange occurring at the capillary bed, and venous exit contribution for the labelled blood water that did not transfer into the extravascular tissue. Often, the water exchange rate (K_w) (described by PS_W / V_c, where PS_w is the permeability surface product of water and V_c is the capillary volume) is used as an index of BBI water permeability. A slight modification of this model can be thought of as a one-compartment Kety model [99] where the vascular compartment directly supplies the extravascular compartment, assuming 100% water extraction. There are distinct assumptions for each of the models but the analysis is dependent of the type of ASL technique being used and labelling scheme that is implemented.

The first demonstration of BBI water permeability measurements achieved using an ASL technique was in the rat brain, using diffusion sensitive gradients at a range of b-values, known as diffusion-weighted (DW) ASL [100]. DW-ASL is based on the differences in diffusion properties which is measured via the apparent diffusion coefficient (ADC) parameter when the water molecules are in the vasculature or in the extravascular/ extracellular space. The pseudo diffusion coefficient of the IV compartment is much higher than the extravascular tissue ADC, therefore the IV signal can be eliminated with relatively low diffusion encoding to allow the separation of the IV and EV signals. The IV and EV signals compartments can then be modelled to measure the transfer of water across the BBI.

The first application of the DW-ASL in the human brain was implemented by Wang *et al.* with water permeability measures ($K_w = 193 \pm 50\ \text{min}^{-1}$) in grey matter across four subjects [96]. This work also demonstrated that there is a substantial increase in water permeability in a brain tumour, particularly in the aggressively growing region with high flow [96]. Recently, a 3D gradient and spin echo (GRASE) sequence with a diffusion preparation has demonstrated the test-retest reproducibility of this DW-ASL technique for water permeability measures in the human brain [101]. In this study, the water exchange rate was measured to be higher in the grey matter (109.6 ± 18.9 min^{-1}) compared to the white matter (94.1 ± 19.6 min^{-1}). This work also highlighted that people at risk of small vessel disease, and diabetes showed an increase in the water permeability exchange rate.

The advantage of the DW-ASL technique for the modelling of BBI water permeability is that there is an ~100-fold difference between the fast-decaying pseudo-diffusion coefficient of the intravascular compartment and slower extravascular diffusion, therefore it is relatively straight-forward to separate the two compartments. The advanced sequences seem to show consistent reproducibility which is promising for clinical applications [101]. However, there is evidence to suggest that the DW-ASL technique might underestimate the intravascular compartment of the signal, since the capillary component may not contribute the measurable values derived from this compartment [102, 103]. The measured intravascular fraction across subjects shows close correlation with the CBF, which could be a complicating factor to the BBI permeability to water measures [100, 102, 104].

A further non-contrast method measure of BBI permeability to water, Water Extraction with Phase Contrast Arterial Spin Tagging (WEPCAST), aims to quantify the water extraction fraction by measuring the ASL signal in the main draining vein, the superior sagittal sinus (SSS). The ASL remaining signal, that has not been extracted into the brain tissue but has moved to the SSS, is detected and can be modelled according to the Renkin-Crone model to extract the kinetics of the labelled vascular water that has transferred into the tissue via the PS_w parameter [105]. This technique has proved sensitive to detect significant changes to patients with mild cognitive impairment (MCI) who show an increase in BBI permeability to water [106]. Currently, this technique can only yield a global measurement for water permeability and therefore would not be able to distinguish any regional permeability effects that may be relevant for disease conditions.

An alternative method able to measure BBI permeability to water is to use T2-prepared ASL to separate the difference in transverse relaxation (T2) that derives from IV and EV compartments. Firstly, using T2 relaxation under spin tagging (TRUST) pulsed ASL sequence and a T2-prepared flow-alternating inversion recovery (FAIR) ASL sequence with a 3D GRASE readout have been applied to the human brain for an index of BBI permeability to water [96, 107, 108]. A multiple echo time approached based of a FAIR sequence was also applied to the rat brain, which also provided additional information about the oxygenation of the arterial side of the vasculature by explicitly measuring the fast-decaying T2 component of the ASL signal [109].

In the T2-ASL technique there is likely to be minimal directional dependence of the magnetic gradients on the signal attenuation, as may be present in DW-ASL [110]. Two compartment kinetic perfusion models can be applied to estimate the tissue transit time (δ), the time for the labelled spins to reach the extravascular tissue compartment and the arterial transit time, when the labelled vascular water reaches the imaging slice. However, there is need to further examine the ability of these techniques to help better understand the physiological relevance of BBI water permeability as an imaging biomarker.

1.3 Biomarkers of Blood-Brain Interface water permeability in neurodegenerative disease

An important motivation for developing non-invasive, non-contrast techniques is for the early detection of neurodegenerative diseases, such as AD. It is thought that the changes that occur in AD begin some 20 years before the patient manifests with the first clinical symptoms [111]. Currently, the clinical differentiation of AD from other forms of dementia are the appearance of deposition of amyloid-β (Aβ) and intracellular neurofibrillary tangles (NFT) of tau protein. However, we have an incomplete understanding of the factors that underlie AD pathogenesis, which hinders the development of a cure for this condition. Emerging imaging techniques are beginning to show increasingly promising results in MCI patients and AD animal models when targeting changes in BBI permeability to water.

The biggest risk factor for AD is ageing, and there are many pathologies that are a common feature of physiological ageing including an increase in BBI permeability [67]. At present, the differences that distinguish normal ‘physiological’ ageing from the biological changes that cause the brain to be vulnerable, specifically to neurodegenerative disease, are very poorly understood. Hence, there is a need for sensitive techniques that are firstly able to detect subtle changes that occur in the ageing brain that might increase the vulnerability of the brain to dementia. Therefore, the development of non-contrast MRI techniques to target changes in the water permeability at the BBI that can be applied to the ageing brain might provide insight into early, non-disruptive mechanisms that precede the larger disruption to the BBI integrity that has already been detected in AD patients. It would also be highly beneficial to have a non-contrast technique when looking at a vulnerable ageing population to minimise additional nephrological complications associated with the injection of a contrast agent.

Despite there being many advancements in MRI techniques to probe BBI water permeability, there has been little work in understanding the physiological mechanisms that govern the water permeability measurements. It is crucial that techniques are characterised biologically for the clinicians to better understand the precise biological mechanisms that are being detected with new imaging tools. There are a vast number of genetic and transgenic mouse models of neurodegenerative diseases that have been developed to help to elucidate the biological processes that may determine the onset of neurodegeneration. Therefore, the development of multiple echo time (multi-TE) ASL in the mouse brain, would provide the opportunity to assess the sensitivity of the technique to specific biological mechanisms that may be associated with the early pathogenesis of AD. Imaging experiments using mice can be performed in highly controlled conditions. Therefore, combining *in-vivo* MR imaging data with more invasive genetic expression profiling of the animals will build our understanding, both technically and biologically, about the basis of multi-TE ASL measurements.

An elegant starting point for better understanding the physiological underpinnings of multi-TE ASL in targeting BBI water permeability, is to examine its sensitivity to changes in AQP4 water channels as a mechanism for vascular water exchange. There is evidence to suggest that there is dysfunction to AQP4 with ageing, which seems to be related to the depolarisation of AQP4, when the water channels are no longer located on the astrocytic endfeet at the BBI. The extent of depolarisation of AQP4 has been found to be correlated with the severity of AD [51]. The deposition of Aβ has also been shown to alter the expression of AQP4 and disrupt the localisation of AQP4 to the astrocytic endfeet in an AD mouse model [112]. Further studies show ~55% reduction in Aβ clearance in AQP4-deficient mice which is thought to be due to an inhibited glymphatic function [45]. In addition, the deletion of AQP4 in an APP/PS1 mouse showed clear signs of advancing AD pathology [113]. However, the mechanisms in which BBI permeability to water is implicated in disease has been scarcely explored.

Multi-TE ASL should be able to probe BBI permeability to water when the BBI still remains intact (i.e. before gross structural changes that allow the egress of larger contrast agents such as GBCAs). Since the flux of water across the BBI can both increase and decrease, BBI water permeability measurements may be able to capture novel physiological changes that have not previously been detected (for example a reduced BBI permeability due to a reduction in AQP4 polarisation). Given that there are many physiological changes that occur in ageing, developing a robust and versatile technique in the mouse brain would be a useful tool for better understanding of the precise changes in physiological ageing as a model for the early stages of neurodegenerative pathology. Moreover, performing functional imaging on the mouse brain is technically challenging due to the markedly smaller size of the mouse brain compared to the rat brain or other larger species. However, a notable benefit is that high field 9.4T MRI will have a significant increase in the signal-to-noise (SNR). Thus, the pre-clinical implementation of a multi-TE ASL for the mouse brain could help to elucidate some of the biological processes at the BBI that can be detected with non-contrast imaging.

Thesis Aims

This thesis aims to address the following research questions: i.) what are the biological mechanisms that affect water permeability across the blood-brain interface and ii.) can these alterations in water permeability be detected by a multiple echo time arterial spin labelling technique?

This thesis will be presented in five chapters, each with a specific aim as indicated:

1. To develop a multi-TE ASL technique protocol that can be applied to the mouse brain for assessment of the exchange time (a quantitative index of BBI permeability to water).

2. To assess whether the multi-TE ASL technique is able to target the expression of AQP4 water channels at the BBI.

3. To implement the multi-TE ASL technique on a second MR system to evaluate the consistency of the BBI water permeability measurements on a new, more advanced, imaging system.

4. To apply the multi-TE ASL technique to a mouse model with reduced AQP4 at the location surrounding the BBI for assessment of AQP4 polarisation on the BBI water permeability.

5. To assess whether there are changes to BBI permeability to water with ageing and whether there are associated changes that occur to the molecular components of the BBI.

Chapter 2

Development of Multiple Echo Time Arterial Spin Labelling Technique in the Mouse Brain

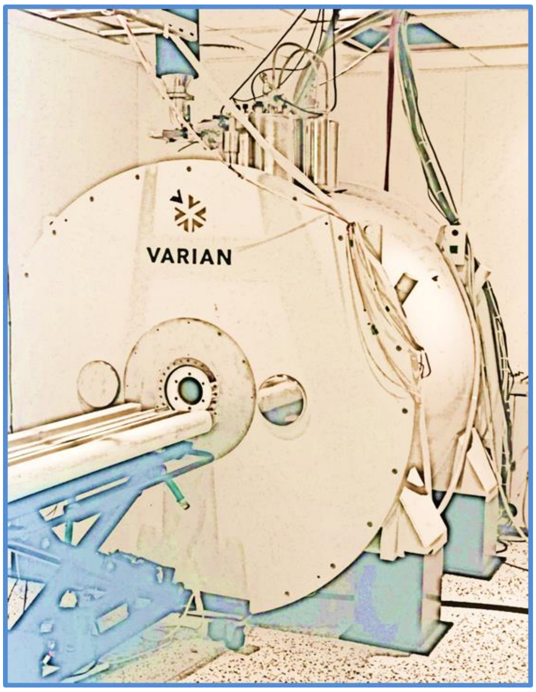

9.4T Agilent Scanner,
Centre for Advanced Biomedical Imaging

Aim

The aim of the work in this chapter was to develop a robust imaging protocol to assess blood-brain interface (BBI) permeability to water in the mouse brain. The development of a non-invasive technique to assess BBI permeability in the mouse brain would enable application to mouse models of BBI abnormalities and neurodegenerative disease in highly controlled experimental conditions with direct translational relevance to clinical measures.

This chapter describes the theory and methodological implementation for the application of multiple echo time arterial spin labelling (multi-TE ASL) technique to the mouse brain. The technique was optimised to be able to separate the intravascular (IV) and extravascular (EV) contribution of the ASL signal in cortical brain tissue. The IV-EV separation of the ASL signal allows the ASL data to be modelled using the two-compartment kinetic perfusion model to estimate the temporal profile of water exchange between compartments. This exchange time (T_{ex}^{w}) measurement represents a quantitative estimate of BBI permeability to water.

This work was presented as an oral presentation at ISMRM 17, Hawaii, USA which led to a collaboration with Dr Catherine Morgan at The University of Auckland, New Zealand.

2.1 Introduction

Arterial spin labelling (ASL) is a functional MRI technique to assess perfusion that was originally developed in the 1990s [92, 114, 115]. The principle of ASL is to label a bolus of intravascular blood water and it captures its perfusion into the tissue. Accordingly, the technique is non-contrast, eliminating the need for an exogenous (often gadolinium-based) contrast agents and non-invasive, using the endogenous labelled blood water as the contrast agent. Therefore, it has clinical value, especially for more vulnerable patients, for measures of cerebral haemodynamics and therefore is highly desirable to be extended for use to estimate BBI permeability.

ASL is based on the production of two images: a labelled image and a control image, that are captured after a specified time delay to allow the labelled blood water to reach the imaging region. The ASL image is generated by the subtraction of these two images and will give a measure proportional to the cerebral blood flow (CBF). ASL techniques have inherently low SNR (often ~1% of full MR signal) due to the signal difference from the magnetic inversion. There are currently three main ASL techniques: pulsed ASL (PASL), continuous ASL (CASL) and pseudo-continuous ASL (pCASL). PASL uses a radiofrequency (RF) pulse to invert the magnetisation in a slice-selective (labelled) and a non-selective (control) imaging volume. CASL labels the blood water as it flows through the labelling plane, which is often positioned across multiple feeding arteries upstream from the imaging region. Finally, pCASL, uses short pulse blips to continuously label a bolus of the blood water in a similar fashion to CASL.

Advanced ASL sequences have been developed, combining with other contrast mechanisms, to separate the intravascular (IV) and extravascular (EV) ASL components to measure an index of blood-brain interface (BBI) permeability to water. Separation of the two compartments can be achieved by applying DW-gradients to distinguish the IV-EV compartments according to the diffusion properties, as described in previous studies [96, 97, 100, 101]. Alternatively, multiple echo time (multi-TE) ASL separates the compartments according to the different transverse relaxation (T2) properties of signal derived from the IV-EV spaces. In previous studies, multi-TE ASL has been applied to the human brain [107] and in the rat brain [109].

Multi-TE ASL techniques are based on T2 properties that are derived from the labelled blood water from the intravascular compartment and the extravascular tissue, $T2_{IV}$ and $T2_{EV}$ respectively. Wells *et al.* demonstrated that $T2_{IV}$ is dependent on the oxygenation which could provide additional information about the oxygen saturation on the arterial side of the vasculature [109]. This oxygenation information is highly dependent on the magnetic field strength of the MR system. In the clinical setting using a 1.5T or 3T scanner the $T2_{IV}$ is higher than the $T2_{EV}$, however at high field 9.4T the $T2_{IV}$ decreases to be lower than $T2_{EV}$ and decrease further with a reduction in oxygenation [109, 116]. Therefore, preclinical implementation of the multi-TE ASL method could help to elucidate about how systemic or local oxygenation effects the T2.

To my knowledge, the advanced ASL techniques have yet to be applied to the mouse brain. This may be due to the markedly smaller size of the mouse brain compared to the rat or human brain, and further, ASL techniques have inherently low SNR which makes it technically challenging for ASL signal acquisition and evaluation. However, the implementation of multi-TE ASL in the mouse brain to assess vascular water permeability at the BBI would be highly beneficial because it could then be applied to the vast range of mouse models that are available to assess neurological diseases.

The following sections will describe the theory behind the novel measurements that will be used to assess BBI permeability to water. Along with the theoretical calculation of CBF as a conventional measure of perfusion. Followed by the final methodological implementation of multi-TE ASL in the mouse brain for measurements of BBI water permeability.

2.2 Theory

ASL methods allow the MRI signal from labelled blood water that has traversed in the imaging region and perfused into the tissue, to be isolated. In order to estimate BBI permeability to water, it is then necessary to separate the proportion of labelled blood water in intravascular (IV) and extravascular (EV) compartments. This section describes how BBI water permeability estimation can be achieved by using a multi-TE ASL acquisition approach.

In this work, PASL is implemented using a flow-sensitive alternating inversion recovery (FAIR) sequence with a labelling strategy previously shown by our lab to give reproducible labelling efficiency [117]. The FAIR labelling scheme is shown schematically for the mouse brain in **Figure 2.1.** The FAIR technique alternates between a global inversion (control image) across a large region of the subject, and a slice-selective inversion (labelled image) where only the spins within the imaging slice are inverted. A subtraction of the control image and labelled image will result in an ASL image that reflects the signal from the labelled vascular water that has traversed into the imaging slice in the given inflow time.

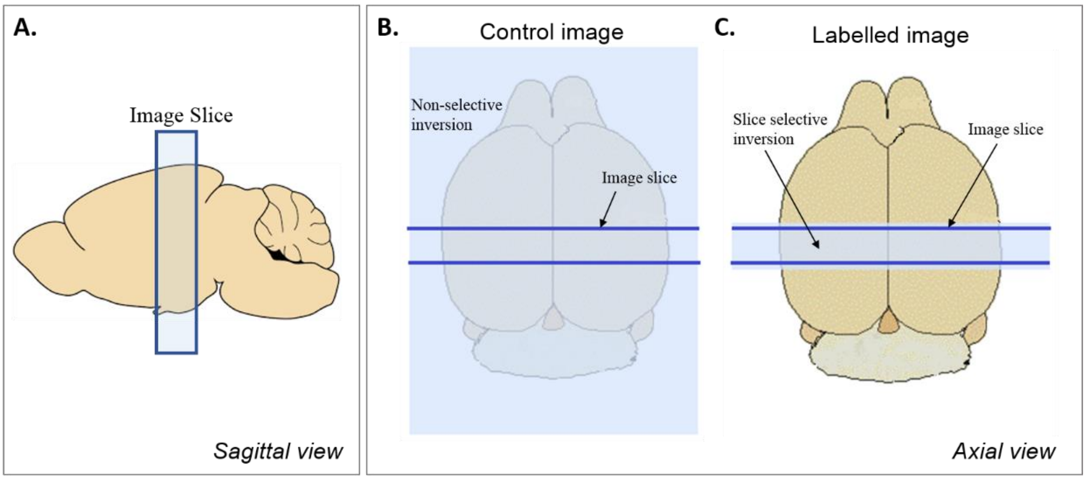

Figure 2.1: Schematic of FAIR Labelling Scheme. **A.** Position of the imaging slice in the mouse brain in this work. **B.** Control image generated from a non-selective global inversion pulse **C.** Labelled image generated from a slice selective inversion in the region of the image slice.

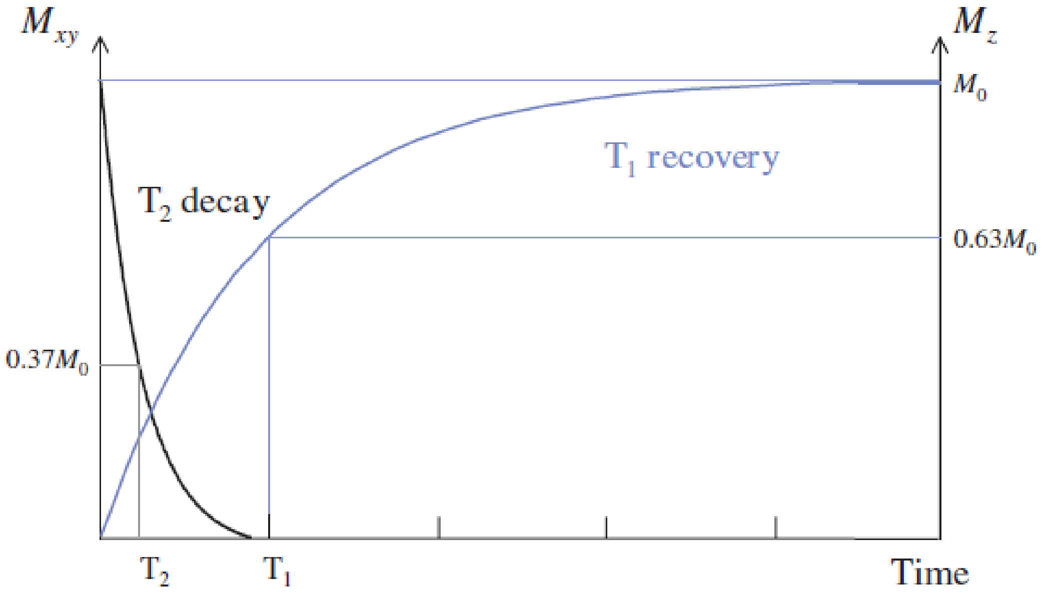

Figure 2.2: Relaxation rates. T_1 recovery, is the longitudinal relaxation and T_2 decay is the transverse relaxation that occurs simultaneously but, *in-vivo*, T_2 is much faster than T_1.

Multi-TE ASL enables several parameters to be estimated from the imaging data. The FAIR sequence labels the spins, in a selected volume, with a single RF pulse and the MR signal decays via longitudinal relaxation (T1), following the standard inversion recovery model, (T1 recovery in **Figure 2.2**) [118]. The image acquisition occurs after a selected inflow time (TI), the time between the labelling pulse and the image readout. Selecting the appropriate TI is important when considering the time scales of the physiological processes that are occurring, and will impact the measured apparent transverse relaxation rate ($T2_{app}$). A schematic of the approximate timescales for the arterial transit time, tissue transit time and temporal length of the tagged bolus for the mouse brain, are displayed in **Figure 2.3**, along with variable inflow time that is selected by the experimenter.

The arterial transit time is the time for the leading edge of label bolus to reach the imaging slice. The tissue transit time is the time between the magnetic labelling and the labelled blood water to reach the extravascular tissue, having transferred across the BBI. These two times will be estimated from the imaging data to determine the time of exchange of vascular water into the extravascular tissue, a measure I hypothesize will be sensitive to the BBI permeability to water. The temporal length of the tagged bolus (τ) determines the period of time over which labelled blood water flows into the imaging volume [119].

In this study, the measured variables are the arterial transit time, tissue transit time, and cerebral blood flow (CBF), derived by fitting both ASL signal and control signal acquired a multiple TE times to mono- and bi-exponential transverse relaxation (T2) equations (see below). The temporal length of the labelled bolus (τ) in the healthy mouse brain has been previously estimated at $\tau = 2s$ [120] in the MR system in our laboratory, using the FAIR sequence, so this value will be assumed in this work. All the other parameters are estimated empirically into order to evaluate the exchange time of the vascular water moving into the extravascular tissue.

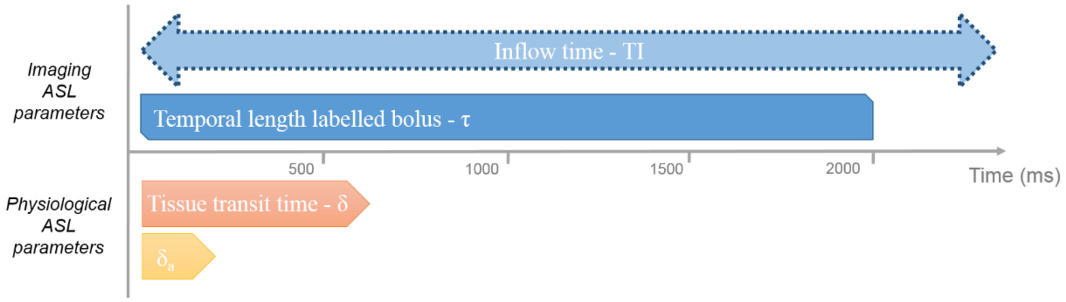

Figure 2.3: Schematic for the approximate timescales for the ASL imaging and physiological parameters, where δ_a is arterial transit time, δ is tissue transit time, τ is temporal width of the tagged bolus and TI is inflow time (selected for each imaging protocol).

2.2.1 Arterial Transit Time and Cerebral Blood Flow estimation

The arterial transit time (δ_a) reflects the arrival time of the labelled bolus of blood water to the imaging region of interest and in this work δ_a is estimated using a separate multiple short inflow time (multi-TI) ASL acquisition. At short inflow times the ASL signal, ΔM, fits to a linear model against TI, according to the pulsed arterial spin labelling (PASL) biophysical model [121]:

$$\Delta M = 0 \qquad \text{when } \delta a > \text{TI} \tag{1}$$

$$\Delta M(TI) = A.(TI - \delta a).exp\left(-\frac{TI}{T1_a}\right) \qquad \text{when } \delta a < \text{TI} \tag{2}$$

where A is a constant factor, dependant on CBF (A = 2α. M_{OA}. CBF/ λ), $T1_a$ is the longitudinal relaxation of the arterial blood and M_{0A} is the equilibrium magnetisation of the blood. A direct fit of $\Delta M(TI).\exp(TI/T1_a)$ as a function of TI therefore enables simultaneous estimation of both δ_a and CBF.

2.2.2 Single Compartment Model: Apparent Transverse Relaxation, $T2_{app}$

The transverse relaxation, T2 is the spin-spin relaxation time and describes how quickly the transverse magnetisation decays in a particular tissue. T2 decay occurs simultaneously with T1 longitudinal recovery, **Figure 2.2**, but typically on a much faster time scale.

T2 is evaluated by fitting the signal, M_{xy}, across several echo times to an exponential decay:

$$M_{xy} = M_0 \exp\left(-\frac{TE}{T2}\right) \tag{3}$$

where M_0 is the magnetisation equilibrium signal, TE is the echo time and T2 is the transverse relaxation.

In this study, the model is adapted for ASL signal, ΔM that is derived from the spins isolated to the labelled blood water therefore;

$$\Delta M = M_0 \exp\left(-\frac{TE}{T2_{app}}\right) \tag{4}$$

where $T2_{app}$ is apparent transverse relaxation that depends on contribution of the signal from the intravascular and extravascular space (where, as described above, IV and EV water compartments have been shown to have different T2 relaxation times). Therefore, $T2_{app}$ reflects the relative contributions of the IV space and EV tissue within the overall ASL signal.

Apparent transverse relaxation, $T2_{app}$ is highly dependent on the selected inflow time, TI. Selecting a short TI ($\delta_a < TI < \delta$), referring to the timescale schematic in **Figure 2.2,** will mean that the majority of the labelled blood water will reside in the intravascular space. This is because the labelled water has reached the imaging slice via the vasculature, but since the time length is shorter than the tissue transit time, δ it will not have transferred into the extravascular compartment. Therefore, the ASL signal will derive solely from the intravascular space and using a single compartment model, $T2_{app}$ will reflect the T2 of the arterial blood. An intermediate TI ($\delta < TI < \tau$) would describe a timescale that is greater than the tissue transit time but shorter than the temporal width of the tagged bolus. This is sufficient time for a proportion of the labelled water to move into the extravascular tissue. In this case, the ASL signal will derive from both IV and EV compartments. A long TI (TI > τ), is an inflow time that is greater than the temporal length of the tagged bolus and greater than that of the tissue transit time. In this condition, the majority of the labelled blood water will have moved into the extravascular space, since the temporal length of the labelled bolus has been exceeded and T2app would be highly similar to the T2 of the extravascular tissue.

$T2_{app}$ is a combination of both the intravascular T2 ($T2_{IV}$) and extravascular T2 ($T2_{EV}$). The $T2_{IV}$ can be influenced by the systemic oxygenation of the blood (Wells, 2013). It is important to understand the effect of the systemic oxygenation on the transverse relaxation. Also, it is crucial to be able to separate the intravascular and extravascular compartments at the intermediate inflow time. Therefore, the effects of oxygenation will be investigated via the measurement of $T2_{app}$ to understand the influence that different air mixture conditions have on systemic oxygenation, and hence will have on the transverse relaxation to provide evidence that the transverse decay of the ASL signal is indeed highly sensitive to blood oxygenation.

2.2.3 Two Compartment Model

2.2.3.1 Exchange Time, T_{ex}^{w}

The multi-TE ASL method is extended to separate IV-EV compartments to model BBI permeability to water via the exchange time parameter. This is achieved by fitting the ASL signal decay to a two-compartment bi-exponential model at intermediate inflow times (δ < TI < τ).

$$\Delta M = \Delta M_{IV} \exp\left(-\frac{TE}{T2_{IV}}\right) + \Delta M_{EV} \exp\left(-\frac{TE}{T2_{EV}}\right) \tag{5}$$

where ΔM_{IV} and ΔM_{EV} are intravascular and extravascular ASL signal weighting factors respectively, TE is the echo time, $T2_{IV}$ is the T2 value of the IV arterial compartment and $T2_{EV}$ is the T2 value of the EV tissue.

The ASL signal weighting factors enable estimation of the intravascular fraction at a given inflow time:

$$Intravascular\ fraction = \frac{\Delta M_{IV}}{\Delta M_{IV} + \Delta M_{EV}}$$

(6)

The kinetic perfusion model proposed by Alsop and Detre [93] and adapted by Wang [122] is applied to ASL signal weighting factors to estimate the tissue transit time, δ. The adapted two compartment kinetic perfusion model [93, 109, 121] is described by the following equations:

$$\Delta M_{IV} = \frac{2M_0 f}{\lambda}\{exp(-TI \times R1_a)\ [min((\delta_a - TI + \tau,\ 0)\ - \delta_a) - (\min(\delta - TI + \tau,\ 0)) - \delta]\}$$

(7)

$$\Delta M_{EV} = \frac{2M_0 f}{\lambda}\left\{exp\left(-TI \times R1_{app}\right)\left[\frac{\exp(\min(TI,\ \delta + \tau)\Delta R)\ - \exp(\delta \Delta R)}{\Delta R}\right]\right\}$$

(8)

where M_0 is the equilibrium of the magnetization, f is the CBF, λ is the blood-brain partition coefficient (λ = 0.9 [123]), TI is the inflow time, $R1_a$ is the longitudinal relaxation rate derived from the arterial compartment, assumed here to be 1/2.4s [124], $R1_{app}$ is the longitudinal relaxation rate of the tissue, here fixed at $R1_{app}$ = 1/1.7s [109], $\Delta R = R1_{app} - R1_a$, and τ is the temporal length of the tagged bolus τ = 2.0s inferred from previous experiments in our laboratory [120].

The exchange time (T_{ex}^{w}) indicates the time for magnetically labelled vascular water to exchange across the BBI into brain tissue once the labelled bolus reaches the imaging slice:

$$T_{ex}^{w} = \delta - \delta_a \qquad (9)$$

The exchange time parameter provides a quantitative, surrogate marker to BBI permeability to water.

2.3 Method

Several imaging protocols were developed for application to the mouse brain to measure $T2_{app}$, CBF, arterial transit time and tissue transit for assessment of BBI permeability to water.

2.3.1 Experimental Set-Up

2.3.1.1 Animal Set-Up

All experiments were performed in mice in accordance with the European Commission Directive 86/609/EEC (European Convention for the Protection of Vertebrate Animals used for Experimental and Other Scientific Purposes) and the United Kingdom Home Office (Scientific Procedures) Act (1986). All mice were acclimatised two weeks prior to data acquisition in an animal house maintained at a temperature of 21 ± 2 °C and a relative humidity of 55 ± 10%, on 12h light/12h dark cycle with food and water provided *ad libitum*. 16 female C57/BL6 WT mice (Charles River Laboratories) at 18 ± 3 weeks were used to establish the techniques for effect of oxygenation on $T2_{app}$ (n = 10) and non-invasive assessment of BBI permeability to water in the mouse brain (n = 5 for TI = 400 ms and n = 6 for all other experiments).

All animals were induced in 2% isoflurane anaesthetic in a mixture of 1.0 L/min medical air, and the isoflurane level was manually adjusted throughout the scans to maintain the respiration rate at ~100bpm. Animals were secured into the MRI cradle with a nose cone, ear bars and bite bar to minimise head movement during the scan. Core body temperature was monitored using a rectal probe (SA Instruments) and maintained at 37 ± 0.5°C via regulation of an adjustable temperature water bath.

2.3.1.2 Image Acquisition

Images were acquired using a 9.4T VNMRS horizontal bore MRI scanner (Agilent Inc.) with an Agilent 205/120HD gradient set. A 72 mm inner diameter volume coil and a two-channel array surface coil (Rapid Biomedical) were used for RF transmission and reception respectively. Prior to data acquisition, 1st and 2nd order shimming was performed to reduce the magnetic field inhomogeneities across the brain.

An anatomical reference scan was acquired using a T2-weighted multi-slice Fast Spin Echo sequence with parameters: 30 slices, slice thickness = 0.6 mm, field-of-view = 35 x 35 mm, matrix size = 256 x 256, effective echo time (TE) = 48 ms, repetition time (TR) = 4 s, echo train length = 8.

The main ASL imaging protocol was based on a flow-alternating inversion recovery (FAIR) sequence, with global inversion width = 216mm, slice-selective width = 16mm with a two-shot segmented spin-echo echo planar imaging (SE-EPI) readout. Further sequence parameter details are provided below.

2.3.1.3 Imaging Protocol for Effect of Oxygenation on $T2_{app}$

A pilot study was carried out to measure the effects of the systemic oxygen level on $T2_{app}$ and to inform the appropriate air mixture to be used for the BBI permeability to water measurements. Blood oxygen saturation measurements from a pulse oximeter (Starr, MouseOx Plus) in an individual animal were collected over a 10-minute period in two air mixture conditions: 1.0 ml/min medical air (21% oxygen) and 1.0 ml/min oxygen (100% oxygen), with a 5-minute acclimatisation period between measurements.

The $T2^{app}$ measurements required imaging parameters: TE = 15 ms, 18 ms, 23 ms, 30 ms, 40 ms, 50 ms, 65 ms; TI = 1500ms, repetition time (TR) = 5000 ms, field-of-view (FOV) = 25 x 25 mm; matrix size = 32 x 32; slice thickness = 2mm; partial fourier, k_0 = 4, repetitions = 20, two-shot segmented EPI readout with saturation bands surrounding the region of the brain. The mice were induced and maintained on isoflurane (2%) anaesthetic in air mixture of 1.0ml/min oxygen (n = 5) or 1.0 ml/min medical air (21% oxygen) (n = 5).

2.3.1.4 Imaging Protocol for $T2_{app}$

A multi-TE ASL sequence was developed with imaging parameters: inflow times (TI) = 400 ms, 1000 ms, 1500 ms and 3500 ms, each inflow time was taken in an individual scan session except intermediate TI = 1000 ms and 1500 ms. Each acquired with a range of TE = 15 ms, 23 ms, 30 ms, 40 ms, 50 ms, 65 ms; TR = 5000 ms except for TI = 3500 ms where TR = 7000 ms, FOV = 25 x 25 mm; matrix size = 32 x 32; slice thickness = 2 mm; k_0 = 20, repetitions = 20.

2.3.1.5 Imaging Protocol for Cerebral Blood Flow & Arterial Transit Time Measurements

A multiple inflow time (multi-TI) ASL protocol was implemented for the arterial transit time measurements and the CBF estimation with sequence parameters: TI = 200 ms, 300 ms, 400 ms, 500 ms; echo time (TE) = 15 ms; repetition time (TR) = 5000 ms, field-of-view (FOV) = 25 x 25 mm; matrix size = 32 x 32; slice thickness = 2 mm; number of k-space line (k_0) = 20, repetitions = 20.

2.3.1.6 Imaging Protocol for BBI Permeability to Water Measurements

A multi-TE ASL sequence with imaging parameters: inflow times (TI) = 1000 ms and 1500 ms, TE = 15, 23, 30, 40, 50, 65 ms; TR = 5000 ms; FOV = 25 x 25 mm; matrix size = 32 x 32; slice thickness = 2 mm; k_0 = 20, repetitions = 20.

2.3.2 Data Analysis

Analysis was performed using Matlab R2015a (Mathworks Inc.) and GraphPad Prism 6 (GraphPad Software). Mean ASL images were generated by a pairwise subtraction of the control and labelled images at each echo time or inflow time, and averaged across all repetitions.

2.3.2.1 Extravascular Transverse Relaxation of static tissue, $T2_{EV}$

Multi-TE data acquired with the global inversion (control images), were used to generate T2 map for the static tissue. Data was fitted pixel-wise to an exponential decay, described in Eq (3) where T2 is equivalent to $T2_{EV}$. The manual ROI was derived from T2 maps across all of the inflow times, to visually avoid regions displaying partial volume effects (PVE) with the cerebral ventricles. T2 values derived from the cortical ROI was used to fix parameter, $T2_{EV}$, transverse relaxation of extravascular tissue, when evaluating the data using the two-compartment model.

2.3.2.2 Apparent Transverse Relaxation, $T2^{app}$

For cortical $T2_{app}$ analysis, ASL signal was extracted from a manually defined cortical region of interest (ROI) and was fitted to a monoexponential model, Eq (4), for each subject, at each inflow time. $T2_{app}$ maps were generated by fitting the ASL images across all echo times to a monoexponential decay model for visualisation purposes.

2.3.2.3 Cerebral Blood Flow, CBF

ASL signal extracted from the cortical region, at increasing inflow times were fitted to the model as described in **Eq (2)**. M_0, equilibrium magnetisation was needed for the CBF calculation, and was estimated using ASL signal intensity, from a single echo time (15 ms), and was fitted to the inversion recovery model to calculate the maximum signal intensity when the longitudinal relaxation has completely recovered, assuming T1 of cortical region to be 1.7 s.

2.3.2.4 Arterial Transit Time, δ_a

ASL signal intensities from the multi-TI sequence, at increasing inflow time were fitted to a linear model, as described in **Eq (2*)***. The model was extrapolatede through the inflow time axis to extract the arterial transit time (δ_a) for each animal.

2.3.2.5 Exchange Time, T_{ex}^{w} & Water Exchange Rate, K_w for measurement of BBI Permeability to Water

For T_{ex}^{w} measurements, ASL signal intensity from the multi-TE ASL data and mean $T2_{EV}$, were derived from the same cortical brain region, and processed using a three parameter (ΔM_{IV}, ΔM_{EV} and $T2_{IV}$) fit across all data sets using the two-compartment exponential model **Eq (5).** The output of fitting process was individual ΔM_{IV} and ΔM_{EV} contributions for each subject and a shared $T2_{IV}$ across all of the subjects.

The individual ΔM_{IV} and ΔM_{EV} contributions were used to calculate the intravascular fraction, **Eq (6).** ΔM_{IV} and ΔM_{EV} signal weightings were used together with the independent measurement of δ_a to extract tissue transit time (δ) from the two-compartment kinetic perfusion model **Eq (7)** and **(8)**, to be used to calculate the final cortical exchange time (T_{ex}^{w}). **Figure 2.4** shows flowchart of the multi-step analysis pipeline for T_{ex}^{w} measurements. The initial exchange time measurements from the animals in the protocol development group was calculated using two TI values (1000 ms and 1500 ms) and was averaged across both TIs to increase accuracy. The parameters that were measured are presented in **Table 2.1** and values used for the assumed variables are presented in **Table 2.2**.

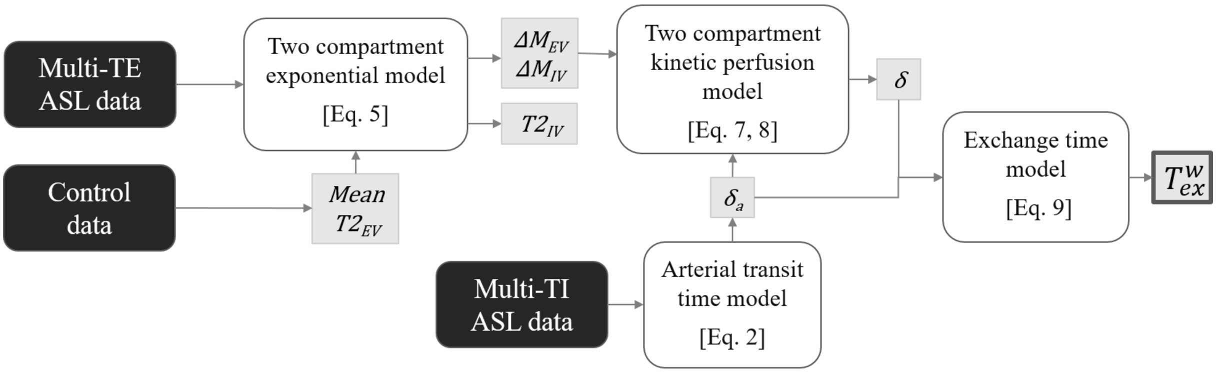

Figure 2.4: Flowchart for the analysis pipeline to determine exchange time (T_{ex}^{w}) from multi-TE ASL data, multi-TI ASL data and control data.

2.3.2.6 Statistical Analysis

All data are reported as the mean and associated error (± standard deviation). An unpaired students t-test was performed on the $T2_{app}$ and $T2_{EV}$ data in different air conditions. A Kruskal-Wallis test was performed on the $T2_{app}$ data at different inflow times. A paired student’s t-test was performed on the intravascular fraction data. For all tests, $p < 0.05$ was considered to indicate a statistically significant result. For results with $p < 0.01$ is denoted with two asterisks **, and $p < 0.001$ is denoted with three asterisks ***.

Measured variables		Units
Exchange time	T_{ex}^{w}	ms
Tissue transit time	δ	ms
Arterial transit time	δ_a	ms
Intravascular ASL signal	ΔM_{IV}	-
Extravascular ASL signal	ΔM_{EV}	-
Intravascular transverse relaxation	$T2_{IV}$	ms
Extravascular transverse relaxation	$T2_{EV}$	ms
Apparent transverse relaxation	$\mathrm{T2_{app}}$	ms
Cerebral blood flow	f	ml/100g/min
Equilibrium magnetisation	$\mathrm{M_0}$	-

Table 2.1: Parameters that are measured from the data

Assumed variables		Fixed Value
Blood-brain partition coefficient	λ	0.9
Longitudinal relaxation rate (blood)	$\mathrm{R1_a}$	1/2.4s
Longitudinal relaxation rate (tissue)	$\mathrm{R1_{app}}$	1/1.7s
Temporal length of tagged bolus	τ	2.0s

Table 2.2: Values of the assumed variables used in the models

2.4 Results

2.4.1 Pilot Study: Effects of Oxygenation on $T2_{app}$

The systemic oxygen saturation level of an individual mouse was measured in two inhalation air mixture conditions: medical air and oxygen using a pulse oximeter. The result of the systemic oxygen saturation level in both air mixtures, during a 10-minute period, **Figure 2.5A**. For medical air conditions, the mean oxygen saturation level = 96.6 ± 0.6 % and in oxygen conditions, mean oxygen saturation level = 98.3 ± 0.2 %. There is a clear separation of the systemic oxygenation in the two air mixture condition which implies that there would be a change in the oxygenation levels in the arterial blood that supplies the brain. The change in the oxygenation level will alter the spin-spin interaction, known to be highly sensitive to the presence of deoxyhaemoglobin, and is likely to have an effect on the apparent transverse relaxation of the ASL signal.

The results of apparent transverse relaxation, $T2^{app}$ with the animals breathing 1.0ml/min medical air or 1.0ml/min oxygen are shown in **Figure 2.5B**. There is a significant increase in $T2_{app}$ from 30.9 ± 1.5 ms in medical air conditions to 34.0 ± 1.4 ms in oxygen conditions, $p = 0.009$. This is caused by the change in the spin-spin interaction when the systemic blood oxygenation level increases. The T2 of the extravascular tissue ($T2_{EV}$) derived from the control images shows a subtle difference in the medical air conditions (36.1 ± 1.2 ms) and in the oxygen conditions (37.2 ± 1.5 ms), $p = 0.222$. This highlight the sensitivity of the ASL signal to the changes in the blood oxygenation and a substantial part of this signal derives from the blood when assessing $T2_{app}$. This initial pilot data provides a degree of confidence in the interpretation of the multi-TE ASL signal and the sensitivity of the method.

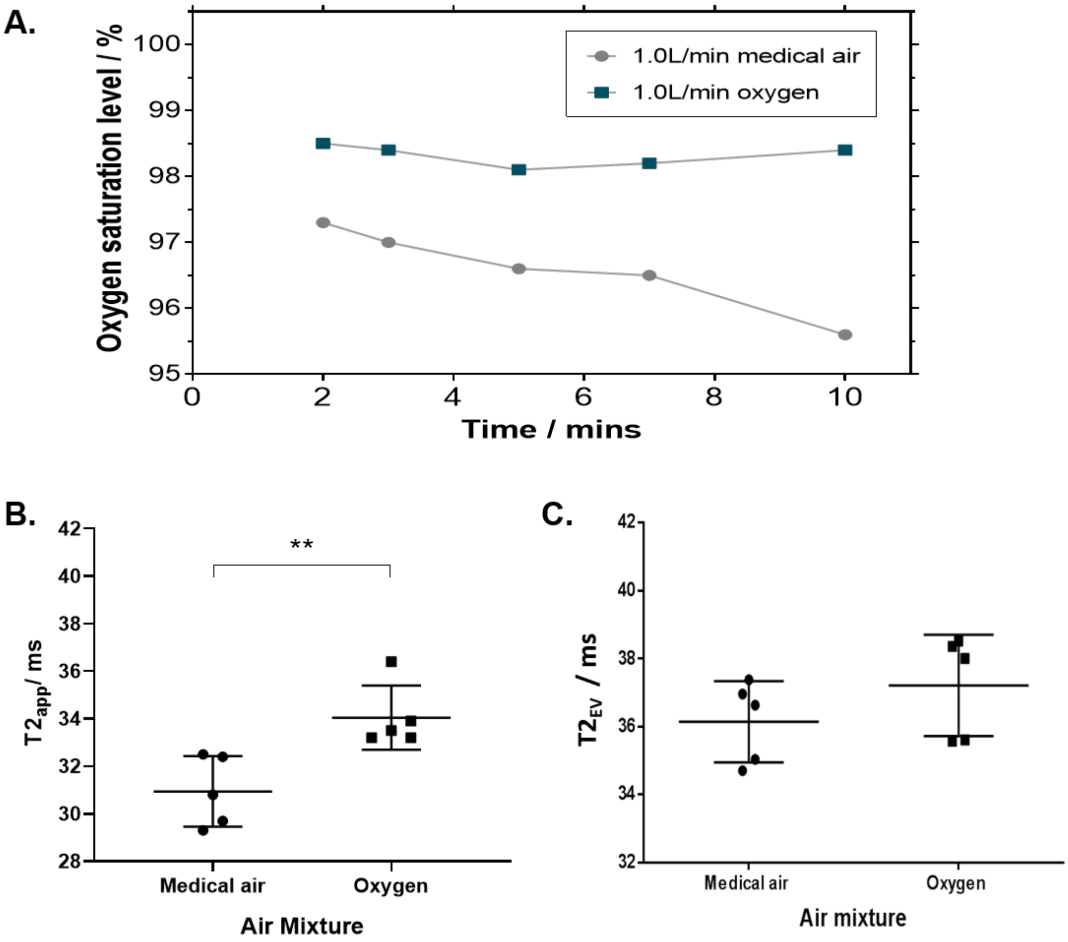

Figure 2.5: Effect of air mixture on $T2_{app}$. **A.** Oxygen saturation level in air mixture conditions: 1.0ml/min medical air and 1.0ml/min oxygen **B.** Apparent transverse relaxation $T2_{app}$ and **C.** extravascular tissue transverse relaxation ($T2_{EV}$), for individual animals breathing two air mixtures with mean value and associated error (± std) indicated on plot.

$T2_{app}$ will derive from the combination of IV and EV signal components, but predominantly systemic oxygenation has an effect on the T2 derived from arterial blood compartment. The IV-EV signal components need to be separated in the two-compartment model to be able to measure the exchange time. When $T2_{app}$ is higher due to an increased level of systemic blood oxygenation (oxygen air mixture), it will make it harder to separate $T2_{IV}$ of the arterial blood from the $T2_{EV}$ of extravascular tissue as their values will be closer together. When there is a larger difference between the T2 of IV and EV spaces it will make the compartments more distinguishable, and the bi-exponential fitting is more reliable. Therefore, the final imaging protocol has been optimised with an air mixture of 1.0L/min medical air to allow greater separation in the $T2_{IV}$ and $T2_{EV}$ values.

2.4.2 Assessment of BBI Permeability to Water in Mouse Brain

A progressive increase in $T2_{app}$ with inflow time is measured in the cortical brain region from 21.6 ± 2.6 ms at TI = 400 ms to 34.0 ± 2.6 ms at TI = 3500 ms ($p = 0.0003$), **Figure 2.6,** with representative $T2_{app}$ maps at each inflow time, **Figure 2.6A.** $T2_{app}$ at TI = 400 ms corresponds to arterial blood T2 at 94.2% oxygen saturation from previous calibration experiments at 9.4T [116] and $T2_{app}$ at TI = 3500 ms was 34.0 ± 2.6 ms, which tends closely towards the T2 value of cortical tissue (~37 ms). This provides evidence that the technique is sensitive to the transfer of labelled blood water moving across the BBI into the extravascular tissue of the mouse brain as TI increases.

A relatively balanced contribution from both the intravascular (IV) and extravascular (EV) compartments was demonstrated at TI = 1000 ms and 1500 ms with $T2_{app}$ = 27.2 ± 1.4 ms and $T2_{app}$ = 31.2 ± 1.0 ms respectively, which lie between $T2_{IV}$ ~ 15 ms [116, 125] and $T2_{EV}$ ~ 37 ms [126]. Hence, the analysis was extended by fitting the ASL signal to a bi-exponential model to separate the IV and EV signal contributions at these intermediate TIs, **Figure 2.6C**. The intravascular fraction confers the proportion of labelled blood water residing in the IV compartment with 'fast-decaying' signal derived from the arterial blood ($T2_{IV}$). A significant reduction in the intravascular fraction from 0.50 ± 0.07 to 0.30 ± 0.06 is reported as the TI increases from 1000 ms to 1500 ms ($p = 0.001$), **Figure 2.6D**.

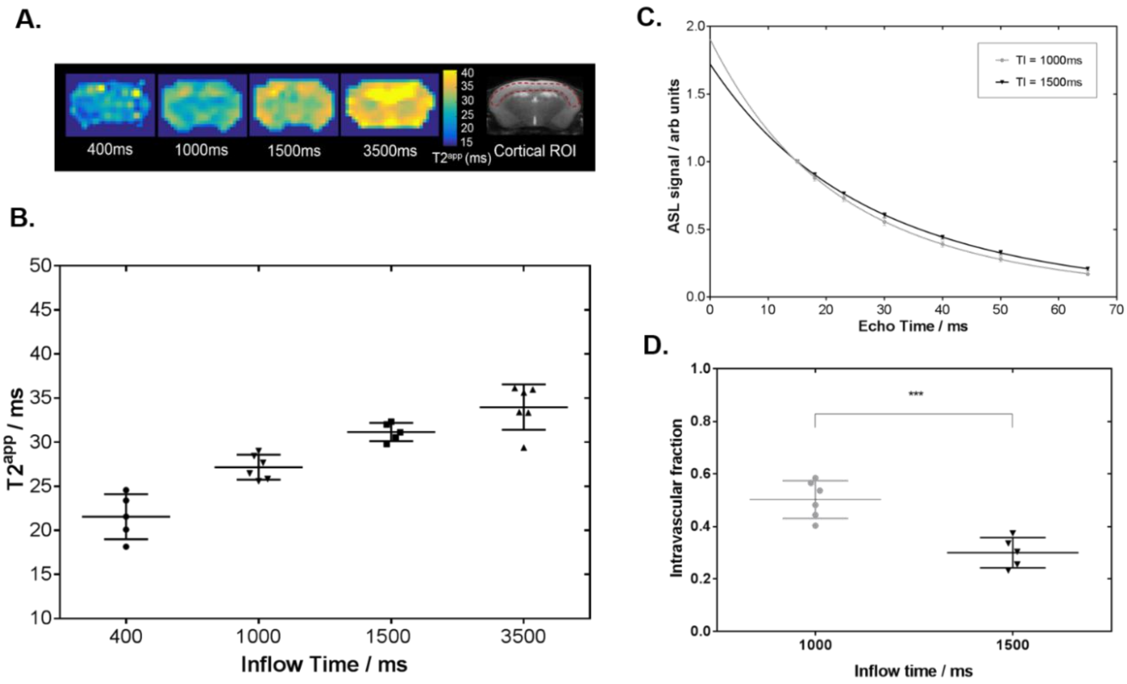

<u>Figure 2.6: Modelling the multi-TE ASL signal</u>. A. Representative $T2_{app}$ map at increasing inflow times (indicated on each image) for a single subject, with an anatomical reference image shown with cortical ROI in red, for illustration purposes. **B.** $T2_{app}$ at increasing inflow times fitted to single compartment model for individual subjects, p = 0.003. **C.** The mean cortical signal across all subjects fitted to the two-compartment model at TI = 1000ms and 1500ms. **D.** The intravascular fraction of the ASL signal determined for the individual subjects at TI = 1000 ms and 1500 ms using the two-compartment model. The mean parameter and associated error (± std) are displayed with each marker representing the individual animals. *** indicates $p < 0.001$.

The $T2_{IV}$ of 16.0 ± 1.7 ms at 1000 ms and to 16.3 ± 2. 6ms at 1500ms. The extravascular $T2_{EV}$ = 36.1 ± 1.1 ms (at 1000 ms) and $T2_{EV}$ = 36.2 ± 1.2 ms (at 1500 ms). CBF was measured at 277 ± 105 ml/100g/min which is within the expected range for the cortical region of the mouse brain, **Figure 2.7A, C**. The mean arterial transit time (δ_a) was calculated to be 157 ± 29 ms, **Figure 2.7A**, and from the fit to the kinetic two compartment perfusion model, mean cortical exchange time was calculated to be 395 ± 54 ms.

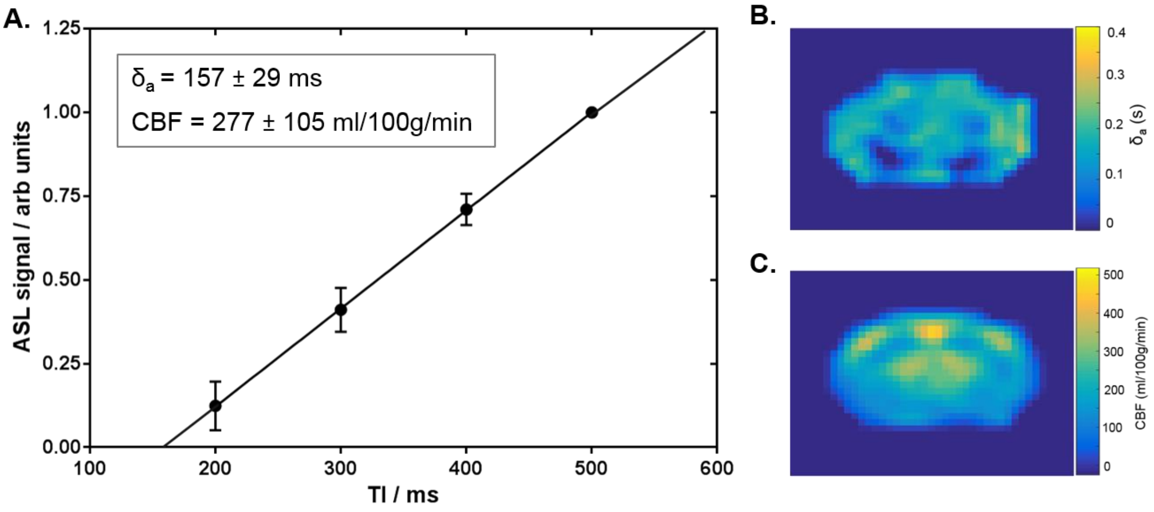

Figure 2.7: Modelling ASL signal at short inflow times. **A.** The normalised mean cortical signal across all subjects fitted to a linear model with mean value and associated error (± std) displayed. **B.** Representative arterial transit time (δ_a) map for an individual subject. **C.** Representative cerebral blood flow (CBF) map for an individual subject. Respective scale bars are displayed.

2.5 Discussion

A multi-TE ASL imaging protocol was established and implemented in the mouse brain to enable the assessment of BBI permeability to water. The methodological developments described in this chapter have enabled the acquisition of multi-TE ASL data in the mouse brain to measure the exchange time of vascular water into cortical tissue, despite the small size and inherently low SNR of the ASL technique in this application. The apparent transverse relaxation ($T2_{app}$) increases as the inflow time increases to provide evidence that the technique is a sensitive correlate of the proportion of intravascular and extravascular labelled blood water. Selected intermediate inflow times (TI = 1000 ms and TI = 1500 ms) allow the ASL data to be fitted to a two-compartment model that was able to estimate both intravascular (IV) and extravascular (EV) contributions. This represents the first non-invasive estimate of the BBI permeability to water in the mouse brain, and, as such, provides the foundation for application of this translational technique to mouse models of disease and BBI abnormalities.

A pilot study was performed to investigate the effect of the oxygen/air inhalation mixture, and hence the systemic oxygenation of the animals on the $T2_{app}$ measurements. The systemic oxygen saturation level is ~2% higher when the mice are breathing 21% oxygen (1.0L/min) compared to when they are breathing an 100% medical air (1.0L/min), **Figure 2.4A**. There was a significant increase in the $T2_{app}$ between the oxygen air mixture and the medical air mixture which is likely to be associated with the change in systemic oxygen level (**Figure 2.4A, B**). There is a small separation in the $T2_{EV}$ which may be due to extravascular blood-oxygenation level dependent (BOLD) effects, (**Figure 2.4C**) [127]. The comparison between $T2_{app}$ and $T2_{EV}$ in the different air mixture conditions would indicate that the systemic oxygenation has a greater effect on the IV compartment than the extravascular tissue, as hypothesised. This result goes some way to verifying the model fitting approach (where a proportion of the ASL signal is assumed to derived from labelled IV blood water at TI = 1500 ms) and the sensitivity of the optimised methodology. An increase in $T2_{IV}$ will have an impact on the bi-exponential fitting when the signal is modelled using a two-compartment model. A lower $T2_{IV}$ will facilitate the separation of IV and EV compartments using multi-TE ASL technique, hence the inhaled gas composition used in the final experiments was 100% medical air.

Changing the chosen inflow time (TI) provides a means of modulating the proportion of labelled water molecules in the intravascular (IV) and extravascular (EV) compartments during the image acquisition phase. It was hypothesised that as the TI increased, the proportion of labelled water in the EV compartment would increase, as greater time is allowed for the labelled bolus of IV water to exchange across the BBI. Consistent with this hypothesis, a gradual increase in $T2_{app}$ was observed as TI was increased from 400 ms to 3500 ms **(Figure 2.3B)**. These measurements provide evidence that the technique presented here is sensitive to the movement of labelled blood water across the BBI into extravascular tissue. The results in this study are comparable to previous $T2_{app}$ data from rat cortical brain tissue [109], but measurements reported here have been extended to both shorter and longer inflow times to further shift the likely source of the labelled blood water to the IV or EV compartment respectively.

The water flux across the BBI can be estimated when a relatively balanced proportion of labelled blood water resides in the IV and EV compartments, therefore the two-compartment model can be successfully applied to the ASL signal. At intermediate inflow times of TI = 1000 ms and TI = 1500 ms, the proportion of spins measured by the intravascular fraction are 0.5 and 0.3 respectively. The intravascular fraction is comparable to the relative amount of labelled water reported in the human brain, where intravascular fraction was measured at 0.39, 0.26 and 0.15 at TI = 800 ms, 1200 ms and 1500 ms respectively, when ASL was combined with a diffusion-weighted (DW) MRI sequence [96].

The estimates of the IV fraction at TI = 1000 ms and 1500 ms were integrated into a kinetic model to calculate the tissue transit time (δ) for each mouse. In order to account for possible differences in arrival time, in this study, the arterial transit time (δ_a) was measured in a separate, short TI, acquisition. The mean cortical T_{ex}^{w}, time was measured at 395 ± 54 ms, providing a quantitative, surrogate index of BBI permeability to water. The T_{ex}^{w} measurement is highly similar to that of the rat cortical brain tissue [109], estimated using a similar approach. T_{ex}^{w} is also comparable to the transfer time parameter ($T_{bl\text{-}ex}$) derived from the grey matter in the human brain where $T_{bl\text{-}ex}$ was 440 ± 30 ms, using a T2-ASL method [108]. Further work must be done to relate these values to establish a gold standard measurement. This could be achieved using radiolabelled water with positron emission tomography (PET), although it is unknown whether such techniques are able to distinguish changes to such rapid water exchange timescales as observed here.

Multi-TE ASL is attractive because it offers a non-invasive approach to assess BBI water permeability. Conventionally, BBI permeability dysfunction is measured using dynamic contrast enhanced (DCE) MRI which requires contrast agents such as gadolinium. DCE-MRI detects gross BBI defects when a marked breakdown of endothelial tight junctions permits large contrast agent molecules to egress into the brain parenchyma. Detecting changes in BBI permeability to water may identify distinct pathological processes at the BBI that may occur at earlier stages of neurodegenerative disease progression prior to the opening of the endothelial layer. DW-ASL techniques have been used to determine the water exchange rate, K_w [128, 129], reported at 252 ± 38 min^{-1} [129] in rat brain, 193 ± 50 min^{-1} [96] and 110 ± 18 min^{-1} in human grey matter [128] and 126 ± 18 min^{-1} in human white matter [128]. Multi-TE ASL and DW-ASL eliminates the need to inject MRI tracers for permeability measures, and though these agents are used routinely in the clinical setting, there is increasing speculation about the potential harm that repeated doses may cause to patients in the long term [91]. Therefore, there may be further clinical benefits to non-invasive measure of BBI permeability to water.

2.6 Conclusion

Overall, the multi-TE ASL protocol implemented in the mouse brain was able to generate ASL data that was applied to the two-compartment kinetic perfusion model to estimate BBI permeability to water in the cortical region of the mouse brain. The development of the multi-TE ASL technique in the mouse brain will allow its application to mouse models of neurodegeneration and specific BBI abnormalities, to further explore the dynamic role of vascular water exchange across the BBI in disease conditions.

2.7 Appendix: Model Comparison

Akaike's Information Criterion (AIC) [130] was performed to assess the preferred model fitting for the ASL signal decay; between a mono-exponential one compartment model or a three-parameter fit for bi-exponential two compartment model.

The fitted parameters for the one compartment model were the equilibrium magnetisation (M_0) and the apparent transverse relaxation ($T2_{app}$), eq. **(4)**. The fitted parameters for the two compartment model were individual intravascular ASL signal weighting (ΔM_{IV}), individual extravascular ASL signal weighting (ΔM_{EV}) and shared intravascular transverse relaxation ($T2_{IV}$), eq **(5)**. The best fit values ± 2σ (95% confidence interval (CI)) for ASL signal decay at TI = 1000 ms for individual animals are presented in **Table 2.3**.

Animal ID	**One compartment model**		**Two compartment model**		
	M_0	**$T2_{app}$ (ms)**	**ΔM_{IV}**	**ΔM_{EV}**	**Shared $T2_{IV}$ (ms)**
1	1.5 ± 0.14	28.4 ± 4.8	0.77 ± 0.14	0.85 ± 0.10	16.0 ± 2.6
2	1.3 ± 0.20	25.6 ± 6.4	0.70 ± 0.14	0.72 ± 0.09	
3	1.6 ± 0.27	26.5 ± 5.2	0.94 ± 0.14	0.69 ± 0.10	
4	1.6 ± 0.18	25.8 ± 4.3	0.99 ± 0.14	0.74 ± 0.11	
5	1.6 ± 0.09	27.6 ± 2.2	1.0 ± 0.14	0.77 ± 0.11	
6	1.5 ± 0.18	29.0 ± 5.2	0.77 ± 0.13	0.81 ± 0.09	

Table 2.3: Best fit values ± 2σ (95% confidence interval) for one compartment and two compartment models for the equilibrium magnetisation (M_0), apparent transverse relaxation ($T2_{app}$), intravascular (ΔM_{IV}) and extravascular (ΔM_{EV}) ASL signal intensities for individual animals and shared intravascular transverse relaxation ($T2_{IV}$) across group at inflow time (TI) = 1000ms.

The 95% CI for ΔM_{IV}, ΔM_{EV} and shared $T2_{IV}$ from the two compartment model are smaller compared to the confidence intervals output for M_0 and $T2_{app}$ from the one compartment model. This would indicate that there is an increase in the precision of the three-parameter fit bi-exponential, two compartment model compared to the mono-exponential one compartment model.

The preferred model is the three-parameter fit for the two compartment model with > 99.99% probability that it is correct. The difference between the AIC of the two models is -27.8. This provides evidence to support the use of the three-parameter fit bi-exponential model over the mono-exponential model.

Chapter 3

Application of Multiple Echo Time Arterial Spin Labelling technique to target Aquaporin-4 Mediated Brain Clearance Pathways

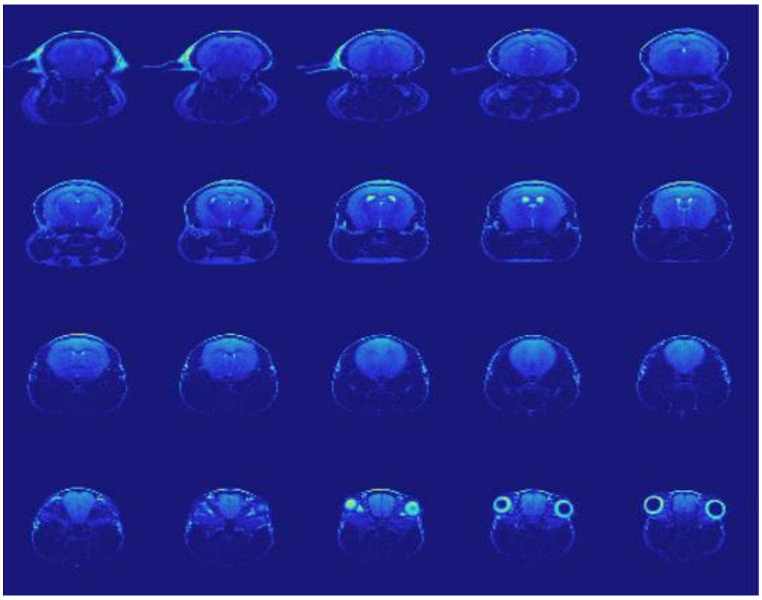

Anatomical MS-FSE Image, Aquaporin-4 deficient mouse brain

Aim

The overall aim of this chapter is to non-invasively assess aquaporin-4 (AQP4) mediated brain clearance pathways. Brain clearance pathways are important in maintaining the homeostasis of the brain, and failure of these routes may lead to, or exacerbate, many neurological diseases such as Alzheimer's Disease (AD). Brain AQP4 water channel appear to play a key role in the clearance of deleterious proteins, particularly amyloid-β. Many aspects of AQP4 have been discovered using immunohistochemical techniques and animals models [33], yet the lack of non-invasive techniques that able to directly probe this pathways currently limits understanding of their precise role in pathology.

In this chapter, the multi-TE ASL technique was applied to a cohort of mice lacking AQP4 water channels (*Aqp4*$^{-/-}$) developed by our collaborators, O.P. Ottersen (Karolinska Institutet, Sweden) and E.A Nagelhaus (University Oslo, Norway). The benefits of applying the technique to a genetic mouse model is that the role of AQP4 in water exchange at the blood brain interface (BBI) is completely isolated. This will provide insight into the sensitivity of the technique to AQP4 expression in controlled experimental conditions, before future application to mouse models of ageing which likely models multiple changes to the BBI.

The optimised imaging protocol, presented in **Chapter 2**, was applied to *Aqp4*$^{-/-}$ mice and wild-type (WT) controls to estimate cortical vascular water exchange rate, as a surrogate index of blood-brain interface (BBI) permeability to water. Cerebral blood flow (CBF), apparent diffusion coefficient (ADC) and arterial transit time (δ_a) are also estimated using more established imaging protocols. To date, there have been no reports of non-invasive tools able to successfully probe AQP4 polarisation. Therefore, this work represents novel approach for targeting AQP4, and may provide a clinically viable tool to better understand the dynamic role of AQP4 in brain protein clearance mechanisms.

This work was presented as a power pitch at ARUK 2018 conference, London, as an e-poster at ISMRM 18, Paris, France and as an oral presentation at the Alzheimer's Imaging Consortium and a poster at AAIC 2018, Chicago, USA.

3.1 Introduction

Regulating brain water transport is vital to brain homeostasis and dysfunction is associated with several neurological conditions such as meningitis, traumatic brain injury and cerebral edema [31, 38, 131, 132]. Parenchymal osmoregulation is supported by brain aquaporin-4 (AQP4) channels, trans-membrane proteins that are highly polarised to astrocytic endfeet, that facilitate bi-directional flux of water [33, 37].

A brain-wide waste removal pathway, coined the glymphatic system, describes the exchange of cerebrospinal fluid (CSF) and interstitial fluid (ISF), a transition strongly mediated by AQP4. AQP4 channels are critical to glymphatic function and appear to play a key role in clearance of deleterious proteins such as amyloid-β (Aβ) [45]. Studies report ~70% decrease in glymphatic function in mice lacking AQP4 channels, which likely contributes to the measured ~55% decrease in rates of Aβ clearance from the brain parenchyma in the same AQP4-deficient animals [45]. Further studies indicate that when AQP4 no longer remains polarised to the astrocytic endfeet there is a reduction in glymphatic function [133]. In agreement, loss of perivascular AQP4 is associated with accumulation and misagregation of amyloid [51, 112].

Many of the methods for assessing the role of AQP4 in brain clearance pathways are highly invasive and not clinically applicable [36, 38, 45]. Therefore, the development of non-invasive tools for the assessment of AQP4 expression/polarisation would be highly beneficial to advance our understanding of AQP4 mediated clearance of waste products and neurotoxic proteins from the brain. Ultimately this may lead to new approaches for early diagnosis and effective therapeutic intervention in neurodegenerative diseases.

To address the lack of non-invasive tools available to assess water transport mechanisms, I developed a multiple echo time (multi-TE) ASL technique for the mouse brain parenchyma, to measure the water flux at the BBI as a surrogate index of BBI permeability to water, presented in **Chapter 2**. Altered BBI water permeability, possibly mediated by AQP4, may provide an early indication of neuropathology [87] and therefore has potential as a clinically viable biomarker of diseases such as Alzheimer's Disease.

While there are several transport mechanisms for water passing across the BBI [134, 135], AQP4 provides a 'path of least resistance' which supports the rapid flux of water molecules into the brain parenchyma [31, 36, 136]. The absence of AQP4 appears to have a marked effect on BBI permeability to water, as reported by ~9-fold decrease within AQP4-deficient mice using invasive techniques [38]. An important motivation for the novel methodological development to the mouse brain, presented in **Chapter 2**, was the potential to apply this technique to genetic mouse models of neurodegeneration and other mouse models of specific BBI abnormality. In this study, the multi-TE ASL protocol for the mouse brain is applied to *Aqp4*$^{-/-}$ mice to estimate BBI permeability to water. The genetic removal of AQP4 channels allows controlled experimental conditions to assess the sensitivity of the technique to record changes in AQP4-mediated water flux across the BBI. I hypothesize that impaired water transport mechanisms in *Aqp4*$^{-/-}$ mice will be detectable via an associated increase in water exchange time, **Figure 3.1**. If so, the non-invasive multi-TE ASL technique may provide a novel tool to assess AQP4 polarisation at the BBI in order to better understand the dynamic role of AQP4 in water transport mechanisms and brain clearance pathways.

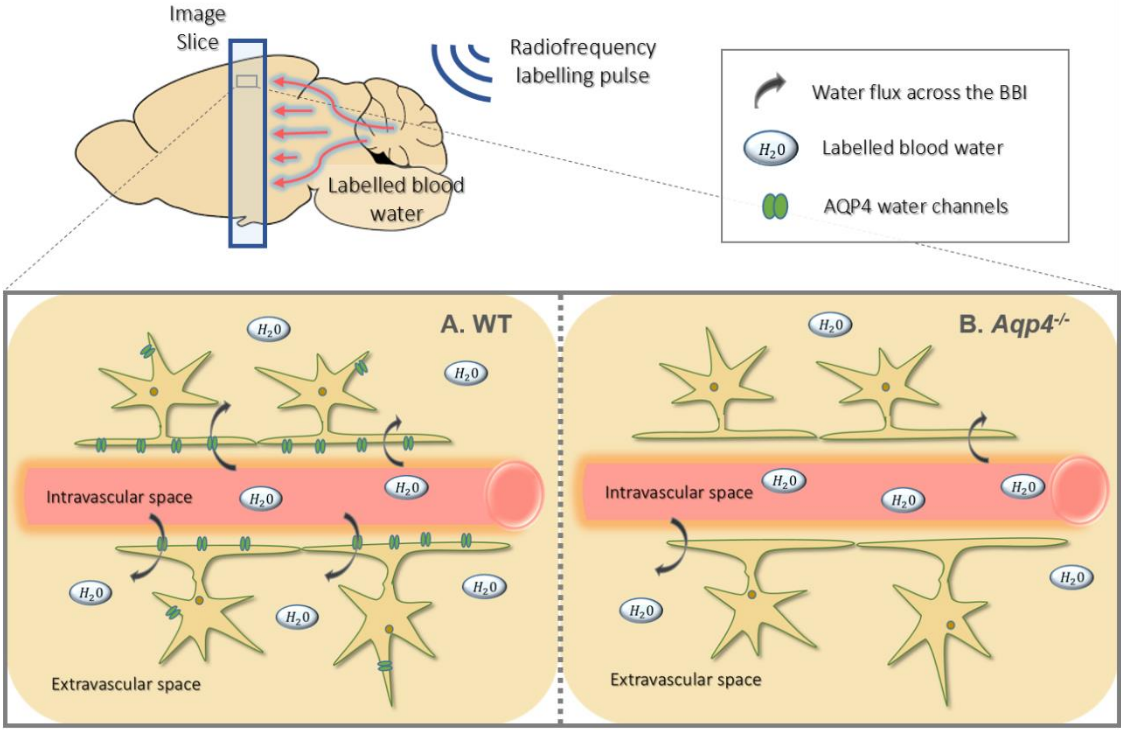

Figure 3.1: Schematic of ASL labelling scheme and labelled blood water transfer from intravascular space to extravascular tissue space. A. Labelled blood water molecules exchange into the extravascular space via all water transport mechanisms including aquaporin-4 (AQP4) water channels in wild-type (WT) mice. **B.** In the absence of AQP4, in AQP4-deficent mice (*Aqp4*$^{-/-}$), the water transport mechanisms are restricted and only occur through cotransport with organic molecules and by diffusion through the lipid bilayer of the plasma membrane.

3.2 Method

3.2.1 Experimental Protocol

3.2.1.1 Animal Preparation

All experiments were performed in mice in accordance with the European Commission Directive 86/609/EEC (European Convention for the Protection of Vertebrate Animals used for Experimental and Other Scientific Purposes) and the United Kingdom Home Office (Scientific Procedures) Act (1986). All mice were acclimatised two weeks prior to data acquisition in an animal house maintained at a temperature of 21 ± 2 °C and a relative humidity of 55 ± 10%, on a 12 h light/12 h dark cycle with food and water provided *ad libitum*.

Male *Aqp4*$^{-/-}$ mice at 6 months old (n = 9) [137] and male WT age-matched controls (C57/Bl6) (n = 9) (Charles River Laboratories) were used to evaluate the contribution of AQP4 in BBI permeability to water measurements as well as cerebral blood flow (CBF), arterial transit time (δ_a) and apparent diffusion coefficient (ADC) measurements.

All animals were induced in 2% isoflurane anesthetic in a mixture of 1.0 L/min medical air, and the isoflurane level was manually adjusted throughout the scans to maintain the respiration rate at ~100 bpm. Core body temperature was monitored using a rectal probe (SA Instruments) and maintained at 37 ± 0.5°C via regulation of an adjustable temperature water bath. Animals were secured into the MRI cradle with a nose cone, ear bars and bite bar to minimise head movement during the scan.

3.2.1.2 Image Acquisition

Images were acquired using a 9.4T VNMRS horizontal bore MRI scanner and the equipment set-up, shimming and anatomical reference images were acquired as outlined in **Chapter 2: Methods: Image Acquisition.**

The main ASL imaging protocol was based on a flow-alternating inversion recovery (FAIR) sequence with parameters outlined in **Chapter 2: Methods: Image Acquisition**. Multi-TE ASL was implemented to measure the water flux across the BBI to assess AQP4 contribution. Sequence parameters were: inflow time (TI) = 1500 ms, echo time (TE) = 15 ms, 23 ms, 30 ms, 40 ms, 50 ms, 65ms; repetition time (TR) = 5000 ms, field-of-view (FOV) = 25 x 25 mm; matrix size = 32 x 32; slice thickness = 2 mm; partial-fourier acquisition k_0 = 20 (16 + 4 k-space lines acquired); repetitions = 15.

The arterial transit time (δ_a) and cerebral blood flow (CBF) was calculated using a separate multiple short inflow time (multi-TI) ASL acquisition. The multi-TI protocol used the following sequence parameters: TI = 200 ms, 300 ms, 400 ms, 500 ms; echo time (TE) = 12 ms; repetition time (TR) = 5000 ms, field-of-view (FOV) = 25 x 25 mm; matrix size = 32 x 32; number of k-space line (k_0) = 20, repetitions = 10.

Apparent diffusion coefficient (ADC) estimates the molecular motion of water in the targeted brain region, and provides an indication of parenchymal water mobility. This was evaluated to assess any tissue differences in measured ADC of the parenchymal tissue between the *Aqp4*$^{-/-}$ and WT animals. ADC was estimated using a two b-value approach with diffusion gradients applied in a single slice select direction: b-values = 0 and 1030.5 s/mm^2; TE = 23.82 ms; TR = 2500 ms; data matrix = 64 x 64; slice thickness = 1.0 mm; repetitions = 10 for both b-values and spin-echo EPI readout.

Diffusion images were averaged across all of the repetitions for each b-value. The diffusion images were used to extract the signal from cortical ROI corresponding to the same region used to measure T_{ex}^{w}, δ_a and CBF. Diffusion-weighted signal was fitted to the standard mono-exponential diffusion model to estimate the ADC.

3.2.2 Quantification of *Aqp4* mRNA Expression

For quantification of *Aqp4* mRNA expression in cortical brain region, three WT mice and three *Aqp4*$^{-/-}$ mice were euthanised by overdose with sodium pentobarbital (10ml/kg, intra-peritoneal), the brain rapidly removed, hemisected, and the cortex dissected and snap frozen in isopentane pre-chilled on dry ice.

Total RNA from each brain region was extracted using the RNeasy® Plus Microkit (Qiagen, UK). Total RNA was converted to cDNA using the QuantiTect® Reverse Transcription Kit (Qiagen), which was quantified using the Eppendorf Mastercycler with Realplex software (v1.5, Eppendorf, UK) and the TaqMan® Gene Expression master mix (Applied Biosystems, UK). TaqMan® Gene Expression assays for *Aqp4* and reference housekeeper genes (β-Actin (*ACTB)* and *GAPDH*) were used, and *Aqp4* expression level determined using the $2^{-\Delta\Delta Ct}$ method [138] with the signal threshold set at 1000, normalising to mRNA expression in the wild-type cortex.

The optimisation of experimental protocol and quantification of *Aqp4* mRNA expression for this study was performed by M.Sc. student Eleanor Bird.

3.2.3 Data Analysis

Analysis was performed using Matlab R2015a (Mathworks Inc.). Mean ASL images were generated by a pairwise subtraction of the control and labelled images at each echo time or inflow time, and averaged across all repetitions. The analysis pipeline for the exchange time (T_{ex}^{w}) measurements is outlined in **Chapter 2: Methods: Data Analysis: BBI Permeability to Water Measurement via Exchange Time and Water Exchange Rate.**

The whole brain region for each subject was manually segmented to generate a mean exchange time map for each animal group for visualisation. This was achieved by fitting the two-compartment model using $T2_{EV}$ maps, arterial transit time maps, and fixed mean cortical $T2_{IV}$ for each individual animal. The ventricular regions were manually segmented and excluded from the analysis since the two-compartment model fails within this region as there is no ASL signal. The exchange time maps were registered together and averaged for each animal group.

All data are reported as the mean and associated error (± standard deviation). All analysis was performed using GraphPad Prism 6 (GraphPad Software). A two-tailed student's t-test was performed on data from WT and *Aqp4*$^{-/-}$ animals to compare T_{ex}^{w}, intravascular fraction, δ_a, CBF, ADC, $T2_{EV}$ and mRNA expression measurements. For all tests, * $p < 0.05$ was considered to indicate a statistically significant result. For results with $p < 0.01$ is denoted with two asterisks **.

3.3 Results

Using the multi-TE ASL imaging protocol to map the exchange times, a 31% increase in T_{ex}^{w} was measured in cortical brain tissue of the AQP4-deficient mice when compared to the WT mice (452 ± 90 ms and 343 ± 91 ms respectively; $p = 0.02$),

Figure 3.2A, B. The intravascular fraction at TI = 1500 ms is larger in the *Aqp4*$^{-/-}$ mice (0.356 ± 0.065) compared to the WT controls (0.273 ± 0.070), p = 0.02. This reflects slower movement of labelled vascular water into the extravascular cortical tissue in the absence of AQP4 channels. Expression of AQP4 mRNA was confirmed using quantitative real time polymerase chain reaction (qRT-PCR) which indicates that *Aqp4* mRNA is absent from the *Aqp4*$^{-/-}$ mice in **Figure 3.3.**

$T2_{IV}$ measured by 3-parameter fit of ASL signal decay was 19.7 ± 3.3 ms in WT animals and 20.4 ± 2.3 ms in *Aqp4*$^{-/-}$ animals. This would indicate that the oxygenation of the intravascular compartment is consistent between the *Aqp4*$^{-/-}$ mice and the WT controls. Extravascular tissue, $T2_{EV,}$ from the control data was measured at 35.8 ± 1.3 ms in WT animals and $T2_{EV}$ = 37.4 ± 0.8 ms in *Aqp4*$^{-/-}$ animals, p = 0.010. The increase in extravascular tissue T2 might reflect the slight increase in the water content of the AQP4-KO mice.

There is no detectable difference in the arterial transit time of vascular water to the cortical brain region between WT mice, δ_a = 166 ± 40 ms and *Aqp4*$^{-/-}$ mice, δ_a = 166 ± 16 ms (p = 0.54), **Figure 3.2C**. This provides evidence that there are no marked differences in the arterial vascular architecture in the two animal cohorts. The arterial transit times are also consistent with those previously measured in the cohort of WT mice outlined in **Chapter 2: Results**. Mean cortical CBF was 310 ± 57 ml/100g/min in WT mice and 273 ± 54 ml/100g/min in *Aqp4*$^{-/-}$ mice (p = 0.19), which also suggests there to be preserved cerebral hemodynamics between both animal group, **Figure 3.2D**. Taken together this indicates that the measured differences in the cortical exchange time between animal groups are not due to alterations in the dynamics of the arterial blood supply. There are no measurable differences in parenchymal water mobility between the two groups as ADC values from the same cortical brain region were 8.85 ± 0.32 x 10^{-4} mm^2/s in WT mice and 8.83 x 10^{-4} mm^2/s in *Aqp4*$^{-/-}$ mice (p = 0.87) (**Figure 3.2E**).

The data shows that the absence of AQP4 water channels has no significant impact on δ_a , CBF or ADC measurements, which is consistent with previous reports indicating a relatively mild phenotype of this mouse model which, with some exception [33], only displays clear differences to WT animals in pathophysiological conditions [37, 139].

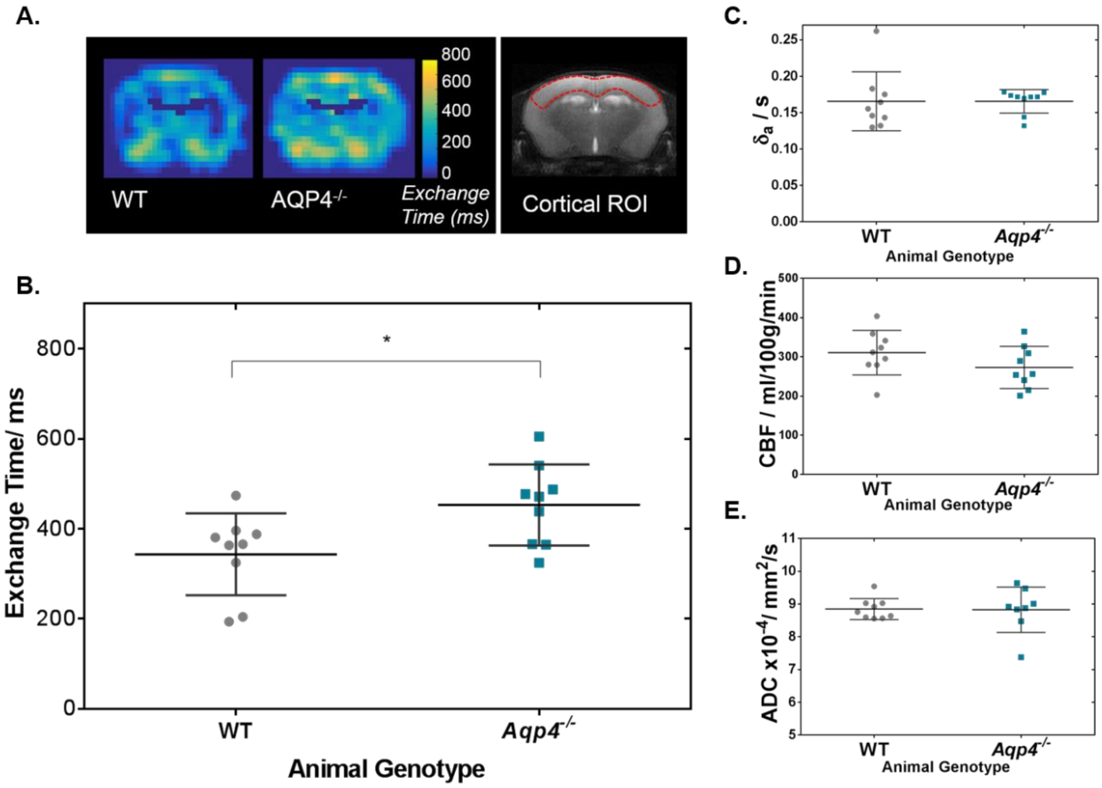

Figure 3.2: Time of exchange of labelled blood water into cortical tissue. **A.** Average exchange time maps for all animals (scale bar shown) and an anatomical reference of the cortical brain region for individual analysis, for illustration purposes. **B.** The mean cortical exchange time measurements for individual animals. **C.** Mean cortical arterial transit time (δ_a) for individual animals. **D.** Mean cortical CBF for individual animals **E.** Mean cortical ADC measured in individual animals. Group mean parameter and associated error (± std) are displayed on each plot, (n=9). * indicates $p < 0.05$.

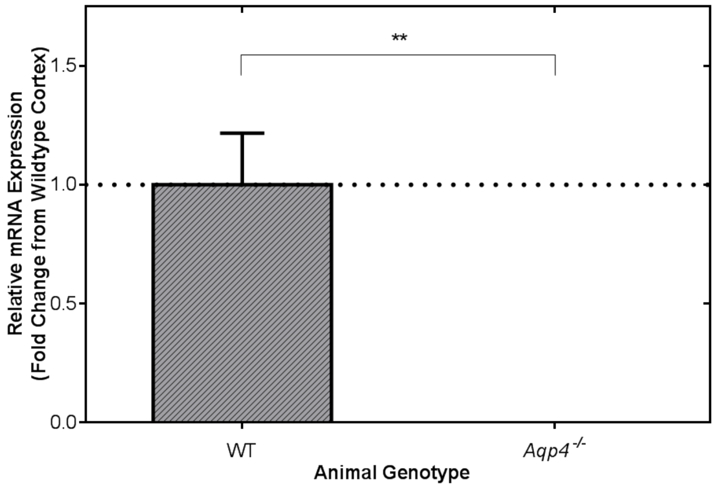

Figure 3.3: Cortical *Aqp4* mRNA expression of wildtype (WT) and Aquaporin- 4 deficient (*Aqp4*$^{-/-}$) mice. Normalised to the WT cortex (n = 3 in each group). ** indicates $p < 0.01$

3.4 Discussion

In this study, the measurements of BBI permeability to water using multiple echo time (multi-TE) ASL technique are sensitive to the presence of AQP4. A 32% reduction of the estimated rate of water flux across the BBI was detected in the absence of these water channels. No significant changes were recorded in other, more established, quantitative MRI parameters: arterial transit time (δ_a), cerebral blood flow (CBF) and apparent diffusion coefficient (ADC) with the lack of AQP4 water channels. This highlights the sensitivity of the multi-TE ASL approach in the non-invasive assessment of AQP4 mediated water permeability in the brain. The emerging roles that AQP4 plays in brain clearance pathways point to AQP4 as a novel imaging target for neurological conditions such as AD.

The current study represents the first demonstration of a non-invasive technique able to detect differences in rates of water flux across the BBI due to the differential expression of AQP4. An overview of the literature suggests that prominent phenotypes associated with the AQP4-model mainly emerge in pathological conditions, such as induced meningitis or ischemic stroke [31, 33, 37, 38]. A 9-fold decrease in brain water uptake was observed in *Aqp4*$^{-/-}$ mice, following serum blood dilation by intraperitoneal injection measured ex-vivo by the change in brain water content, as an index of BBI water permeability [38]. The changes observed here were not as pronounced. However, the present recordings were done non-invasively, without subjecting the animals to pathophysiological conditions.

While *Apq4*$^{-/-}$ mice appear to have a subtle phenotype, they show a slight increase in brain water content [36], which may account for the increase in $T2_{EV}$ in the cortical brain region of this animal group. Further, *Aqp4*$^{-/-}$ animals have an intact endothelium as shown by histology [140], and confirmed by the absence of leakage of Evans Blue dye into the brain parenchyma [36]. This highlights the sensitivity of the multi-TE ASL technique in the ability to detect differences in BBI water flux without disruption to the integrity of the endothelial wall. It has been reported that small interference RNA (siRNA) can be used to transiently knock down AQP4 expression in the rat brain which caused a significant decrease in the measured ADC [141]. Interestingly, in the present study we recorded no significant differences in the ADC of the tissue in the *Aqp4*$^{-/-}$ mouse. This difference may reflect the acute nature of AQP4 modulation using siRNA, compared to the chronic AQP4-deficient model examined here. Overall, the specific contribution and possible compensation of other water transport mechanisms on water mobility are not fully understood.

Water traverses several different interfaces within the brain: across the blood-brain barrier and the astrocyte foot processes into extravascular brain tissue, through ependymal layer to access the ventricular space from the interstitial space and via the subpial astrocyte processes and pial cells into the subarachnoid space. All three routes are thought to be important for maintaining the water homeostasis of the brain and AQP4 is highly expressed in each of these interfaces [53]. AQP4 channels are believed to be a key component of the glymphatic clearance pathway, a waste solute removal system dependent on glial water transport [142]. It has been shown that glymphatic function was impaired by ~70% in *Aqp4*$^{-/-}$ mice compared to the WT animals, as detected by movement of a fluorescent tracer [45]. In this study we demonstrate sensitivity of multi-TE ASL to AQP4 expression, which plays a critical role in the glymphatic pathway. As such, this technique may represent a surrogate marker of glymphatic function. Further understanding the contributions of the rate of water flux across different membrane interfaces could help to detect putative malfunctions of these pathways in disease conditions.

Currently, the underlying mechanisms that determine changes to BBI permeability to water remain poorly understood. Diffusion-weighted ASL techniques (DW-ASL) have been used to assess BBI water permeability in various neurological conditions such as stroke [129], sleep apnea [143] and brain tumours [96, 144]. An increase in BBI water permeability via water exchange rate (K_w), was shown in a rat model of ischemic stroke, where changes in blood water permeability covered more extensive regions compared to the changes in BBI permeability determined by Evans Blue [129], demonstrating that water may be a more sensitive marker for BBI permeability than larger exogenous tracers. A further study reported a significant reduction of K_w in patients with obstructive sleep apnea (OSA) [145]. In this study the authors speculated that the measured reduction in water exchange rate reflects an increase in BBI permeability to water, however it is possible that compromised aquaporin function associated with this condition caused the measured reduction in the permeability-surface area product to water (PS_w). This highlights the need to better understand the role of AQP4 in water flux across the BBI, measured using translational non-invasive imaging techniques, which is the aim of the current work.

Multi-TE ASL is attractive because it offers a non-invasive approach to assess BBI water permeability. Conventionally, BBI permeability dysfunction is measured using dynamic contrast enhanced (DCE) MRI which requires contrast agents such as gadolinium. DCE-MRI detects gross BBI defects when a marked breakdown of endothelial tight junctions permits large contrast agent molecules to egress into the brain parenchyma. Detecting changes in BBI permeability to water may identify distinct pathological processes at the BBI (e.g. loss of AQP4 polarisation) that may occur at earlier stages of neurodegenerative disease progression prior to the opening of the endothelial layer. Multi-TE ASL and DW-ASL eliminates the need to inject MRI tracers for permeability measures, and though these agents are used routinely in the clinical setting, there is increasing speculation about the potential harm that repeated doses may cause to patients in the long term [91]. Therefore, there may be further clinical benefits to non-invasive measures of BBI permeability.

Adapted ASL methods that use alternate contrast mechanisms to assess BBI permeability to water have also been proposed in various studies [94, 107, 128, 146]. DW-ASL techniques may be complicated by the directional dependence of the signal attenuation, which is dependent on the chosen inflow time [110]. A recent study estimated the water extraction fraction (E) by measuring the proportion of labelled spins draining to large cerebral veins for BBI water permeability determination [105]. This approach provides limited spatial specificity and may restrict the regions where BBI permeability can be assessed, because of the necessity to extract the signal from the large draining veins. Visual inspection of **Figure 3.2A** indicates spatial heterogeneity of the exchange time within the coronal slice studied in this work. The present study was designed to measure water exchange time in the cortical region and the modulation of this parameter by AQP4 expression. Future studies, however, may wish to further probe the regional distribution of water exchange time, possibly by incorporating a multi-slice approach to image acquisition. Further experiments would be necessary to further explore how other factors such as distribution of tight junction proteins, pericyte coverage or extent of AQP4 polarisation impact the water flux across the BBI.

There is increasing evidence to suggest that AQP4 water channels plays an important role in brain Aβ clearance [45, 113]. The loss of perivascular localization of AQP4 is proposed to be a factor that is associated with an increased Aβ burden [51, 112]. Studies show a correlation between AQP4 polarisation with the severity of AD in the human brain [51].The data suggests that the multi-TE ASL technique applied here is sensitive to the perivascular expression of AQP4, given that the technique is specifically targeting water exchange at the BBI. Future studies applying multi-TE ASL to other genetic mouse models could more specifically address the effect of specific AQP4 pools on the transfer of water across the BBI**.**

3.5 Conclusion

In conclusion, the multi-TE ASL technique developed for the mouse brain to able to assess AQP4-mediated water transport at the BBI. Previous studies suggest that the capacity of this water transport system is a key determinant of Aβ clearance from the brain. Further studies will be implemented to better understand the precise role of AQP4 polarisation on BBI water permeability. Overall, the emerging importance of AQP4-mediated clearance pathways, such as the glymphatic system, make this technique a promising and clinically applicable tool for better understanding the role of AQP4-mediated clearance in pathological conditions like AD.

Chapter 4

Development of Multiple Echo Time Arterial Spin Labelling Technique in 9.4T Bruker System

For assessment of regional variation of blood-brain interface permeability to water

9.4T Bruker Scanner,
Centre for Advanced Biomedical Imaging

Aim

We recently had a new 9.4T Bruker Biospec scanner installed in the laboratory, which gave the opportunity to translate the imaging protocols from the 9.4T Agilent scanner that is now over 10 years old. This installation provided the opportunity to potentially improve the multi-TE ASL technique taking advantage of the enhanced features of the MRI hardware and software and compare the results between the two different imaging systems. Improvements to the multi-TE ASL technique would potentially enable regional variation of blood-brain interface (BBI) permeability to water measurements across the mouse brain to be evaluated, working towards brain-wide application of the technique.

Firstly, a multi-TE ASL imaging protocol was developed and optimised on the new 9.4T Bruker system. These data were then compared to the previous ASL data acquired on the Agilent system in order to examine the consistency of the cortical exchange time measurements in the mouse brain across the two imaging systems. Secondly, the optimised multi-TE ASL technique (Bruker) was implemented in a pilot study, to investigate the following hypothesis: BBI water permeability is higher in the cerebellum than the cortical brain region, due to higher expression of aquaporin-4 (AQP4) water channels in the cerebellum.

This work was presented as a power pitch and poster at the annual meeting of ISMRM 19, Montreal, Canada.

4.1 Introduction

Whole brain MRI can capture the signature patterns of regional pathology that define different neurodegenerative conditions, such as frontotemporal dementia and Alzheimer’s disease. However, to date, there has been very limited evaluation of regional variation in water permeability in healthy and pathological brain tissue using non-contrast MRI techniques.

Multi-TE ASL MRI has been previously applied to assess blood-brain interface (BBI) water permeability in the cortex of the mouse and rat brain [109, 147]. However, thus far, the technique has been limited to single cortical brain regions only, partly due to the proximal distance to the surface coil and the relatively large size and homogeneity of the cortex as well as the single slice image acquisition employed. By developing the technique on an MRI system with more advanced hardware and software, methodological improvements are achievable that, in turn, may enable the assessment of BBI permeability across multiple brain regions. Therefore, the implementation of a multi-TE ASL imaging protocol on a 9.4T Bruker imaging system may extend the scope of the technique to probe other brain regions, working towards brain-wide application.

Though it is currently challenging to acquire a 'gold-standard' measurement for the exchange time parameter as an index of BBI permeability to water, the experiments performed in **Chapter 2 & 3** provide evidence to support the capability of the multi-TE ASL technique to capture the labelled vascular water moving into the extravascular tissue. Reproducing these results on another imaging system would provide further confidence in the physiological relevance of the technique. Hence, the exchange time (T_{ex}^{w}) and intravascular and extravascular T2 relaxation time ($T2_{IV}$ / $T2_{EV}$), will be measured with a new imaging protocol on the Bruker scanner to be compared with the previous data acquired on the Agilent scanner. Measurements of the stability in the resultant images across the given repetitions are taken in order to assess and compare the experimental and physiological noise from each of the imaging protocols.

The 9.4T Bruker imaging system has several enhanced features that could benefit the implementation of the multi-TE ASL technique for the assessment of BBI permeability. The Bruker gradient set (BioSpec B-GA 12S2) has a 10% higher gradient amplitude (440 mT/m) compared to the 9.4T Agilent system (400 mT/m) which can improve the imaging speed. With matching EPI imaging sequence parameters, the excitation pulse length and refocussing pulse length is found to be shorter on the Bruker system (1.91 ms and 1.55 ms respectively) compared to on the Agilent system (2.04 ms and 2.08 ms respectively) which would have an impact on the minimum echo time achievable for the acquisition. Again, with matching imaging parameters, the ramp time for the echo planar imaging (EPI) readout is also markedly shorter on the Bruker (50 µs) compared to the Agilent system (120 µs) which could further reduce the minimum echo time and reduce susceptibility of the sequence to motion. The EPI inter-echo spacing is less, which will reduce distortions in the phase-encoding direction making a single shot acquisition more feasible. Moreover, the Bruker volume coil can be coupled with a four-channel mouse brain surface coil for transmission and reception of the signal respectively. The increased number of channels (compared to the Agilent system which had a two-channel surface coil) will improve the SNR, as well as possibly being able to probe deeper brain regions due to the circularly polarized shaped design that has optimal sensitivity for the mouse head.

A current limitation of the imaging protocol on the Agilent system is that, for the chosen spatial resolution (FOV and matrix size), the shortest reliable echo time (TE) is 15ms using a two-shot segmented readout. Considering the intravascular transverse relaxation ($T2_{IV}$) is ~15-20 ms [116, 147], approximately half of the signal derived from this compartment would have decayed by the first TE. Therefore, moving to a shorter minimum echo time may be beneficial to improve the precision of $T2_{IV}$, which is currently the parameter with the largest variability, despite the technique optimisation and analysis development undertaken in the previous chapters. The in-built flow alternating inversion recovery echo planar imaging (FAIR_EPI) sequence on Bruker Paravision 6.0 software provides a shorter minimum echo time (7.47 ms) at comparable spatial resolution to that employed on the Agilent system (**Chapter 2**), which, theoretically, should be able to better capture $T2_{IV}$ to improve the quality of the two-compartment bi-exponential fit. The built-in Bruker imaging sequences have been designed to produce robust single-shot EPI readout that are able to achieve shorter echo times, which will half the imaging scan time compared to a two-shot segmented readout and make the images less susceptible to motion artefacts. Improved scanner hardware may allow for higher resolution for the images, which will be beneficial to probe other, particularly smaller, brain regions. Therefore, a comparison study will be useful to assess the similarities/ differences in the variance of the resulting ASL images, to inform future studies with the possibility of targeting other brain regions in addition to the cortical region.

The blood-brain interface (BBI) regulates the passage of the vital molecules that pass from the vasculature into the brain parenchyma. It is thought to be heterogeneous across the brain, partially due to the variation in the density of pericytes and different types of astrocytes within different regions [148]. However, there are limited studies about BBI permeability differences in specific brain regions in normal physiological conditions using non-invasive methods [21, 148]. More specifically, to my knowledge there are only two studies that have measured water permeability across the BBI in different brain regions [90, 104]. Early BBI permeability to water studies have reported mean grey matter/ white matter measurements across the brain [96, 116, 143], and other water permeability techniques make a global measurements using the venous signal contribution [105, 149]. Therefore, it would be useful to extend the multi-TE ASL technique to assess different regions of the mouse brain to determine potential spatial alterations in the BBI integrity.

Brain aquaporin-4 (AQP4) water channels are central to the transfer of water across the BBI, and the previous chapter demonstrates the sensitivity of the multi-TE ASL technique to changes in AQP4 channels at the BBI [147]. Differences in the AQP4 distribution across regions and sub-regions of the brain, as well on a cellular level, would suggest that the capacity of AQP4 mediated water transfer to be regionally heterogeneous [150]. It has been shown that there are marked regional differences in AQP4 expression within the healthy mouse brain [151]. Therefore, to investigate the possible application of multi-TE ASL in different brain regions, the multi-TE ASL technique will be applied to the cerebellum in a pilot study to compare BBI permeability to water in the cortical and cerebellar brain regions. My hypothesis is that the cerebellum may have an increased capacity to exchange water across the BBI compared to the cortex, given the markedly higher expression of AQP4 within this region [150]. Measuring regional differences in water transport across the healthy mouse brain may represent a novel approach for characterising changes in BBI water permeability associated with different neurodegenerative conditions.

4.2 Methods

The multi-TE ASL technique was implemented on the 9.4T Bruker imaging system. Firstly, ASL data acquired using an optimised sequence on the Bruker system was compared with the ASL data previously obtained from the 9.4T Agilent system, to assess the similarity of the technique on another imaging system. Secondly, a pilot study was performed to assess the capability of the 9.4T Bruker system to measure BBI permeability in the cerebellar brain region to determine any measurable differences to the cortex and to assess the scope of expanding the technique to brain-wide application.

4.2.1 Comparison Study: Multi-TE ASL Imaging Protocols

All experiments were performed in mice in accordance with the European Commission Directive 86/609/EEC (European Convention for the Protection of Vertebrate Animals used for Experimental and Other Scientific Purposes) and the United Kingdom Home Office (Scientific Procedures) Act (1986). All mice were acclimatised prior to data acquisition in an animal house maintained on a 12 h light/12 h dark cycle with food and water provided *ad libitum*.

4.2.1.1 9.4T Agilent Imaging Protocol

The data used here was taken from the implementation of the multi-TE ASL technique presented in **Chapter 2: Methods, Multi-TE Acquisition for Technique Validation**, with images acquired in the 9.4T VNMRS horizontal bore MRI scanner (Agilent Inc.) with an Agilent 205/120HD gradient set, a 72 mm inner diameter volume coil and a two-channel array surface coil (Rapid Biomedical).

Briefly, ASL data was acquired using the Agilent system in female C57/Bl6 mice at 4 ± 1 months old (n = 5). The multi-TE ASL sequence was based on a flow-alternating inversion recovery (FAIR) sequence with a two-shot segmented spin-echo (SE) echo-planar imaging (EPI) readout. Imaging sequence parameters were inflow time (TI) = 1500 ms; echo time (TE) = 15 ms, 18 ms, 23 ms, 30 ms, 40 ms, 50 ms, 65ms; repetition time (TR) = 5000 ms; data matrix = 32 x 32, field-of-view (FOV) = 25 x 25 mm; repetitions = 20; scan duration: ~35 minutes.

4.2.1.2 9.4T Bruker Imaging Protocol

Images were acquired in C57/Bl6 mice at 4 ± 1 months old (n = 5). All mice were induced with 2% isoflurane anaesthetic in a mixture with room air at 1.0L/min. The mice were administered a subcutaneous saline injection of 0.25ml saline solution to avoid dehydration over the scan duration. Mice were placed in the MRI cradle with the front incisor in the bite bar and ear bars with a nose cone were used to secure the head in position and to minimise motion. Eye gel was applied to the mice eyes to avoid damage to the eyes while the animal was in the scanner. A rectal probe (SA Instruments) was used to monitor the core body temperature which was maintained at 37.0 ± 0.5°C via an adjustable water bath supplied to a mouse heating pad (Bruker BioSpec). The anaesthesia was adjusted between 1.75-1.5% to maintain the respiration at ~100bpm, which was measured using a pressure pad and monitored throughout the scan.

Images were acquired on a 9.4T Bruker imaging system (BioSpec 94/20 USR) with a horizontal bore and 440 mT/m gradient set with outer/ inner diameter 205 mm /116 mm respectively (BioSpec B-GA 12S2), 86mm volume coil and a four-channel array mouse brain surface coil for the transmission and the reception of the radiofrequency (RF) signal respectively. The imaging sequence is based on a flow-alternating inversion recovery (FAIR) with a spin-echo (SE) echo planar imaging (EPI) readout, from the *Perfusion_FAIR_EPI* imaging sequence using Paravision 6.0.1 (Bruker software). The position of the mouse brain was placed symmetrically in the iso-centre to maximise the quality of the shim.

The *Perfusion_FAIR_EPI* sequence is a single echo time FAIR acquisition, the protocol was extended to acquire ASL data at multiple echo times. This was implemented by initially acquiring a B_0 map for the automated shim able to minimise the magnetic field inhomogeneities. The field inhomogeneities were further improved by manually performing 1st order and 2nd order shims to minimise the distortions associated with the boundaries between different types of medium, this effect can manifest as the shape of the brain being distorted. This calibration was applied across all the imaging sequence parameters (below).

The imaging parameters implemented on the 9.4T Bruker system had several improvements compared to the sequence parameters used in the imaging protocol on the Agilent system. Echo times (TE) = 8 ms, 10 ms, 12 ms, 15 ms, 18 ms, 23 ms, 30 ms, 40 ms, 50 ms, 65ms (the shorter minimum echo time was used to better capture the fast-decaying IV compartment of the ASL signal). Inflow time (TI) = 1500 ms and repetition time (TR) = 5000ms for direct comparison with the previous ASL data from the Agilent system. A single shot EPI readout was used to reduce the overall scan time (and reduce susceptibility to motion artefacts). Though single shot

EPI readouts can more susceptible to geometric distortion relative to multiple-shot segmented readouts, reducing the scan time would benefit further experiments where multiple inflow times or multiple imaging slice locations are implemented in the same animals, in addition to reducing possible physiological variability that could occur when scanning an anaesthetised mouse for long periods. A partial fourier readout was used to decrease the EPI train length in order to further reduce the time of the minimum echo time; partial fourier = 32 + 4 lines of k-space. A single dummy scan was included before the image acquisition at each echo time for the magnetisation of the tissue to reach steady state before the image readout.

Further imaging sequence parameters for the multi-TE ASL technique were an increased resolution to better target different (smaller) brain regions: data matrix = 64 x 64; field-of-view (FOV) = 25 mm x 25 mm; slice thickness = 2 mm. Repetitions = 5; averages = 2 (the averages were repetitions that were automatically combined on the imaging software, this was to minimise any software delays when moving between the scans with different TEs). Saturation bands were included around the brain region, and fat suppression was enabled to minimise the related artefacts [118]. Scan duration: ~20 minutes.

4.2.2 Pilot Study: Regional Variation of BBI permeability to water

The optimised imaging protocol for the 9.4T Bruker imaging system was then applied in a separate set of experiments to assess BBI permeability to water for both the cortical and the cerebellum brain region in each scan session. ASL data were acquired in five female C57/Bl6 at 4 ± 1 months old at two inflow times: TI = 800ms and 1500ms. Given my hypothesis that the BBI water permeability would be higher in the cerebellar brain region, the additional shorter inflow time (800ms) was included to capture the intravascular signal before it transfers into the extravascular (EV) compartment (i.e. it may be such that, in the cerebellum, at TI = 1500ms the ASL signal is derived solely from the EV compartment due to the fast exchange time which would make the exchange time calculations impossible).

The other imaging parameters were: TE = 8 ms, 10 ms, 12 ms, 15 ms, 18 ms, 23 ms, 30 ms, 40 ms, 50 ms, 65 ms; TR = 5000 ms; data matrix = 64 x 64; FOV = 25 x 25 mm; slice thickness = 2 mm; partial fourier = 32 + 4 lines of k-space; repetitions = 10. The position of the coronal slice was moved between the middle of the mouse brain (caudal cortex) and the back of the brain (cerebellum). The order of the inflow time and the slice positions were randomised across the animals to eliminate any bias that might arise from physiological changes that occur after prolonged anaesthesia. A manual shim centred on each imaging slice was performed before the acquisition of data of each slice to ensure the optimal image quality.

4.2.1.1 Quantification of Aquaporin-4 mRNA Expression

A protocol was established to quantify the expression profile of *Aqp4* within the mouse brain to better understand how possible difference in the non-invasive measurements of BBI permeability to water might be related to the molecular composition of the brain region. The protocol for the biochemical techniques were optimised by an M.Sc. student in the laboratory. I established and applied this protocol in this pilot study to assess the AQP4 mRNA expression with the cortical and cerebellum brain regions. These methods could then be incorporated and built upon in the study design of future experiments, described in the following chapters.

Aqp4 mRNA expression was quantified in the caudal cortex and the cerebellum regions of a cohort of female C57/ Bl6 mice at 4 ± 1 months old (n = 6, separate mouse cohort). All mice were euthanised by overdose with intra-peritoneal injection of sodium pentobarbital (10 ml/kg), the brain was removed, hemisected, and the caudal cortex and the cerebellum dissected and snap frozen in isopentane pre-chilled on dry ice.

Total RNA was extracted and converted in cDNA using RNeasy Plus Microkit and QuantiTect Reverse Transcription kit (Qiagen, UK). Genomic DNA was eliminated by incubation of RNA with 2 µl of gDNA wipeout buffer at 42°C for 2 minutes. The samples were then incubated at 42°C for 15 minutes in a reverse-transcription master mix of 1 µl Quantiscript Reverse Transcriptase (RT), 4 µl Quantiscript RT buffer, 1 µl RT Primer mix to convert from the extracted RNA to cDNA. The RT was inactivated by an incubation of the samples for 3 minutes at 95°C. Finally, 80µl of nuclease-free water was added to dilute the cDNA samples and were stored at -20°C until qRT-PCR analysis.

20 µl samples consisting of 2 µl cDNA, 1 µl primer (*Aqp4* or reference housekeeper genes, β-Actin and *GAPDH (*Taqman)), 10 µl of Master Mix (TaqMan) and 7 µl of nuclease-free water were pipetted in 96-well plate. Triplicates of each of the genes were made for each sample, to ensure concordant results and eliminate any anomalies. The quantitative reverse transcription PCR (qRT-PCR) protocol was programmed at 55°C for 2 mins, 95°C for 10 mins followed by a 2-step cycle of 95°C for 15 s and 60°C for 60 s which repeated over 50 cycles, using the Eppendorf Mastercycle with RealPlex software (v1.5, Eppendorf, UK). This RT-qPCR protocol generated sigmoidal curves from the whose Ct values were extracted with the threshold value set to 1000 units. The quantification of the final *Aqp4* gene expression levels was calculated by the $2^{-\Delta\Delta Ct}$ method [138], taking the cortical region as the control group of unit reference value, with its normalisation factor was calculated based on the geometric mean between the two housekeeper genes, and the *Aqp4* mRNA expression of cerebellum was expressed as a fold-change of the unit reference.

4.2.3 Data Analysis

All imaging data was analysed using Matlab 2018a (Mathworks) and GraphPad Prism 8 (GraphPad software). Automatic signal intensity scaling of each of the ASL image pairs (for each TE) occurs when acquiring the individual images in the 9.4T Bruker system using the Paravision 6.01 software. Therefore, the image signal intensity for each data set was adjusted in post-processing for the correct scaling effects. The reconstruction parameters follow the model:

$$M = M_c . recon_{slope} + recon_{offset}$$

where M is normalised signal, M_C is the original signal, recon_slope is the scaling factor and recon_offset is the reconstruction offset. The baseline signal (M_c) is essential for correct evaluation of the multi-TE decay.

Mean ASL images were generated and an analysis pipeline was established **(Figure 4.1)**. Each brain region (either cortical or cerebellar) was manually defined and the signal from the control data was extracted and fit to a mono-exponential decay model to measure the extravascular tissue $T2_{EV}$. The mean group $T2_{EV}$, was calculated and fixed for the two-compartment bi-exponential fit. The ASL signal was extracted from the same region and a group-wise bi-exponential fit was performed to generate individual intravascular (IV) and extravascular (EV) ASL signal intensities, ΔM_{IV} and ΔM_{EV} respectively, and a single common $T2_{IV}$. ΔM_{IV} and ΔM_{EV} variable were constrained to be greater than zero so that the model was physiologically relevant. Outliers, in the groupwise fitting, were determined using ROUT coefficient (Q set at 1%) [152], and were excluded from further analysis.

The ASL signal contributions were used to calculate the intravascular fraction $\left(\frac{\Delta M_{IV}}{\Delta M_{IV} + \Delta M_{EV}}\right)$. The intravascular fraction was taken together with the average arterial transit times, 125ms for the cortex and 90ms for the cerebellum (values taken from other experimental data in the following **Chapter 6**), to measure the tissue transit time, using the two-compartment kinetic perfusion model. The average arterial transit time values were taken for the data analysis of this study because the calculation of individual arterial transit time values were not possible due to technical inaccuracies during the data acquisition. Finally, the exchange time (T_{ex}^{w}) was measured by subtracting the tissue transit time from the average arterial transit time, and averaged for the two inflow times to give a surrogate index of BBI permeability to water.

Intravascular maps were generated by manually segmenting the whole brain region from the imaging slice. A pixel-wise $T2_{EV}$ map was generated for each animal, and was used, along with the fixed shared $T2_{IV}$ for each brain region, in the pixel-wise bi-exponential fitting of the ASL images across all of the echo times. The individual intravascular fraction maps were for visualisation purposes.

Cerebral blood flow (CBF) was assessed by taking the ASL signal at a short echo time, ΔM, for the two inflow times and applying them to the Buxton model:

$$\Delta M = 2.M_0.(TI-\delta_a).\alpha.CBF.\left[\frac{\max(0,TI-\delta_a}{TI-\delta_a}\right]\left(\exp\left(-\frac{TI}{T1_b}\right).q_1.\frac{\min(0,TI-\delta_a-\tau)}{TI-\delta_a-\tau}\right.$$
$$\left. +\ 2.M_0\tau\alpha.\exp\left(-\frac{TI}{T1_b}\right).q_2\,\frac{\max(0,TI-\delta_a-\tau)}{TI-\delta_a-\tau}\right).$$

where M_0 is the equilibrium magnetisation from the short echo time control signal using the standard recovery model [118], TI is the inflow time, δ_a is the arterial transit time, α is the inversion efficiency (0.9), $T1_b$ is the longitudinal relaxation of the arterial blood (2.5s [124]), τ is the temporal length of the labelled bolus (2.0s taken from previous experiments [120]).

$$k = \frac{1}{T1_b} - \frac{1}{T1 + {}^{CBF}/_{\lambda}}$$

$$q_1 = \exp(k.TI).\exp(-k.\delta_a) - \frac{\exp(-k.TI)}{k.(TI-\delta_a)}$$

$$q_2 = \exp(k.TI).\exp(-k.\delta_a) - \frac{\exp(-k.(\tau+\delta_a)}{k.\tau}$$

where λ is the partition coefficient (0.9 [123]).

The stability in the measured ASL signal was assessed by calculating the mean values of μ/σ (mean signal intensity/ standard deviation from all of the echo times) across the repetitions for data acquired on the Bruker and the Agilent system respectively.

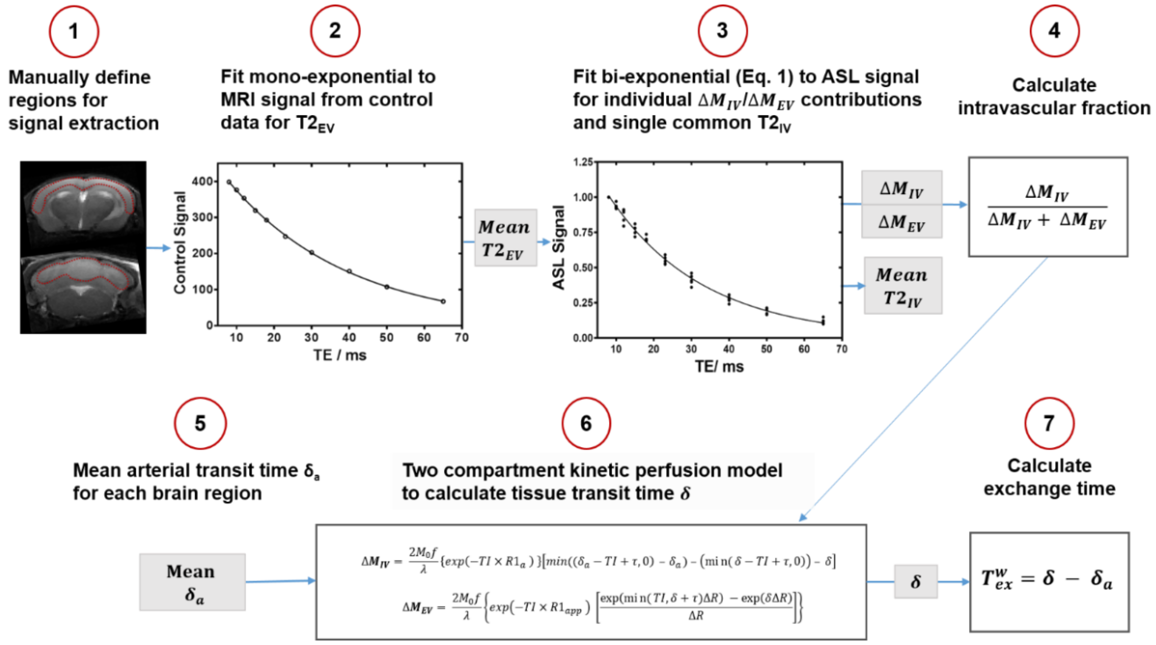

Figure 4.1: Analysis Pipeline for Exchange Time (T_{ex}^{w}) measurements. Step-wise approach for calculating the intravascular fraction and the exchange time from the ASL data.

4.3.1 Statistical Analysis

All data are reported as the mean and associated error (± std), with statistical analysis performed using GraphPad Prism 8 (GraphPad Software). An unpaired student's t-test was used to compare the $T2_{EV}$ and the intravascular fraction parameters in the comparison study between the two imaging systems. A 2-way ANOVA with a Bonferroni's multiple comparison test was used to compare the variation in intravascular fraction for i) the inflow times and ii) brain regions. A paired two-tailed student's t-test was performed to assess differences between the mean exchange times in the cortical and the cerebellar brain regions as a dependence on inflow time was not expected. A paired two-tailed student's t-test was performed to assess the difference in the CBF and *Aqp4* mRNA expression. For all tests, $p < 0.05$ was considered to be a statistically significant result.

4.3 Results

4.3.1 Comparison Study: 9.4T Imaging Systems

The multi-TE ASL technique, with the newly designed imaging protocol, was successfully implemented on the 9.4T Bruker system, **Figure 4.2** is a representative example of the quality of the ASL images, taken at increasing echo time, from this imaging protocol. The ASL signal extracted from the cortical brain region is well described by the bi-exponential model across both of the imaging systems, **Figure 4.3A**. Despite the difference in the imaging protocol between the two imaging systems, the behaviour of the decay of the plots are broadly similar and the between-animal variability is minimal.

There is a clear similarity between all of the parameters extracted from the bi-exponential fit to the multi-TE ASL data acquired from both of the imaging systems, which highlights the reproducibility of the technique across the two imaging systems, Table 1. The mean extravascular tissue $T2_{EV}$ is comparable using both of the imaging protocols, this has the smallest error of all of the parameters which is expected since the measurement is taken from the high SNR control signal. The mean intravascular $T2_{IV}$ is lower in the Bruker imaging acquisition (13.8 ± 4.0 ms) compared to the Agilent (18.4 ± 4.8 ms), which may be due the larger range of echo times (specifically the additional shorter TEs) in Bruker imaging protocol. For the intravascular fraction estimates, the results are very similar at 0.33 ± 0.07 with the Agilent protocol compared to 0.31 ± 0.06 the Bruker imaging protocol, **Figure 4.3B**. Assuming that the mean arterial transit time is 150 ms, the mean cortical exchange time is 396 ± 82 ms on the Bruker system which is consistent with the previous measurements using the Agilent imaging protocol (395 ± 54 ms) [147].

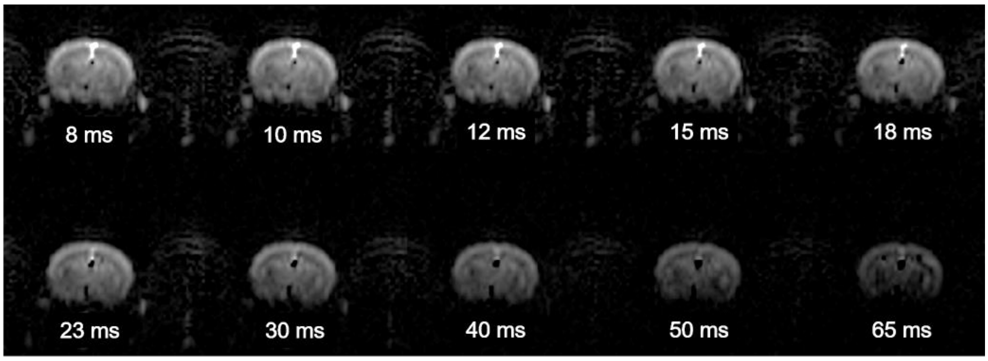

Figure 4.2: Example of ASL images acquired a representative animal using the 9.4T Bruker at increasing echo time (indicated on images) with the optimised imaging parameters.

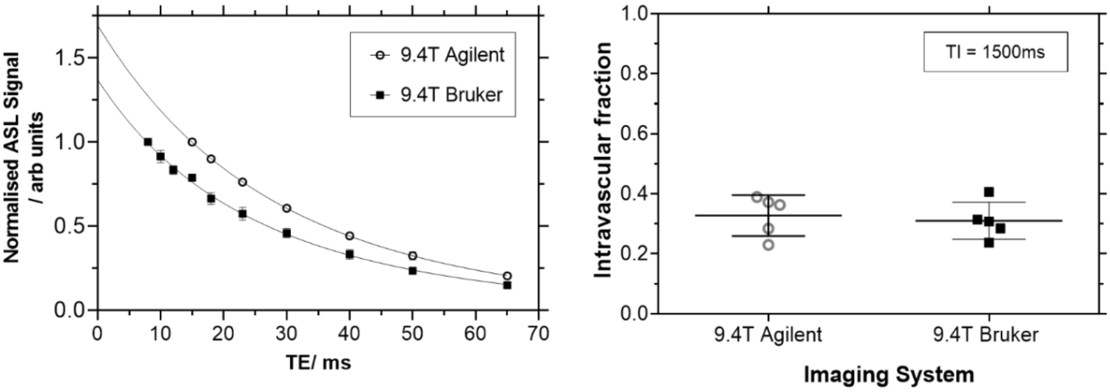

Figure 4.3: ASL signal decay from the two 9.4T imaging systems. A. Mean ASL signal fitted to bi-exponential model for the optimised 9.4T Agilent system imaging protocol (n = 5) and the 9.4T Bruker system imaging protocol (n = 5). **B.** Intravascular fraction for individual animals at inflow time (TI) = 1500 ms. The mean value and the associated error (± std) are displayed on both plots. NB. In some cases the error bars may not be visible they are very small.

	9.4T Agilent System	**9.4T Bruker System**	**Comparison Statistics**
$T2_{IV}$	18.4 ± 4.8ms	13.8 ± 4.0ms	-
$T2_{EV}$	36.2 ± 1.2ms	35.7 ± 0.8ms	0.49
IV Fraction	0.33 ± 0.07	0.31 ± 0.06	0.68

Table 4.1: Parameters associated with the ASL signal decay for the 9.4T Agilent imaging protocol and the 9.4T Bruker and the associated comparison statistics.

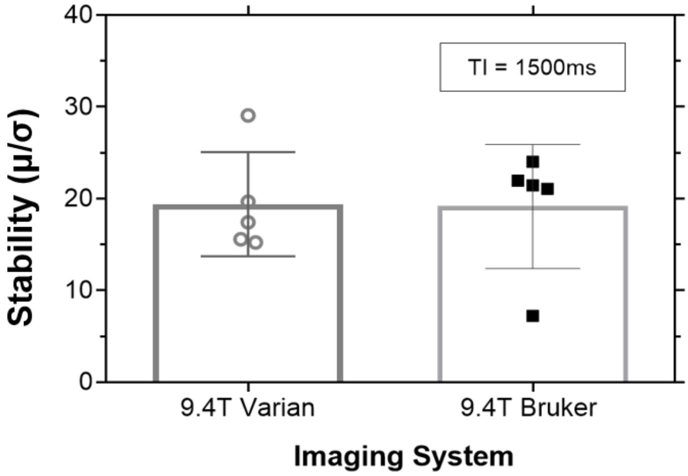

Figure 4.4: Stability of the ASL signal decay. The mean/ standard deviation (μ/σ) of the ASL signal across the repetitions for the individual animals with the mean and the associated error displayed for both of the imaging systems.

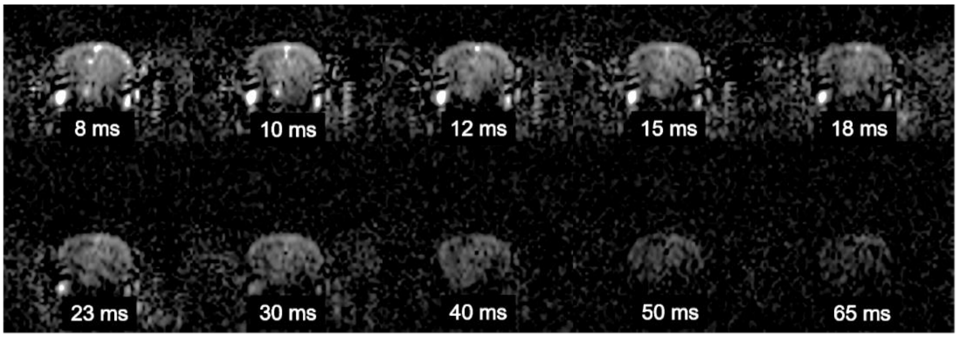

Figure 4.5: Example of poor quality ASL images. This is an example of ASL data containing artefacts with a low stability (μ/σ).

The mean stability (μ/σ) of the ASL signal was measured for the individual animals for both of the imaging protocols to measure the stability of the ASL measurements. This measure of signal stability takes into account both experimental and physiological noise, and was measured at 19.4 ± 5.7 for the Agilent compared to 19.4 ± 6.6 on the Bruker system, **Figure 4.4**. The ASL data from the Bruker imaging protocol associated with the lowest stability had visible artefacts with the images which may have been due to motion or poor shimming, the resultant images are shown in **Figure 4.5**. The variability between the two imaging protocols are comparable, but the Bruker system is able to acquire data in a reduced scan time at a higher resolution.

4.3.2 Pilot Study: Regional variation of BBI permeability to water

The multi-TE ASL technique was applied to the cortical brain region and the cerebellum brain region to assess any difference in the BBI permeability to water in these brain regions. The ASL data was fit to the biexponential model in both the cortical region and cerebellum region at the two inflow times. The ASL signal has a slower decay when the inflow time is increased from 800ms to 1500ms in both brain regions, which is consistent which the previous trend presented in Chapter 2 ($p < 0.001$), **Figure 4.6.** This indicates that the multi-TE ASL technique implemented on the Bruker system is able to capture the labelled vascular water moving into the extravascular brain tissue in both cortical and cerebellar brain regions as TI is increased.

A significant reduction in the intravascular fraction in the cerebellar compared to the cortical brain regions was recorded at TI = 800ms: 0.657 ± 0.21 and 0.907 ± 0.08 respectively ($p = 0.013$), **Figure 4.7B**. A similar intravascular fraction between the two brain regions was measured at TI = 1500ms: 0.263 ± 0.20 and 0.266 ± 0.08, ($p > 0.99$), **Figure 4.7B**. Overall, the mean exchange time was higher in the cortical region (478 ± 61 ms) compared to the cerebellum region (313 ± 77 ms), though not significant ($p = 0.11$), **Figure 4.8A**.

CBF (averaged over both inflow times) was measured at 195 ± 35 ml/100g/min and 212 ± 65 ml/100g/min in the cortical and cerebellar region respectively**,** $p = 0.58$ **Figure 4.8B**. There was no measurable difference in the CBF between the cortical and cerebellar regions, suggesting similar cerebral energy demands and haemodynamic in two brain regions.

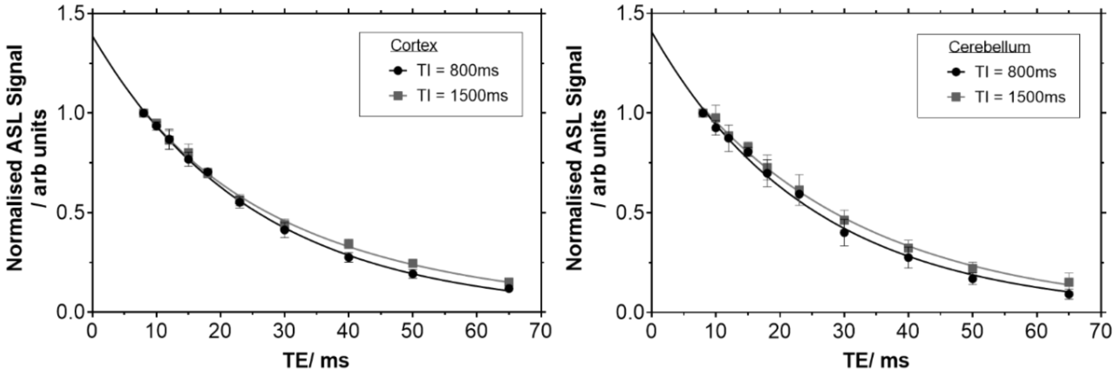

Figure 4.6: ASL signal decay for the cortical region and the cerebellar brain region at inflow times, TI = 800 ms and TI = 1500 ms, with the mean parameter and the associated error indicated in the plot with the mean values and the associated errors (± std) (n = 5).

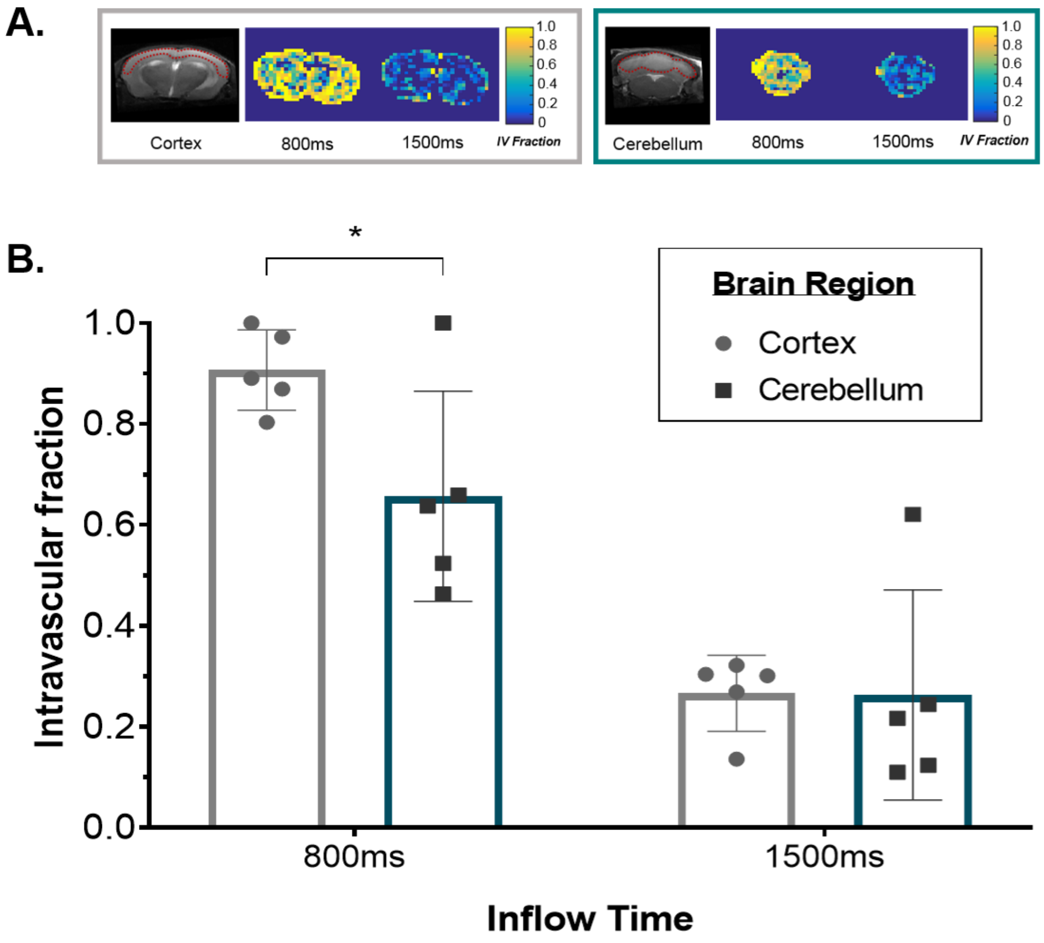

Figure 4.7: Multi-TE ASL in cortical and cerebellar brain regions. **A**. Intravascular fractions maps for cortical and cerebellar slice of the mouse brain with inflow times indicated for each image, and anatomical reference image with ROI in red. **B.** Intravascular fraction derived from the cortical and cerebellar brain regions for individual subjects at inflow times TI = 800 ms and 1500 ms. The mean parameter and associated error (± std) are displayed. * indicates $p < 0.05$.

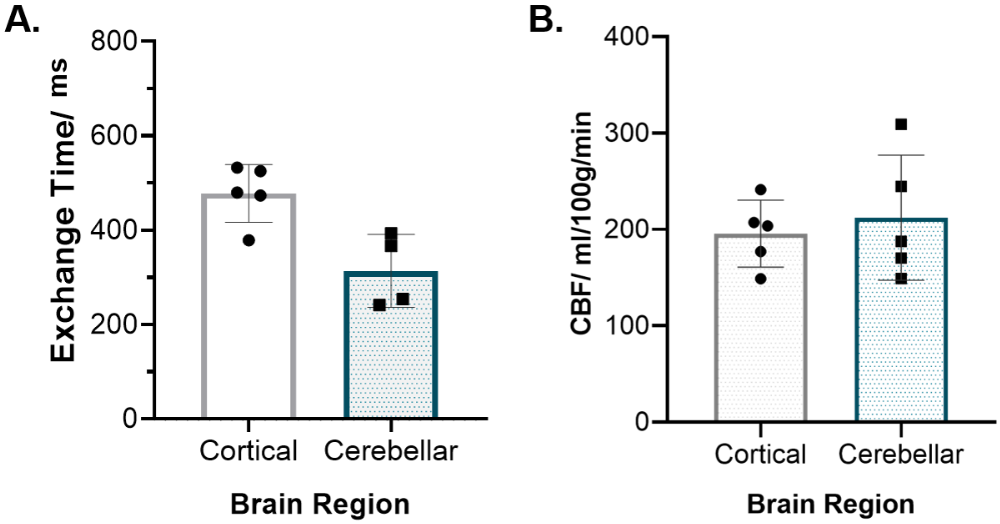

Figure 4.8: BBI Permeability to water and perfusion in cortical and cerebellar brain regions **A.** Exchange time measurements and **B.** Cerebral blood flow (CBF) measurements in the cortical and cerebellar regions for individual animals with the mean value and the associated error (± std) indicated on each of the plots.

The cortical intravascular $T2_{IV}$ was 24.2 ± 4.2 ms and 13.0 ± 3.5 ms at TI = 800 ms and TI = 1500 ms respectively. In comparison, the cerebellar $T2_{IV}$ was measured at 19.5 ± 1.8 ms and 18.7 ± 3.7 ms at TI = 800 ms and TI = 1500 ms respectively. The extravascular cortical tissue $T2_{EV}$ was measured at 37.0 ± 0.7 ms and 33.5 ± 0.8 ms for TI = 800 ms and TI = 1500 ms respectively. The cerebellum tissue $T2_{EV}$ was measured at 34.6 ± 2.4 ms and 31.8 ± 2.2 ms at TI = 800 ms and TI = 1500 ms respectively. The lower $T2_{EV}$ in the cerebellum is expected due to increased white matter tissue within this brain region. The differences in the $T2_{IV}$ and $T2_{EV}$, at the different inflow times, would indicate the relaxation of the spins from different molecular environment may be depend on the T1 relaxation and influence the T2 measurement derived from the control signal.

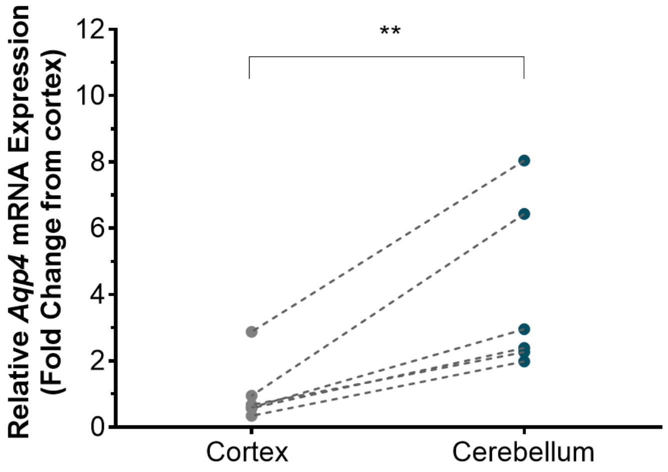

<u>Figure 4.9: *Aqp4* mRNA expression</u> from paired cortical and cerebellar brain regions of C57/Bl6 WT mice (n = 6). ** indicates $p < 0.01$.

The mRNA expression of *Aqp4* showed a 4-fold increase in the cerebellum region compared the cortical control region ($p = 0.01$), **Figure 4.9**. This would suggest that the expression of AQP4 water channels may have an effect on the BBI water permeability, however it seems that it is not a dominant mechanism as reflected by the non-significant difference in exchange time between the cortical and cerebellar brain regions.

4.4 Discussion

4.4.1 Comparison Study: 9.4T Imaging Systems

The multi-TE ASL technique has been implemented on the 9.4T Bruker imaging system with an imaging protocol that enables the acquisition of ASL images with larger range of echo times, in half the scan time and at higher resolution. Overall, the parameters derived from the ASL data from the cortical region using the Bruker acquisition, including the intravascular fraction, $T2_{IV}$ and $T2_{EV}$ and their associated errors, had distinct similarities with the previous measurements from the Agilent system, highlighting the reproducibility of the technique across imaging systems. Equivalence of the measured parameters derived from the two systems was hypothesized, but there was no certainty that the two systems would yield the same results given that the imaging protocols were not identical and there were several differences in hardware and software. Therefore, the comparable measurements provide further confidence in the measured exchange time as a meaningful index of BBI permeability to water.

The ASL TE-dependant signal decay from the imaging protocol of the Bruker system fits the bi-exponential model well. All of the parameters (ΔM_{IV}, ΔM_{EV}, $T2_{IV}$ and $T2_{EV}$) were measured with a slight increase precision using the Bruker system, Table 1. At TI = 1500ms the imaging protocol yielded an intravascular fraction of 0.31 ± 0.06 which is well within the margin of error of the previously measured intravascular fraction from the Agilent system, and overall yielded similar exchange time results on the Bruker system.

The intravascular $T2_{IV}$ parameter had a notable difference on the Bruker system compared to the Agilent system, though no statistics could be performed on this result due to it being a mean value for each group. It is likely that this difference is due to the minimum echo time being shorter in the Bruker imaging protocol, which better captures the fast-decaying signal which is thought to be derived from the vascular compartment. This is achieved on the Bruker system in part due to the shorter pulse length for the excitation and refocussing pulses and shorter ramp time for the EPI readout. Interestingly, although there is a decrease in the $T2_{IV}$ measured on the Bruker imaging protocol the intravascular fraction is measured to be the same as on the Agilent system. Hence, the change in intravascular $T2_{IV}$ does not seem to have a significant effect on the measured ratio between the IV and EV ASL signal weightings used to assess the BBI permeability to water. Further experiments must be performed to further understand the accuracy of the $T2_{IV}$ measurement and its precise physiological meaning.

The measure of stability of the ASL data is consistent between the two imaging protocols. Occasionally, the quality of the data can be significantly reduced because of increased motion, poor shimming or anatomical differences, such as mice having larger size air pockets in their ears which would have an effect on the shimming. An example of a poor image quality is shown in **Figure 4.5**, and is reflected in the lower stability point on the accompanying plot, **Figure 4.4**. Through visual inspection, these types of data sets with very poor quality images should be excluded from the group analysis in any future experiments. Overall, the stability of the Bruker data was in line with the previous Agilent data, using the new multiple echo time acquisition method. This demonstrates that the Bruker imaging protocol represents a promising development for using multi-TE ASL to target other regions across the brain, owing to the reduced acquisition time per imaging slice position.

The imaging protocol that has been implemented on the 9.4T Bruker system has yielded promising results for measuring the BBI water permeability in the cortical region of the mouse brain. The technical developments demonstrate that it would be beneficial to take advantage of the improvements and use it for subsequent experiments described in this thesis, beginning with the application to other brain regions to investigate regional differences in the BBI permeability to water.

4.4.2 Pilot Study: Regional variation of BBI permeability to water

The results from the pilot study show that though, there is a small decrease in cerebellar exchange time compared to the cortical region of the mouse brain this is not significant. The intravascular fraction suggests that labelled vascular water is transferred into the cerebellar brain tissue significantly faster than in the cortical region at TI = 800ms. However, this trend is not replicated at TI = 1500ms. The marked increase in expression of AQP4 water channels in the cerebellar brain region is not reflected here in the changes of in the BBI permeability of water in different regions of the mouse brain.

There are limited studies which have investigated the regional variation of BBI water permeability across the brain. This initial data suggests that the rate of water flux in the cerebellar region is slightly faster (though not significant) compared the cortical brain region. It is important to measure the physiologically ‘normal’ rates of vascular water flux across the different regions BBI, which remains scarcely explored, before moving to the changes that occur in pathology. There may be regions that become more vulnerable to particular pathologies, or, conversely, certain brain regions could provide a control region with stable BBI permeability to water. Therefore, this is a step towards extending the technique to a more brain wide application and other brain regions should be targeted in further experiments.

The slight increase in the BBI water permeability might be related to the marked increase in *Aqp4* expression (~400%) measured within the cerebellum relative to the cortex **Figure 4.9**. The previous results from **Chapter 3** show that water permeability across the BBI seems to be associated with the expression of AQP4 water channels, however this is an extreme model as the water channels are completely absent [147]. The 4-fold increase in the *Aqp4* mRNA expression is consistent with previous studies that have quantified AQP4 across the mouse brain using immunohistological techniques [151]. There may be several other mechanisms that contribute to the BBI water permeability [153], and future studies could be designed to assess the contribution of other factors, such as tight junction proteins or other molecular transporters, on the rate of vascular water transfer across the BBI of the healthy mouse brain.

The mean cortical CBF of WT mice was measured at 245 ± 89 ml/100g/min in the initial study implementing the multi-TE ASL technique on the mouse brain using the Agilent system, and analysing the CBF using the short inflow time data. Here the cortical CBF values are lower, but not significantly, at 195 ± 34 ml/100g/min ($p = 0.2776$). It is likely that this is due to cohort variability, but it may also highlight that there is some variation in the two methods for the CBF calculation which may be linked to the calculation of M0 (where a T1 of the tissue is assumed). Overall, this does not seem to have a large impact on the overall measurement. There are also no measurable differences in the CBF within the cerebellum brain region compared to the cortical region.

A significant decrease was measured in the intravascular fraction in both brain regions with increased inflow time, $p < 0.0001$. This would indicate that the imaging protocol established in the Bruker imaging system is able to capture the transfer of the labelled vascular water into the extravascular tissue as TI is increased. This replicates the results presented in **Chapter 2** in the methodological developments for the Agilent imaging system, and highlights the sensitivity of the method in the ability to detect the labelled vascular water transferring across the BBI.

The pilot data presented here indicates that the intravascular $T2_{IV}$ in the cerebellum region is lower compared to the cortical brain region. It is known that the T2 is highly dependent on the oxygenation of the vascular compartment [116, 154], therefore this decrease might be indicative of an increased oxygen extraction with the cerebellum region, which has been suggested in previous studies [155]. The difference in the $T2_{IV}$ in the two different brain regions may also suggest that the vascular architecture, as the cortex and the cerebellum are supplied by different feeding arteries, and the rate of oxygen extraction varies between the brain regions [156]. It highlights the benefit of measuring the $T2_{IV}$ and incorporating it in the two-compartment kinetic perfusion model. Further investigation into the $T2_{IV}$ parameter may reveal some novel blood oxygenation related information using this non-invasive technique.

When the inflow time is increased a substantial decrease in the $T2_{IV}$ was measured in both the cortical and the cerebellar brain regions. The increase in inflow time would allow more oxygen to be extracted at the capillaries which could effect the $T2_{IV}$ of signal derived from labelled vascular water in the intravascular compartment. The decreasing $T2_{IV}$ at increased inflow time may indicate that the technique is probing the labelled vascular water at a different point down the vascular tree. The effect could be further evaluated using multi-TE ASL and an independent, invasive method for local measurement of cerebral oximetry. If the two measurements were correlated, this would show that multi-TE ASL could potentially be a novel non-invasive technique for oxygen extraction fraction assessment.

There is a difference in the extravascular tissue $T2_{EV}$ measured in the cerebellum region compared to the cortical region. The lower T2 in the cerebellum region (~33ms) compared to the cortical region (~36ms) is likely to be due to the increase in the white matter that is present in the cerebellum region. It has been reported that water transfer rate in human brain white matter is faster compared to grey matter as measured by diffusion-weighted (DW) ASL [128]. More accurate regional segmentation would be needed to separate the contributions from the grey matter and the white matter in the mouse brain to examine potential differences.

Assessing the different brain regions shows that the group-wise analysis technique is able to detect an extremely small intravascular fraction (as shown in the cerebellum data at TI = 1500ms) or small extravascular fraction (in the cortex at TI = 800ms). This has been achieved through the group-wise fitting that calculates a single mean $T2_{IV.}$ When $T2_{IV}$ is measured individually, the two-compartment model is not able to fit to the data reliably, especially for the cerebellum brain region. It may be due to there being an uneven contribution between the two compartments, at TI = 1500ms, and a very short $T2_{IV.}$ A further shortfall of this study was the absence of the individual arterial transit time data, which were not possible to calculate due to a technical error during the image acquisition. There may be differences in the arterial transit time between the cortical and cerebellar brain regions, which could have an impact on the exchange time measurements. Arterial transit time measurements should be collected in future studies to improve the accuracy of the individual exchange times.

In this pilot study, the cortical exchange time is marginally higher than previously measured. This is a consequence of the additional shorter inflow time (800ms) incorporated into the model. The shorter inflow time was included to ensure that the ASL signal would have contribution from both the intravascular and extravascular compartment for at least one inflow time. The inflow time of 800ms results in an exchange time which is longer than TI = 1500ms. This would suggest that that there is a limitation with the two-compartment kinetic perfusion model. Since this model assumes that the leading edge of the labelled water bolus linearly transfers from the capillary bed into the extravascular tissue, it may be that the intravascular signal contributions is measured from a different location the vasculature tree at the shorter inflow time.

4.5 Conclusion

The multi-TE ASL technique has been successfully implemented on the 9.4T Bruker imaging system, with several hardware enhancements and pulse sequence improvements. The optimised sequence yielded very similar exchange time measurements compared to the previous results recorded using the 9.4T Varian/ Agilent system, as reported in **Chapter 2**.

The technical improvement implemented using the 9.4T Bruker system demonstrate the scope of the technique towards brain-wide application. As an initial step, a pilot study was performed to probe the BBB water permeability in the cerebellar tissue of the mouse brain. Despite the results suggesting there were no significant difference regional variation of BBI water permeability between the cortical and cerebellar region; the multi-TE ASL technique is able to assess different brain regions, and can be applied to mouse models of neurodegeneration to better understand the dynamic role of BBI water permeability in pathology.

4.6 Appendix: Ongoing Proof of Concept work - Multi-echo FAIR-T2-EPI

The multi-TE ASL technique show promises to be a useful tool for the early detection of neurodegenerative diseases, but for this to be effective in a clinical setting a reduction in scan duration is always desirable. The time for clinical scans is always restricted, as there are often several different scans that need to be acquired within a given session. In pre-clinical imaging the acceptable scan time is often significantly longer than in the clinical setting, but if the time of the MRI sequence is reduced this would allow an increase in the number of repetitions, spatial coverage, spatial resolution and/or range of inflow times as well as a higher throughput to be implemented in the imaging session.

Until now, the multi-TE ASL sequences used in this thesis have been implemented using a single echo for each TR, see pulse sequence diagram shown in **Figure 4.10A**. While this technique has proven to produce consistent results, an optimised multi-TE ASL sequence would be beneficial to reduce the scan time for the technique and improve the scope for clinical application. Therefore, I have designed a new MRI sequence (FAIR-T2-EPI) on the Bruker 9.4T system that combines a labelling pulse with a multi-TE EPI sequence so that all of the echo times can be captured within a single repetition time to significantly reduce the acquisition time of the MRI sequence, **Figure 4.10B**.

The new MRI sequence was designed with a T2-EPI MRI sequence as the backbone. This sequence is able to collect an array of T2-weighted images, following a single excitation pulse, with echo times at an equal echo spacing using an EPI readout. The T2-EPI sequence was combined with a labelling pulse that alternates between an inversion pulse that inverted a global region (non-selective slice) and inverting a slice-selective region (selective slice).

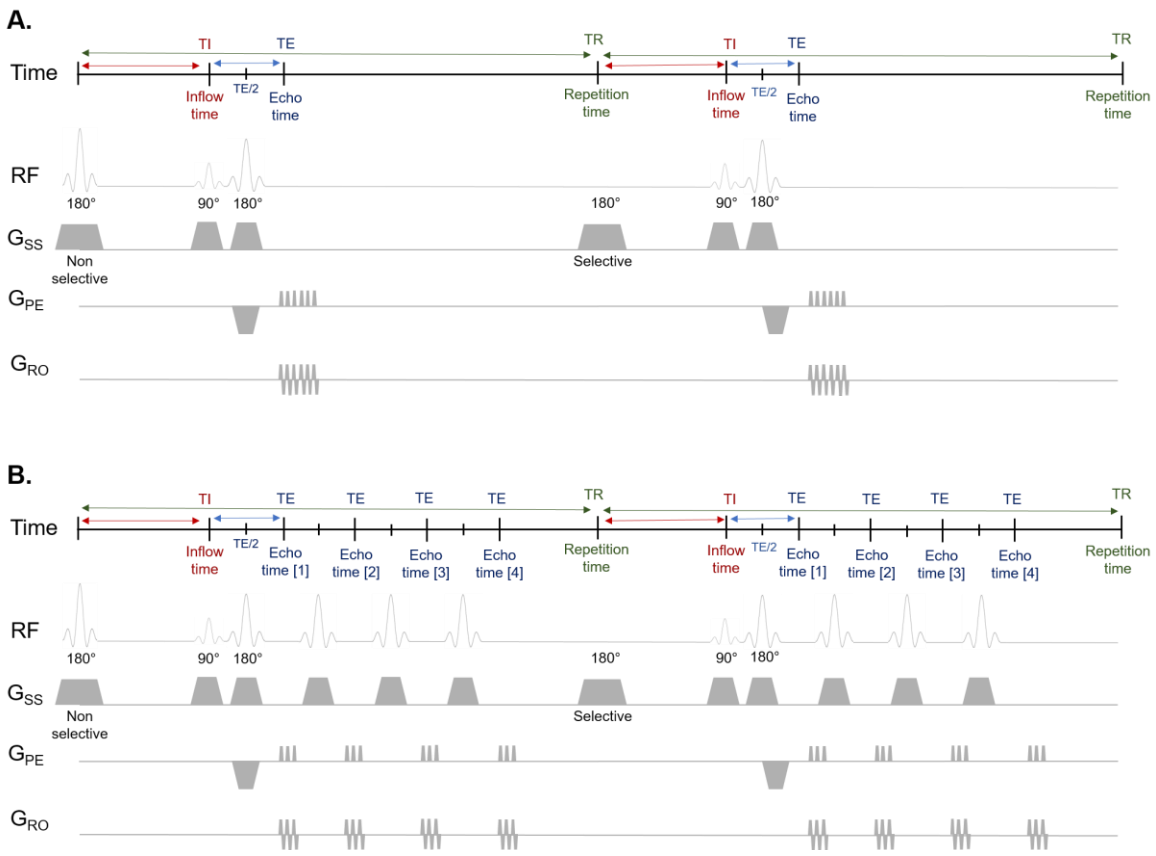

Figure 4.10: Schematic of Pulse Sequence **A.** Flow-alternating inversion recovery (FAIR) sequence for single echo time**. B.** FAIR-T2-EPI sequence with multiple echo time acquisition displaying timings including: inflow time (TI), echo time (TE) and repetition time (TR), radio-frequency (RF) pulses and gradients: slice selective (G_{SS}), phase encoding (G_{PE}) and readout (G_{RO}).

The new pulse sequence was coded in C++ using the Bruker sequence modules on Paravision v6.0. The timings were calculated to determine the inversion pulse time, inflow time and repetition time as in the general pulsed ASL sequence. Multiple echo times that occur with a given echo spacing were incorporated into the sequence and were implemented to fit within a single repetition time. A simulation of the FAIR-T2-EPI pulse sequence is shown in **Figure 4.11**.

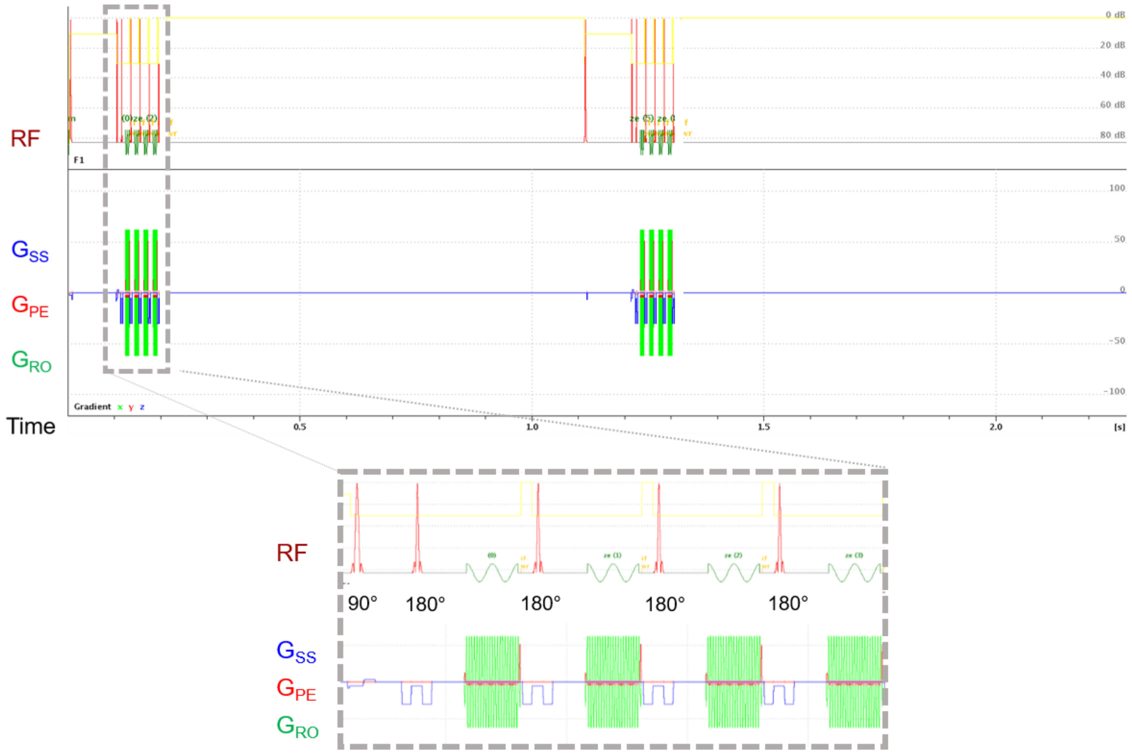

Figure 4.11: Simulated FAIR-T2-EPI sequence. Radiofrequency (RF) pulses (in red) for non-selective and selective inversion and for spin echoes, slice selective gradient (blue), phase encode gradient (red) and readout gradient (green) with sequence parameters: TI = 100ms; TR = 1156ms; Echo Spacing = 20ms; Echoes = 5. Bottom inset: magnification of the RF pulses with flip angle indicated and magnetic gradients demonstrating the multiple echo acquisition.

The FAIR-T2-EPI was tested on a single C57/Bl6 mouse for proof-of-concept. The sequence parameters were selected to be similar to those previously used in studies presented in this thesis: Inflow time (TI) = 800 ms and 1500 ms; Echo spacing = 20ms, echo times (TE) = 20 ms, 40 ms, 60 ms, 80 ms; TR = 5000 ms; FOV = 25 x 25 mm; Slice thickness = 2 mm; Repetitions = 10. Scan time: 1 min 40 secs.

As a first step, the data was analysed using a single compartment model with apparent transverse relaxation ($T2_{app}$) reflecting a combination of the signal derived from both the intravascular and extravascular compartments – as in **Chapter 2: Single Compartment Model: Apparent Transverse Relaxation, T2.**

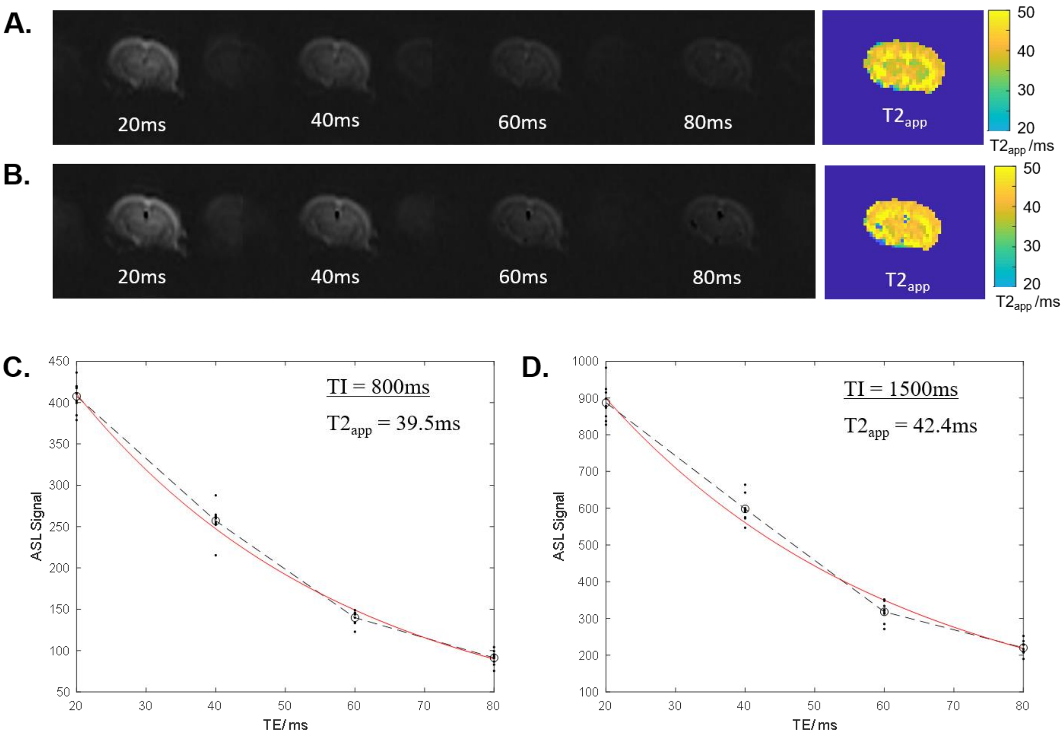

Figure 4.12: $T2_{app}$ measurements from FAIR-T2-EPI sequence. ASL images at increasing echo time (marked on images) for calculation of $T2_{app}$ maps (right) for the same animal at **A.** TI = 800ms **B.** TI = 1500ms. ASL signal, for individual repetitions with mean value marked on plot, derived from the cortical region of interest for quantitative measurement of $T2^{app}$ at **C.** TI = 800ms **D.** TI = 1500ms with the red line to indicate the mono-exponential fitting.

The FAIR-T2-EPI sequence is able to acquire high quality ASL images at increasing echo time in a rapid scan time, **Figure 4.12A, B**. Of note, there is still a detectable signal at both inflow times, at a longest extended echo time of 80ms. The $T2_{app}$ was measured at 39.5ms and 43.4ms, at inflow times of 800ms and 1500ms respectively, **Figure 4.12C, D.** The increase in $T2_{app}$ is the proof-of-concept that the new sequence is sensitive to the labelled vascular water moving from intravascular to the extravascular compartment, as demonstrated in **Chapter 2: Results.** Although the absolute values are higher than the previous measurements, the same characteristic trend of an increasing T2 is demonstrated using this novel sequence.

Further optimisation of the imaging parameters is required to sample true transverse relaxation signal behaviour, which would enable a bi-exponential fitting to estimate the IV fraction and quantify the exchange time. Given the significant reduction in the total scan time, this mean that a greater number of averages can be collected in the same scan time which would largely boost the SNR. This may also reduce the errors and artefacts that are associated with motion of the animal.

This initial proof-of-concept study demonstrates that the new FAIR-T2-EPI approach shows promise as a potential MRI sequence that can be used to measure water permeability across the BBI in a substantially reduced scan time.

Chapter 5

Assessing the effect of Aquaporin-4 Polarisation on Blood-Brain Interface Permeability to Water

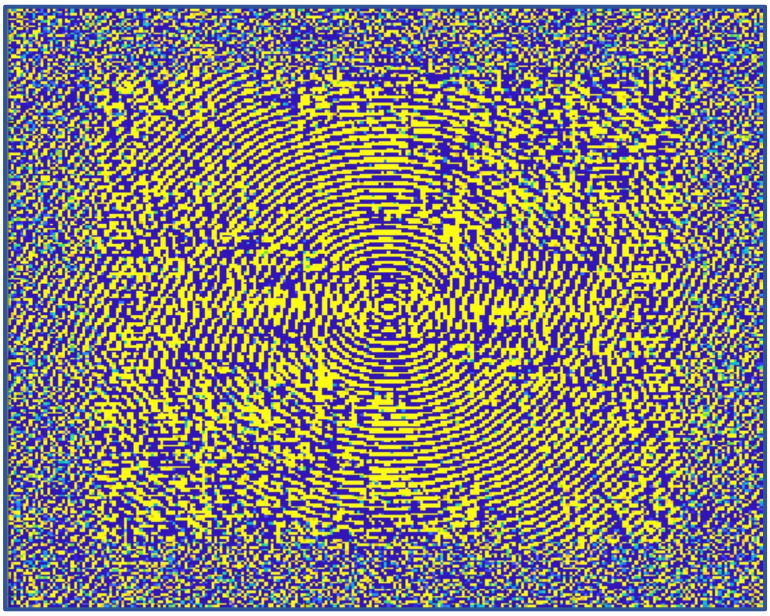

k-space, α-syntrophin-deficient mouse brain

Aim

The aim of this chapter is to characterize the effect of aquaporin-4 (AQP4) polarisation on measures of blood-brain interface (BBI) permeability to water using multiple echo time arterial spin labelling (multi-TE ASL). The previous chapter demonstrates that multi-TE ASL is able to detect differences in the BBI water permeability measure in the absence of AQP4. However, several studies have reported that changes of the polarisation (i.e. location on the endfeet of astrocytes facing the blood vessels) rather than overall expression of AQP4 is associated with brain pathology. Changes to AQP4 polarisation in the glymphatic system (and other mechanisms) play a role in Alzheimer's Disease (AD). Therefore, the application of multi-TE ASL to a genetic mouse model, α-syntrophin-deficient ($Syn^{-/-}$), where the AQP4 polarisation is down-regulated, would help to better understand the impact of AQP4 polarisation on the measured BBI permeability to water.

In this study, multi-TE ASL was applied to the cortical and cerebellar brain regions of the $Syn^{-/-}$ mice to examine the effects of AQP4 polarisation. Applying the technique to the two brain regions will further assess the regional effects of AQP4 polarisation on the measures of BBI permeability to water. Overall, this study aims to understand the effect of expression vs polarisation of AQP4 on the BBI water permeability measures.

This work was presented as power-pitch and poster at BRAIN & BRAIN PET 2019, Yokahoma, Japan and was selected as part of the Early Career Investigator Award session.

5.1 Introduction

Aquaporin-4 (AQP4) water channels are abundantly expressed on the endfeet of astrocytes, which are highly localized to the interfaces between the brain parenchyma and the blood vessel compartment or cerebrospinal fluid (CSF) compartment [132]. The polarity of the AQP4 channels refers to the channels being arranged in a regular order at the blood-brain interface (BBI) to facilitate the rapid transfer of water into and out of the brain parenchyma. Marked changes to AQP4 polarisation are associated with pathological conditions such as traumatic brain injury (TBI), ischemic stroke and Alzheimer's Disease (AD) [51, 98, 157].

In recent years, there has been increasing interest in examining AQP4 polarisation due to the role of AQP4 as a functional regulator of the glymphatic system. The alteration in AQP4 polarisation and location seems to have an effect on glymphatic function, which is thought to be related to the clearance of interstitial solutes, such as amyloid-β (Aβ) [45]. The extent of the depolarisation of AQP4 in the human brain appears to correlate with the progression/severity of AD in post-mortem human brain tissue [51]. However, there remain many unanswered questions surrounding the glymphatic system and the specific contribution of AQP4 [158].

AQP4 takes a tetramer structure when it is located in the plasma membrane, which consists of higher order structures called orthogonal array of particles (OAP). It has been suggested that this structure facilitates an increased water permeability, cell-cell adhesion and AQP4 polarisation to the endfeet of astrocytes [50]. AQP4 polarisation is due to the anchoring of the water channels to the basal lamina (otherwise known as the basement membrane) via a group of proteins called the dystrophin-associated protein complex (DAPC). DAPC consists of α-Syntrophin (α-Syn), α-dystrobrevin (α-DB), 71kD isoform of dystrophin (DP71), β-dystroglcan (β-DG) and α-dystroglycan (αDG), see **Figure 5.1A**. Each of these proteins are important for anchoring and stabilizing the AQP4 in the location facing the basal lamina at the BBI.

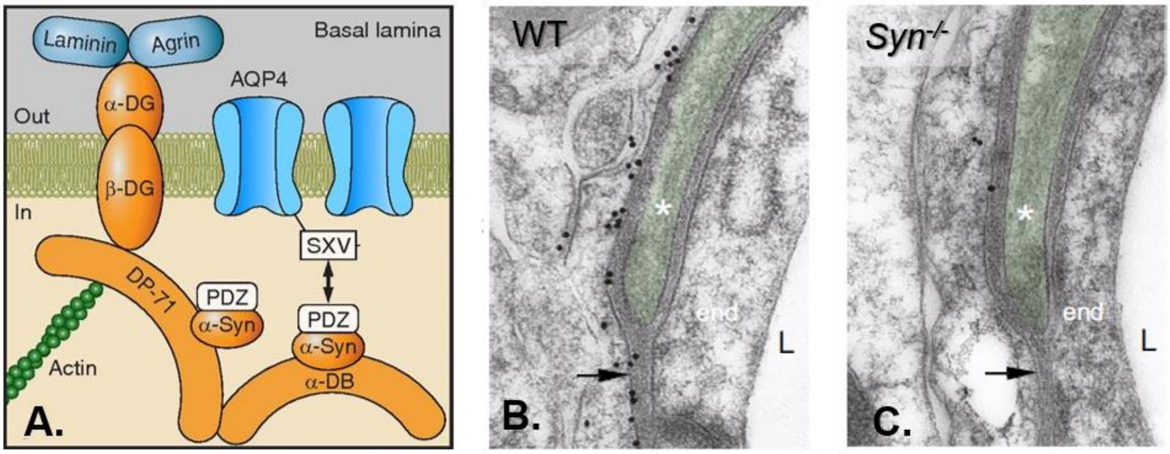

Figure 5.1: Anchoring of the AQP4 molecule to the perivascular location. **A.** The dystrophin-associated protein complex (DAPC) consisting of α-Syntrophin (α-Syn), α-dystrobrevin (α-DB), 71kD isoform of dystrophin (DP71), β-dystroglcan (β-DG) and α-dystroglycan (αDG), the AQP4 interacts directly or indirectly with the PDZ domain of α-syntrophin. **B.** Wild-type (WT) mouse and **C.** α-syntrophin KO (*Syn*$^{-/-}$) mouse of brain slice from the hippocampus demonstrating perivascular AQP4 immunogold labelling (black circles) in with the arrow indicating the membrane abutting the endothelium (end), the capillary lumen (L) and part of the pericytes (colored green with asterisk). Schematic adapted from: [150].

Alterations to AQP4 polarisation manifests in several conditions including AD. There are several ways to disrupt the distribution and location of the AQP4 water channel, in particular by the removal of the anchoring proteins that form the DAPC. The genetic removal of the α-Syn protein was established in *Syn*$^{-/-}$ mice where the AQP4 channels were found to be no longer facing the blood vessel, but were found on the cell body of the astrocyte, **Figure 5.1B, C** [159]. Interestingly, in *Syn*$^{-/-}$ mice the AQP4 channels are vastly reduced from the perivascular location next to the BBI while the overall level of AQP4 in the brain tissue (i.e. overall AQP4 expression) is maintained, which may be crucial to better understand the function of AQP4 polarisation [139, 160]. This is important since the reduction in AQP4 polarisation seems to correlate with the disease progression and cognitive decline in AD [51].

There have been several techniques that are able to probe AQP4 polarisation. The initial development of the *Syn*$^{-/-}$ mice used immunogold particle staining to demonstrate that the AQP4 were no longer present at the BBI, **Figure 5.1B, C.** Immunofluorescence using a local confocal microscopy is a further method that is able to quantitatively measure the AQP4 expression at the perivascular endfeet location and compare to the quantity in the remaining tissue to give an index of AQP4 polarisation [133]. Similarly, frozen and fixed human tissue sample has also been analysed for the extent of AQP4 polarisation using immunofluorescence techniques, which were confirmed using Western blot approaches [51]. The glymphatic function of *Syn*$^{-/-}$ mice has also been assessed via DCE-MRI following an inter-cisterna magna injection of gaditeridol contrast agent. T1-weighted images demonstrated a reduction in the influx of the contrast agent in *Syn*$^{-/-}$ mice, suggesting a reduced glymphatic function [47]. Though the AQP4 channels do not directly transport the contrast agent, they play a role in determining the rate that solutes can pass into the brain parenchyma [161].

The distribution of AQP4 is heterogeneous in both the human and rodent brain, with the cerebellum having the most abundant accumulation of AQP4, and the lowest expression being the cortical and hippocampal brain regions [150, 151]. The biological mechanisms that underpin the heterogeneity of the water channels across the brain remain largely unknown. Therefore, there is a need to probe the different regions of the brain to better understand the functional consequences of the density, location and polarisation of AQP4 water channels.

Currently, there are limited minimally invasive techniques that are able to target AQP4 polarisation and would, therefore, be applicable within a clinical setting. The use of *Syn*$^{-/-}$ mice has been beneficial to study the effect of AQP4 polarisation. Therefore, given the lack of non-invasive techniques that are able to target AQP4 polarisation, this study aimed to apply the multi-TE ASL technique to the *Syn*$^{-/-}$ mice to assess the effect of AQP4 polarisation on BBI permeability to water. The *Syn*$^{-/-}$ mice provide a model that more closely mimics the changes that occur in the human brain in pathological condition than the total removal of AQP4 that was modelled in the *Aqp4*$^{-/-}$ mice that were imaged in **Chapter 3**. BBI permeability to water was measured in both the cortex and the cerebellum regions of the mouse brain, for regional assessment moving towards a brain-wide approach. The hypothesis was that there would be a reduction in the BBI water permeability, in both the cortical and cerebellar brain regions, with the reduction of perivascular AQP4 at the BBI in the *Syn*$^{-/-}$ mice.

5.2 Method

5.2.1 Experimental Protocol

5.2.1.1 Animal Preparation

All experiments were performed in mice in accordance with the European Commission Directive 86/609/EEC (European Convention for the Protection of Vertebrate Animals used for Experimental and Other Scientific Purposes) and the United Kingdom Home Office (Scientific Procedures) Act (1986). Eleven *Syn*$^{-/-}$ mice (n = 5, female and n= 6, male) at 7 ± 1 months old provided by our collaborators O.P. Ottersen and E.A. Nagelhus at University of Oslo [162] and ten age-matched wild-type (WT) C57/Bl6 (n = 4, female and n = 6, male) (Charles River). All mice were acclimatised for some months prior to data acquisition in an animal house on a 12 h light/12 h dark cycle with food and water provided *ad libitum*. For animal preparation, anesthesia, set-up and physiological monitoring refer to **Chapter 4: Methods: 9.4T Bruker Imaging Protocol.**

5.2.1.2 Imaging Protocol

For MRI equipment and multi-TE ASL sequence parameters refer to **Chapter 4: Methods: 9.4T Bruker Imaging Protocol.** In this study the multi-TE FAIR protocol was applied to two slice positions (one central and one caudal in the mouse brain) in one scanning session to acquire data from both a cortical and cerebellum brain region. Repetitions = 8. Scan time per slice: ~40 mins (~20 mins per inflow time).

For the measurement of the arterial transit time (δ_a) and cerebral blood flow (CBF), a multi-TI ASL protocol was implemented with imaging parameters: inflow time (TI) = 200, 300, 400, 500 ms, echo time (TE) = 10 ms; repetition time (TR) = 10 000 ms; matrix size = 64 x 64; FOV = 25 x 25 mm; repetitions = 5. Scan time per slice: ~8 mins.

5.2.2 Data Analysis

All data was evaluated using Matlab R2018a (Mathworks) and GraphPad Prism 8 (Prism). For the data analysis pipeline for quantification of the intravascular fraction and exchange time, refer to **Chapter 4: Methods: Data Analysis**. Three multi-TE ASL data sets from the WT group and four multi-TE ASL data sets from the *Syn*$^{-/-}$ group were excluded from the final analysis as they contained severe artefacts which may have arisen from poor shimming or animal motion, example ASL images for the cortical slice and the cerebellum slice are shown in **Figure 5.2**.

The arterial transit time was evaluated multi-TI ASL imaging using the analysis protocol outlined in **Chapter 2: Methods: Data Analysis**. The individual arterial transit times were incorporated into the two-compartment kinetic perfusion model for each animal. There were three data sets where the arterial transit times resulted in a negative value, which is physiologically impossible. The average arterial transit time for the group was used to evaluate the individual exchange time of these animals, since this would be the most relevant choice of arterial transit time since an arterial transit time equal to zero is physically impossible. There was one arterial transit time data point and one exchange time measurement that were identified as outliers using the ROUT coefficient (Q set at 1%), and therefore excluded from the final analysis.

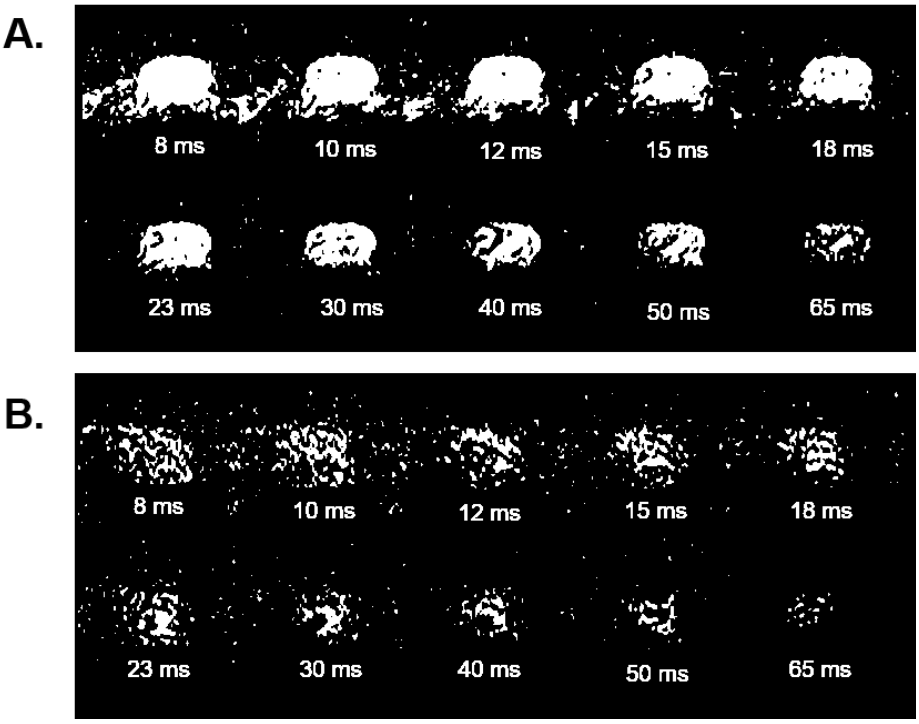

Figure 5.2: ASL images with severe artefacts that were excluded from the final analysis for **A.** Cortical slice and **B.** Cerebellar slice from a representative animal.

The exchange time maps were generated by manually segmentation of the brain region, and pixel-wise modelling of the intravascular fraction, incorporated with an $T2_{EV}$ map, ATT map and a the fixed shared $T2_{IV}$ value.

5.2.2.1 Statistical Analysis

All data are reported as the mean and associated error (± standard deviation). A 2-way ANOVA with a Bonferroni's multiple comparison test was used to assess the dependence of the intravascular fraction and the $T2_{EV}$ on i.) genotype of mice ($Syn^{-/-}$ and WT controls) and ii.) inflow time. For parameters in which a dependence of inflow was not expected, exchange time, arterial transit time and CBF, an unpaired two-tailed student's t-test was used to assess any differences between the $Syn^{-/-}$ mice and WT controls. A Sidak's multiple comparisons test was used to compare the exchange time and arterial transit time for the different brain regions. For all tests $p < 0.05$ was considered to be a statistically significant result.

5.3 Results

The ASL signal acquired from the multi-TE ASL protocol fits to the bi-exponential model well in both the cortical and the cerebellum regions at both inflow times**, Figure 5.3, 5.4**. The intravascular fraction was significantly decreased as the inflow time was increased in all groups ($p < 0.001$), which would indicate that the technique is capturing the labelled vascular water moving into the extravascular tissue as the inflow time is increased.

In the cortical brain region, the intravascular fraction of the ASL signal decreased from 0.62 ± 0.12 to 0.27 ± 0.11 in the WT mice compared to 0.55 ± 0.17 to 0.22 ± 0.10 in the *Syn*$^{-/-}$ mice, at 800 ms and 1500 ms respectively in both animal groups, **Figure 5.3**. There were no significant differences in cortical ASL intravascular fraction measured between the two animal groups at either inflow times (adjusted p values: $p = 0.66$ at 800ms and $p > 0.999$ at 1500ms) suggesting that the rate of water exchange of vascular water into the extravascular is relatively consistent in the cortex when there is a reduction of perivascular AQP4 water channels at the BBI. Indeed, there were no measureable differences in the cortical exchange time between the *Syn*$^{-/-}$ mice (332 ± 103 ms) and the WT controls (385 ± 114 ms), $p = 0.38$, **Figure 5.5B**.

In the cerebellum brain region, the intravascular fraction was measured at 0.72 ± 0.17 and 0.71 ± 0.13 at TI = 800ms and 0.26 ± 0.08 and 0.38 ± 0.13 at TI = 1500ms in the WT and *Syn*$^{-/-}$ mice respectively at each inflow time, **Figure 5.4**. There were no measurable difference at TI = 800ms however there was a significant increase in intravascular fraction in *Syn*$^{-/-}$ mice at TI = 1500ms (adjusted p-values: $p > 0.999$ and $p = 0.05$ respectively). The exchange time is significantly increased in the cerebellum of *Syn*$^{-/-}$ (531 ± 21 ms) relative to WT (396 ± 82 ms), $p = 0.002$, which suggests that there is a slower water transfer across the BBI when the AQP4 water channel have been reduced from the endfeet of astrocytes within the cerebellum, **Figure 5.5B**.

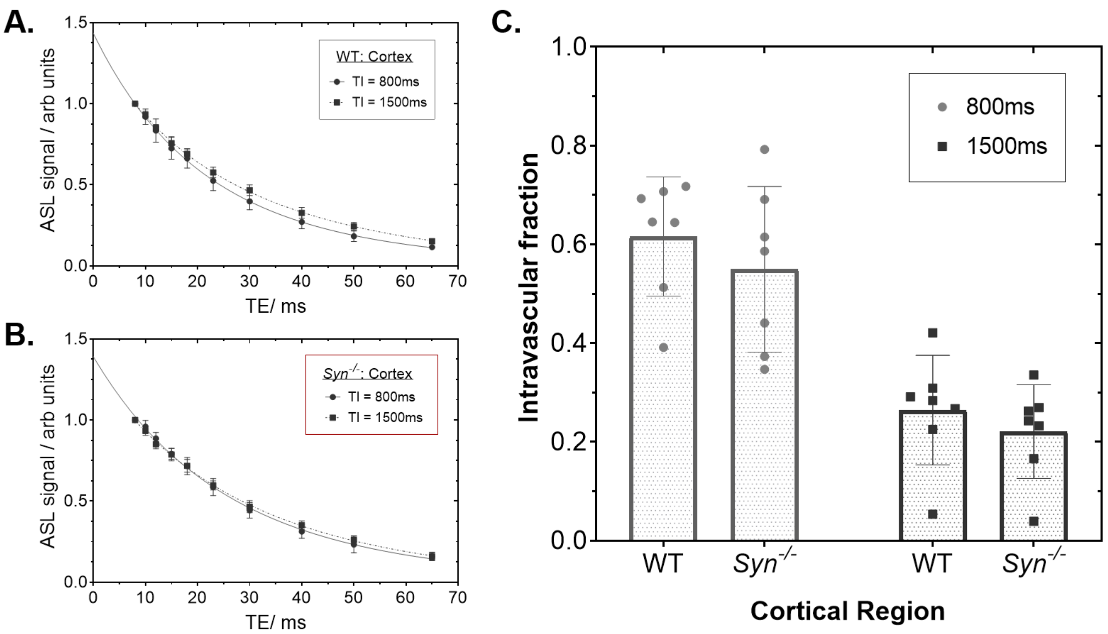

Figure 5.3: ASL signal decay and intravascular fraction of cortical brain region. ASL signal decay at TI = 800 ms and 1500 ms at increasing echo time for **A.** Wild-type (WT) mice and **B.** α-syntrophin-deficient mice (*Syn*$^{-/-}$). **C.** Intravascular fraction for individual animals at inflow times (800 ms and 1500 ms) with mean value and associated error (± std) indicated on the plots.

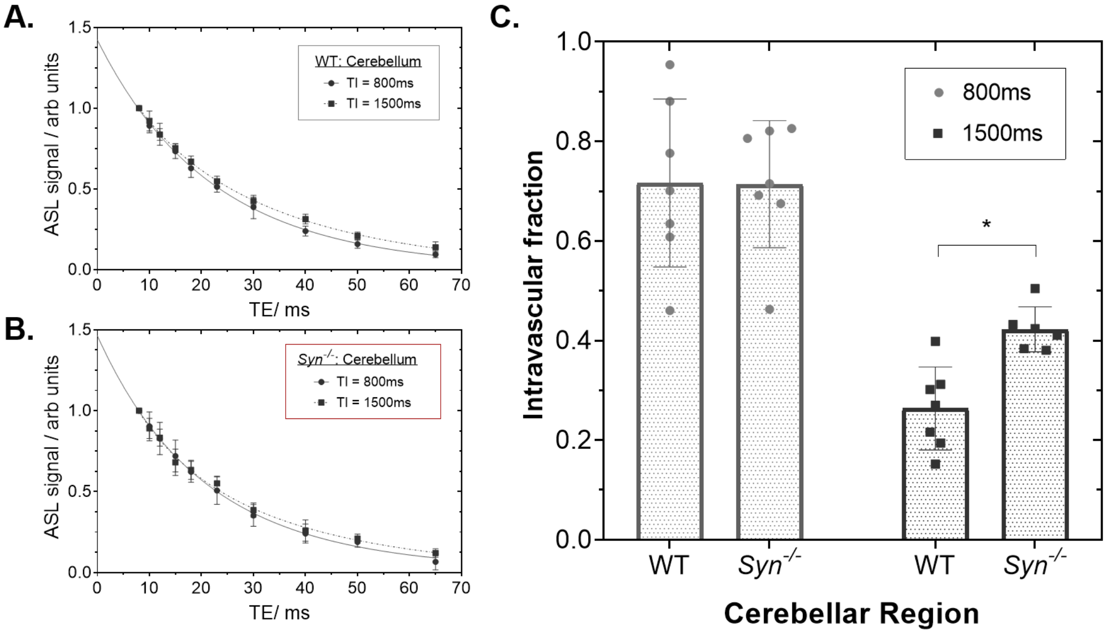

Figure 5.4: ASL signal decay and intravascular fraction of cerebellum brain region. ASL signal decay at TI = 800 ms and 1500 ms at increasing echo times for **A.** Wild-type (WT) mice and **B.** α-syntrophin-deficient (*Syn*$^{-/-}$) mice **C.** Intravascular fraction for individual animals at inflow times (800 ms and 1500 ms). The mean values and associated error (± std) are displayed on the plot.

There was a significant difference in exchange time between the cortical and cerebellum brain regions in the *Syn*$^{-/-}$ mice, p = 0.001. This would suggest that there is a heterogeneous effect on the BBI water permeability index in the different regions of the *Syn*$^{-/-}$ mice. Whereas, there was no measurable difference between the cortical and cerebellum brain regions in the WT controls, p = 0.97.

There are no measurable differences in the arterial transit time in the cortical region between the WT mice (67 ± 82 ms) relative to the *Syn*$^{-/-}$ mice (106 ± 26 ms), p = 0.87. Also, no differences were shown in the cerebellum region of the WT (152 ± 40 ms) or *Syn*$^{-/-}$ (125 ± 50 ms), p = 0.28, **Figure 5.6A**. This would indicate that the vascular architecture is maintained when the AQP4 is reduced around the perivascular region of BBI. Of note, there was a significant increase in the arterial transit time in cerebellum brain region compared to the cortical brain region in the WT animal, p = 0.014. No measureable changes were reported between the cortical and cerebellar brain regions in the *Syn*$^{-/-}$ mice, p = 0.78.

CBF is significantly lower in the cortical region of *Syn*$^{-/-}$ mice (187 ± 25 ml/100g/min) relative to the WT controls (260 ± 44 ml/100g/min), p = 0.023, **Figure 5.6B**. This indicates that there are haemodynamic alterations in the cortical regions with the removal of α-syntrophin protein in the *Syn*$^{-/-}$ mice. There were no measurable differences in the CBF within the cerebellum brain region of *Syn*$^{-/-}$ mice (215 ± 100 ml/100g/min) compared to WT mice measured at (270 ± 22 ml/100g/min), p = 0.18.

The cortical intravascular T2 ($T2_{IV}$) was measured at 17.2 ± 1.5 ms and 11.1 ± 1.4 ms in the WT mice, relative to 19.9 ± 2.5 ms and 14.9 ± 3.6 ms in the *Syn*$^{-/-}$ mice, at inflow times 800 ms and 1500 ms respectively for both animal groups. This suggests that measured T2 relaxation rate derived from the intravascular compartment is similar between the two groups of animals, statistical analysis for this parameter is not possible since only a single shared $T2_{IV}$ is derived from the analysis pipeline. The cerebellar $T2_{IV}$ was measured at 19.4 ± 3.1 ms to 8.4 ± 2.5 ms in the WT animals compared to 17.2 ± 3.8 ms and 9.1 ± 2.5 ms, at inflow times 800 ms and 1500 ms respectively for each animal group. This demonstrates that there is a consistent decrease in the $T2_{IV}$ as the inflow time increases in both brain regions and animal groups, as previously reported in **Chapter 4: Results: Pilot Study: Regional variation in BBI permeability to water**. There is also a reduction is the $T2_{IV}$ measured in the cerebellar region compared to the cortical region which might suggested that there a larger oxygen extraction within the cerebellum region.

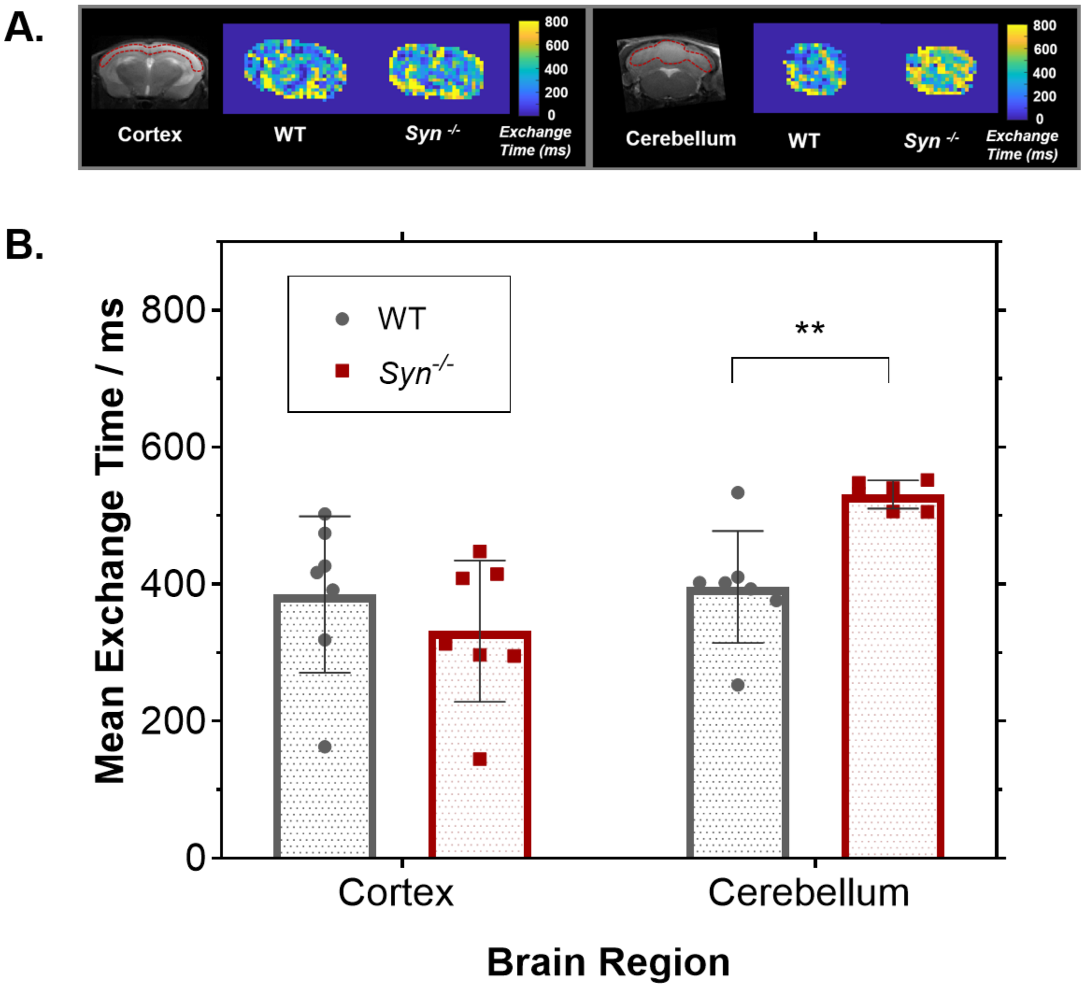

<u>Figure 5.5: Exchange Time measurements from the cortical and cerebellum brain region.</u> A. Exchange time maps of the cortex and the cerebellum in a representative wild-type (WT) and α-Syntrophin-deficient (*Syn*$^{-/-}$) mice, with an anatomical image on left (with ROI shown in red). **B.** Mean exchange time measurements in individual WT *and Syn*$^{-/-}$ mice in cortical and cerebellar brain regions**.** ** indicates $p < 0.01$.

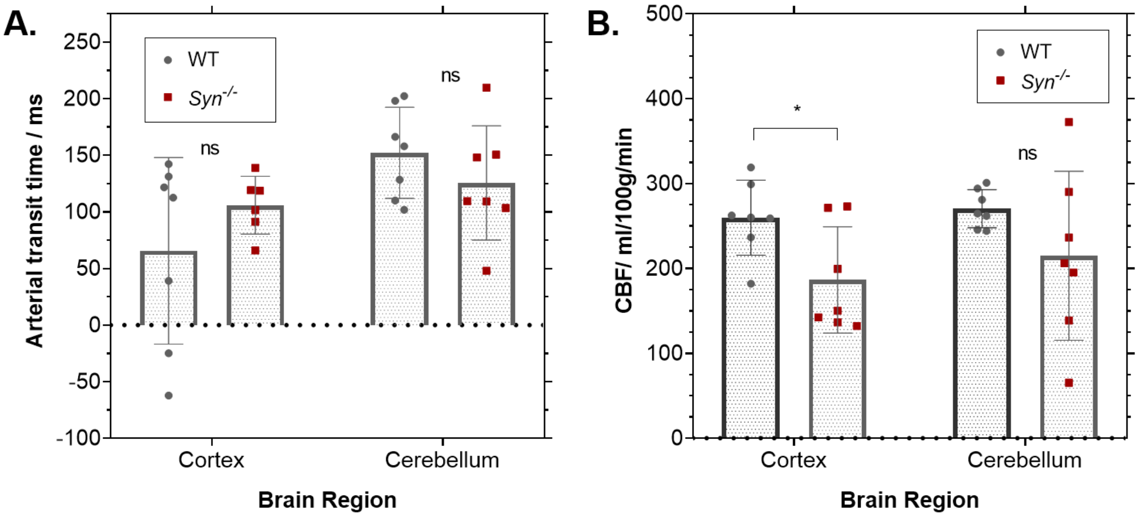

Figure 5.6: Cerebral haemodynamics in the cortical and cerebellum brain regions. A. Arterial transit time measurements for individual WT and *Syn*$^{-/-}$ mice and **B.** Cerebral blood flow (CBF) measurements for cortex and cerebellum brain regions of the WT mice and *Syn*$^{-/-}$ mice. All plots display the mean parameter and associated error (± std). * indicates $p < 0.05$.

The cortical extravascular tissue T2 ($T2_{EV}$) was measured at 36.2 ± 1.7 ms relative to 38.1 ± 1.0 ms at 800ms, ($p = 0.15$) and 34.4 ± 2.0 ms relative to 34.7 ± 2.1 ms at 1500 ms in the WT mice *Syn*$^{-/-}$ mice respectively, for each inflow time ($p = 0.0009$ for inflow time dependence; $p = 0.14$ for genotype dependence). The cerebellar $T2_{EV}$ was measured at 33.7 ± 1.1 ms compared to 34.6 ± 2.6 at 800 ms ($p = 0.711$) and 30.7 ± 0.8 ms compared to 31.7 ± 1.9 ms at 1500 ms ($p = 0.97$) in the WT controls and *Syn*$^{-/-}$ mice respectively for each inflow time ($p < 0.0001$ for inflow time dependence and $p = 0.50$ for the genotype dependence). The slight increase in the $T2_{EV}$ in the *Syn*$^{-/-}$ mice may indicate that there is a slightly increase in the brain water content [163].

5.4 Discussion

The multi-TE ASL technique was used to assess the rate of vascular permeability to water with a reduction in AQP4 polarisation as modelled by the *Syn*$^{-/-}$ mice. There was a significant increase (34%) in water exchange time to reflect reduction in the BBI permeability to water, with reduced AQP4 polarisation at the BBI, in the cerebellum brain region. However, there were no measurable differences in the vascular water permeability in the cortical brain region with the removal of the AQP4 at the BBI. There were no regional differences in the exchange time reported between cortical and cerebellar brain regions of WT controls, however there was a significant increase in exchange time in the $Syn^{-/-}$ mice. Conversely, in the cortical brain region the CBF was measured to be significantly lower in the $Syn^{-/-}$ mice compared to the WT controls, whereas there was no measurable CBF difference in the cerebellum. The arterial transit time was not affected in either brain region with the depolarisation of the AQP4 channels. Overall, this highlights the heterogeneity in the BBI permeability to water across different regions of the mouse brain and the possible correspondence between the cerebral haemodynamics and the water permeability measurements.

The polarisation of AQP4 channels (i.e. located at the endfeet of astrocytes as they connect to the basal lamina) is thought to be important for glymphatic function. Previous studies have recorded a decrease in the influx of MRI contrast agent into the brain parenchyma in $Syn^{-/-}$ mice [47]. To my knowledge, there have not been any non-invasive techniques that have been used to directly assess AQP4 polarisation. The present study, measuring BBI water permeability, provides evidence that the multi-TE ASL technique is sensitive to the location of the AQP4 at the BBI in the cerebellum brain region, where there is a higher exchange time indicating an increase in the time taken for the water to transfer across the BBI. No difference between the cortical exchange time was measured between the $Syn^{-/-}$ and the WT controls, which suggests that there is a regional dependency of the rate of water flux transferring in the brain with a reduction in AQP4 at perivascular location. But crucially this technique is potentially a promising non-invasive tool to further probe change to AQP4 polarization in the brain.

It is likely that the regional variation in the BBI water permeability is linked to the cerebral haemodynamics, and vascular heterogeneities between the animal groups.

There was a significant reduction in the CBF measured in the cortical brain region of the *Syn*$^{-/-}$ mice relative to WT controls. Previous studies have demonstrated that a decrease in CBF is coupled with an increased permeability as the molecules are able to pass across the BBI into the brain parenchyma more readily when they are moving through the vasculature at a slower rate [164]. CBF values in the cerebellum region of the *Syn*$^{-/-}$ mice were similar, though there was also a decreasing trend in this region but a higher intra-animal variability, compared to the WT controls. It might indicate that there is a difference in the CBF regulation between the animal groups, and may explain the reduced water permeability measured in the cortical brain region of the *Syn*$^{-/-}$ mice. Future studies could be performed varying the CBF, by using a gas challenge for example, to measure the effects on the exchange time parameter as a measure of water permeability. Alternatively, the implementation of a steady state MRI method of measuring water exchange across the BBI, such as MFAME – MRI, might be useful to quantify the permeability surface product PS_w as an index of permeability, since this technique is less susceptible to flow effects.

The ratio between the α-syntrophin protein and AQP4 water channel is consistent across the different regions of the mouse brain [150]. Therefore, the extent of the reduction of AQP4 from the perivascular endfeet, in the *Syn*$^{-/-}$ mice, should be the same in both the cortical and the cerebellar brain regions. This would indicate that there may be other mechanisms which are facilitating the transfer of water across the BBI that might be different in the cortical region compared to the cerebellum. It is known that the vascular density and the white matter to grey matter tissue composition are both higher within the cerebellum region, which may be driving the difference in the BBI water permeability in the cerebellum region in the *Syn*$^{-/-}$ mice. Further experiments to measure the capillary density or tissue composition within the various brain regions may help to better understand differential regional effects related to the water permeability.

The arterial transit time was maintained between the *Syn*$^{-/-}$ mice and the WT controls in both the cortical and cerebellar brain regions. This demonstrates that the removal of the AQP4 from the locations of the BBI does not affect the passage of the labelled vascular water arriving at the imaging slice from the feeding arteries supplying both of the brain regions. The arterial transit times from the WT mice are significantly faster in this study than those measured in the WT animals in the previous study (**Chapter 3**) using the Agilent system, $p = 0.036$. This might be due to the smaller/ thinner slice selective inversion width used on the Bruker system compared to the Agilent system. There was also a noticeable increase in the variability of the arterial transit time when taking the measurements using the Bruker imaging system; currently the reason for this increased variability are unknown.

Higher extravascular tissue $T2_{EV}$ was measured in the *Syn*$^{-/-}$ mice in both cortical and cerebellar brain regions, which may be due to an greater water accumulation in the brain parenchyma of *Syn*$^{-/-}$ mice, which is similar to the higher $T2_{EV}$ reported in the AQP4 knock-out mice in **Chapter 3** [163]. The *Syn*$^{-/-}$ mice have a larger extracellular volume fraction under control conditions which might account for the higher $T2_{EV}$ measurements [163].

A limitation of using *Syn*$^{-/-}$ mice to understand AQP4 polarisation is that the distribution of the AQP4 molecular within the central nervous system (CNS) of mice is distinct from the human CNS. The concentration of the AQP4 water molecule localized to the BBI in the human brain is far reduced (~1/3) compared to the murine models [158, 165]. This would need to be a consideration when translating this technique from the murine brain to the human brain, as the changes may be more subtle. The kinetic perfusion model could be extended to be able to measure the water permeability surface (PS_w) independently from the capillary volume (V_c), instead of the exchange time as an index BBI water permeability, which may be a metric that could be more relevant for the human brain.

The design of the imaging protocol resulted in an average scan time ~ 3 hours 30 minutes due to the acquisition of two imaging slice and two inflow times. While this time is within the 4-hour limit for recovery protocol for the Home Office project license, it does not allow for any time for delays with the set-up or imaging acquisition. Inevitably, the physiology of the animal will begin to change over this period of time. It was noted that the respiration dropped from 120 to 70 bpm, on average, which is likely to be due to the prolonged effect of anesthetic during the scan, despite decreasing the delivered dose of isoflurane as the scan progressed. The use of different anesthetics should also be explored as this may also have an impact on the measurements [166, 167]. The orders of the acquisition of the slice position and the inflow times were randomized between animals to minimise the effect of artefacts from motion due to reduced respiration of the animals, as deep, slow breathing causes increased head motion of the animals. There were three to four animals from each group that were eliminated from the final analysis because the data had severe artefacts that may have been due to motion from deeper respiration due to the long scan time. In further studies, separate scan sessions could be used to acquire slices at different brain regions which should improve the quality of the data by reducing the variability in the animal physiology. However, this would introduce additional between-session variability which would need to be taken into consideration when designing the study.

Overall, this study highlights the complexity of cerebral dynamics in *in-vivo* models. In the human brain it is unlikely that the mislocalisation of AQP4 would be the only mechanism in pathology. In AD, the precise stage of disease progression when a reduction in AQP4 polarisation begins to occur is currently unknown. However, the aggregation of amyloid-β seems to further disrupt the anchoring of the AQP4 to the perivascular location [158]. Therefore, further studies using AD mouse model should be performed to relative the changes in AQP4 polarisation with disease progression.

5.5 Conclusion

To conclude, the multi-TE ASL technique is able to detect a reduction in BBI water permeability in the cerebellum region, but no alterations were found in the cortical brain region. Given that there was a significant difference in the cortical CBF, it highlights the potential impact of cerebral hemodynamics on the measures of water permeability via estimation of the exchange time. But, nonetheless this study illustrates the potential of measuring BBI permeability to water using multi-TE ASL techniques, as an index of AQP4 polarisation.

Chapter 6

Applying the Multiple Echo Time Arterial Spin Labelling Technique to a Mouse Model of Ageing

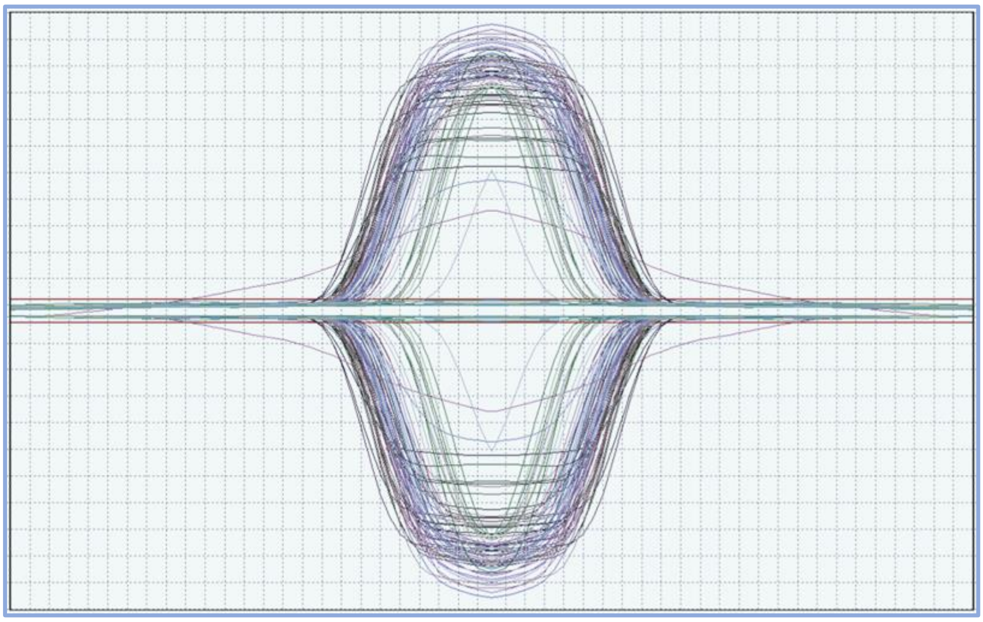

qRT-PCR curves, ageing mouse brain

Aim

There is a need for sensitive biomarkers that are able to predict poorer ageing, indicative of increased risk of neurodegeneration, leading to cognitive decline. There are many aspects of ageing that remain poorly understood, including dysfunction of blood brain interface (BBI) that results in changes of permeability which are linked to neurodegeneration in several conditions. Therefore, this chapter aims to investigate the potential changes in BBI permeability to water with ageing.

Currently, there are few non-invasive techniques that are able to assess BBI permeability, and hence the multi-TE ASL technique could be applied to the ageing brain to target water permeability across the BBI. Multi-TE ASL has proved to be sensitive to differences in aquaporin-4 (AQP4) expression at the BBI, and therefore it may also provide new insight into dysfunction of the BBI occurring with ageing that may affect BBI permeability to water. This work also aims to examine the expression profile of several components of the BBI such as the tight junctions, aquaporin-4 and pericytes, to give an insight into key components that may influence the rates of water permeability across the BBI in the aged mouse brain.

The aged mouse brain should be more representative of the changes that occur during ageing in the human brain, than the specific genetic mouse models used in the previous chapters (i.e. AQP4-deficient and α-syntrophin-deficient mice). This study aims to couple the non-contrast imaging measurements with invasive measures of the molecular components of the BBI to better understand the natural ageing processes that can be detected with multi-TE ASL technique, as a potential biomarker for neurodegenerative diseases such as Alzheimer’s Disease (AD) where ageing is the greatest risk factor.

6.1 Introduction

Normal ‘physiological’ ageing is inevitable, with the physical decline of the body including deterioration of the central nervous system (CNS) usually beginning in humans at around 40 years of age. However, the specific processes that render the aged brain more vulnerable to neurodegenerative disease are still poorly understood. There are many factors: genetic, biological and environmental, that can have an influence on the rate of cognitive decline. Ageing is currently the biggest risk factor for developing neurodegenerative disease, such as Alzheimer’s Disease (AD), but it is highly likely that ageing compounds the other risk factors resulting in the transition from normal physiological ageing to debilitating diseases that occur in the CNS [168, 169]. There are several changes that happen to the CNS during the ageing process including brain atrophy, slowing down of the nerve cell connections and accumulation of waste produces within the brain tissue [170, 171].

However, to my knowledge, thus far imaging techniques have not been able to detect significant changes to water permeability that occur with normal physiological ageing. The multiple-echo time (multi-TE) ASL technique, using endogenous water as a tracer, might enable the detection of non-disruptive BBI changes, such as alterations to the function of transporters, if the physical disruption to the BBI has not occurred. Brain imaging techniques such as CT, MRI and PET studies have been established to measure BBI permeability, crucially reporting additional spatial information about the barrier properties [67]. DCE-MRI techniques were able to measure an increase in BBI permeability in the hippocampus of mild cognitive impairment (MCI) patients [2] relative to age-match healthy controls and another study found that the extent of BBI leakage was correlated with the degree of cognitive impairment [3].

There are few studies assessing regional differences in permeability, though it is thought that certain brain regions, such as the hippocampus and limbic system, naturally show increased permeability in physiological conditions [2, 148, 172]. There is some speculation that these regions are more vulnerable to damage to the BBI leading to neurological deterioration. The application of non-invasive techniques to probe BBI water permeability in different brain regions would be a step towards brain-wide measurements when investigating permeability changes in diseased conditions.

There has been limited work assessing the molecular changes to the BBI which affect permeability to water. It has been shown that the deterioration of transmembrane TJ protein, occludin, is associated with an increase in water permeability [90]. The expression/ polarisation of aquaporin-4 (AQP4) has also been shown to play a significant role in mediating water flux into the brain parenchyma, presented in **Chapter 3** and **Chapter 5** [33, 147]. Therefore, it would be valuable to establish any changes that occur to the molecular components of the BBI, such as TJs, AQP4 water channels and pericytes during the ageing process. Together with non-invasive measurements of BBI permeability to water, this should provide insight into the driving mechanisms that induce changes to water permeability with ageing.

There are many transgenic mice models of AD, some of which have aggressive pathologies with a rapid temporal cascade that mimic an aggressive form of AD. Therefore, naturally aged mice may represent an alternative model of early neurodegenerative processes that occur in age-related cognitive decline [173]. Age-related loss of cognitive function has been widely characterised in animal studies with mice [174, 175]. Additionally, as mice age, amyloid-β (Aβ) plaques begin to aggregate within the brain with a formation pattern similar to that found in sporadic, late-onset AD (LOAD) which affects the majority of AD sufferers [173]. Aged mice (27 months old) are equivalent to the human age of around 70 years old – an age group who are at relatively high risk of developing LOAD. Thus, aged mice are a simple model of a brain vulnerable of developing sporadic forms of AD. An advantage of applying the multi-TE ASL technique to the mouse brain is that non-invasive *in-vivo* measurements can be acquired in a highly controlled environment, and be paired for a direct comparison with molecular information using immunochemical techniques brain regions of interest.

The present study aimed to assess BBI permeability to water using the multi-TE ASL technique in the cortical and cerebellar regions of the aged mouse brain. The expression profile of several components of the BBI of the aged mice was examined, to determine the age-related changes to the BBI that might be driving possible differences in water permeability.

6.2 Method

All experiments were performed in mice in accordance with the European Commission Directive 86/609/EEC (European Convention for the Protection of Vertebrate Animals used for Experimental and Other Scientific Purposes) and the United Kingdom Home Office (Scientific Procedures) Act (1986). All mice were acclimatised in an animal house, prior to data acquisition, with a 12 h light/12 h dark cycle with food and water provided *ad libitum*. Eight C57Bl/6JRj mice at 27 ± 1 months old (29.6 – 37.5g) and eleven C57Bl/6JRj mice at 7 ± 1 months old (30.1 - 35.7g) were used for assessing BBI permeability to water in the cortical brain region. For the cerebellum brain region, eight C57Bl/6JRj mice at 27 ± 1 months old and eight C57Bl/6JRj mice at 7 ± 1 months old were scanned from the same cohort of mice.

6.2.1 Imaging Protocol

The imaging protocol was designed to reduce the overall scan time compared to the previous study in **Chapter 5**, to ensure that the older mice, being possibly more fragile, would be physiologically stable for the duration of the scan. Therefore, the cortical slice and the cerebellum slice were taking in separate scan session. For each slice, two inflow times with the multi-TE ASL sequence from **Chapter 4: Method: Pilot Study of BBI Permeability to Water** and the multi-TI sequence using the protocol from **Chapter 5: Method: Experimental Protocol: Imaging Protocol**. The overall time required to scan a single slice was ~2h30 from initial anesthesia induction. Imaging a single slice allowed the targeted region to be in the isocenter of the magnet which helped to improve the quality of the EPI readout through localized shimming. All mice were recovered after the scan, and the second brain region (cerebellum) was scanned approximately one week later using the same routine.

The physiological monitoring of the animals, equipment set-up, and the imaging sequence parameters for the multi-TE and are outlined in **Chapter 4: Method: Pilot Study of BBI Permeability to Water** and the multi-TI protocols is outlined in **Chapter 5: Method: Experimental Protocol: Imaging Protocol**, however in this study the number of repetitions were increased to 10, as overall the same session was shorter for this single slice protocol. Animals were scanned in the same set-up position in the multi-TE and multi-TI sequence sequences.

6.2.2 Data Analysis

Mean ASL images were generated at each echo time, and this data was analysed using Matlab 2018a (Mathworks) and GraphPad (Prism 8) using the analysis pipeline (**Figure 6.1**) established in the previous **Chapter 2: Methods**, here incorporating the individual arterial transit times in the analysis pipeline. One data set of the cortical slice of an adult mice, one data set for the cerebellum slice of an adult mice and two data sets of the aged mice cerebellum slice were excluded from the final analysis due to severe artefacts in the images assessed by visual inspection of the images.

The cortical and cerebellum brain region were manually defined and the signal from the control data was extracted and fit to a mono-exponential decay model to estimate the extravascular tissue T2 ($T2_{EV}$). ASL signal was extracted from all data sets of each group and the analysis pipeline outlined in **Chapter 2: Method** and **Chapter 4: Methods: Data Analysis** generated individual IV and EV ASL signals, ΔM_{IV} and ΔM_{EV} respectively, along with a single group-wise $T2_{IV}$. The IV and EV ASL signal contributions were used to calculate the intravascular fraction $\left(\frac{\Delta M_{IV}}{\Delta M_{IV} + \Delta M_{EV}}\right)$. The separate short multi-TI data set was used to calculate the arterial transit time using the model outlined in the previous **Chapter 2: Theory, Arterial Transit Time Measurement**. The intravascular fraction and the arterial transit time were combined together to measure the tissue transit time, using the two-compartment kinetic perfusion model. Finally, the exchange time(T_{ex}^{w}) was measured by subtracting the arterial transit time from the tissue transit time, to give a surrogate index of BBI permeability to water.

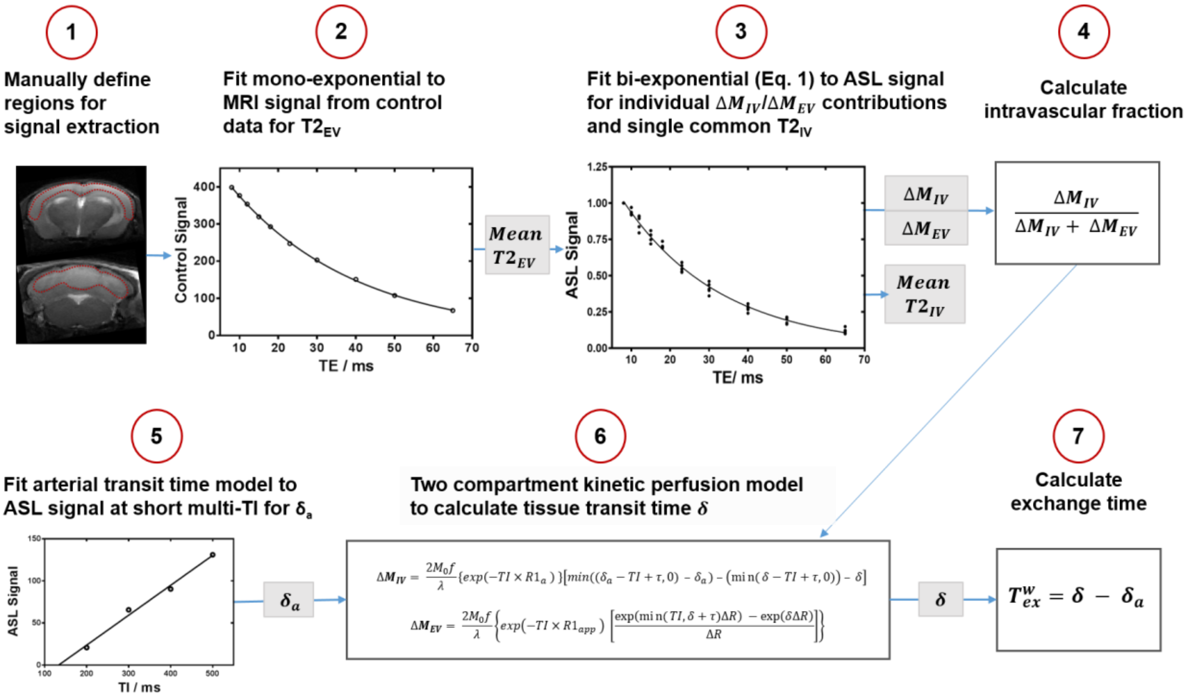

Figure 6.1: Analysis pipeline for exchange time (T_{ex}^{w}) calculation. Stepwise process outlining the modelling process using the ASL data to measure the exchange time (T_{ex}^{w}), from a defined region of interest, using the adapted two compartment kinetic perfusion model [93, 147] and the arterial transit time measurements.

Individual $T2_{IV}$ measurements were taken in the cortical brain region by performing a three parameter fit using the bi-exponential model on the individual ASL signal decay curves. A comparison of the precision and accuracy of the fitting parameters using the group-wise fitting compared to using the three-parameter fit for the individual animal is presented in **Chapter 6: Appendix: Two-compartment Model.**

Mean exchange time maps were generated for individual animals for visualisation purposes by manually segmenting the whole brain region from the imaging slice for each subject. A pixel-wise fitting of the ASL images across the range of echo times, using the two compartment model incorporating the individual $T2_{EV}$ maps, arterial transit time maps and the fixed shared $T2_{IV}$ for each age group. The resulting exchange time map was averaged across the two inflow times.

The cerebral blood flow (CBF) was determined using the general kinetic model outlined in **Chapter 4: Methods: Cerebral Blood Flow Quantification.**

6.2.3 Quantification of mRNA expression of molecular components of the blood-brain interface

mRNA expression levels of key structural and functional components of the BBI were quantified to better understand the driving factors that could be causing changes to BBI permeability to water in the aged mouse brain, measured with MRI. mRNA expression of aquaporin-4 water channels (*Aqp4*), α-syntrophin protein (*SNTA1)* for AQP4 polarisation, platelet-derived growth factor receptor-β (*Pdgfrβ)* (as a surrogate marker of pericyte coverage) and tight junction proteins occludin (*Occl)* and claudin-5 (*Cld-5)* was determined in the cortical and cerebellar brain region of seven C57Bl/6JRj mice at 27 ± 2 month old and seven C57Bl/6JRj at 7 ± 2 months old (same mice cohort used for BBI water permeability measurements). All mice were euthanised by overdose with intra-peritoneal injection of sodium pentobarbital (10 ml/kg), the brain was removed, hemisected, and the cortex dissected and snap frozen on dry ice.

Total RNA from each brain region was extracted using the protocol outlined in **Chapter 4, Methods: Quantification of *Aqp4* mRNA expression**. In this study, mRNA expression of *Aqp4, SNTA1, Pdgfrβ, Occl* and *Cld-5,* along with the reference housekeeper genes (*ACTB* and GAPDH) was quantified from the cDNA samples.

The same quantitative real-time polymerase chain reaction (qRT-PCR) thermocycle protocol, used was 2 mins at 55°C, 10 mins at 95°C and a two-step cycle of 15s at 95°C followed by 60s at 60°C which was repeated for 50 cycles. Each of the mRNA expression levels were determined using the $2^{-\Delta\Delta Ct}$ method [138] with the normalisation factor calculated based on the geometric mean between the two housekeeper genes, and internal normalisation determined from either the adult mice cortex or the adult mice cerebellum for the two brain regions.

6.2.4 Statistical Analysis

All data are reported as the mean and the associated error (± standard deviation). All of the statistical analysis was performed with GraphPad Prism 8 (GraphPad Software). A 2-way ANOVA with Bonferroni's multiple comparisons test was performed on the intravascular fraction and the $T2_{EV}$ to evaluate the dependence on i.) the inflow time and ii.) effect of the age between the adult and aged mice. For the parameters on which dependence on inflow time was not expected, exchange time, ATT and CBF, a two-tailed unpaired student's t-test was performed to compare effect of age between the adult and aged mice. A 2-way ANOVA with Bonferroni's multiple comparisons was performed to compare the difference in mRNA expression measurements between the adult and the aged mice. A two-tailed paired student's t-test was performed to compare the difference in regional exchange time between the cortical and cerebellar brain regions for the adult mice and the aged mice. For all tests, $p < 0.05$ was considered to be a statistically significant result.

6.3 Results

6.3.1 Cortical Brain Region

The ASL data from the cortical brain region is well described by a bi-exponential decay, **Figure 6.2A, B**. The intravascular fraction was measured to be 0.76 ± 0.12 for adult mice compared to 0.61 ± 0.08 for the aged mice at TI = 800 ms, (p = 0.018), with a similar decreasing trend for TI = 1500ms, where intravascular fraction is 0.28 ± 0.05 for adult mice compared to 0.22 ± 0.09 in the aged mice, p = 0.11 (**Figure 6.2C**). This indicates that the water is transferring into the tissue compartment more quickly in the aged mice, as there is less labelled vascular water in the intravascular compartment at a given inflow time.

Visual inspection of the exchange time maps showed a general decrease with age, **Figure 6.3A**. The mean cortical exchange time was 31% lower in the aged mice (335 ± 70 ms) relative to the adult mice (440 ± 75 ms), p = 0.017, **Figure 6.3B**. This reflects the faster rate of vascular water moving into the extravascular tissue in the aged mice, which is indicative of a change BBI permeability to water with ageing. To our knowledge, this is the first demonstration of changed BBI permeability with ageing measured using non-invasive techniques, which highlights the sensitivity of multi-TE ASL to probe differences to water permeability across the BBI.

There were no measurable differences in the arterial transit time in the cortical region of the mouse brain in the adult brain (100 ± 73 ms) relative to the aged brain (125 ± 31 ms), p = 0.38; **Figure 6.3C**. This suggests that the arterial vascular architecture is preserved at this age in the cortical region of the mouse brain. There are also no marked differences in the cerebral blood flow (CBF) measurements in aged mice, 188 ± 61 ml/100g/min, compared to the adult mice, 191 ± 71 ml/100g/min, indicating there to be consistent cortical haemodynamics as the mice age (p = 0.94). Often an increase in the measured EV fraction of the ASL signal is associated with a reduction in CBF [100, 102]; however, the equivalence of CBF in the two cohorts in the presence of significant differences in IV/EV signal fractions demonstrates the independence of these different measures.

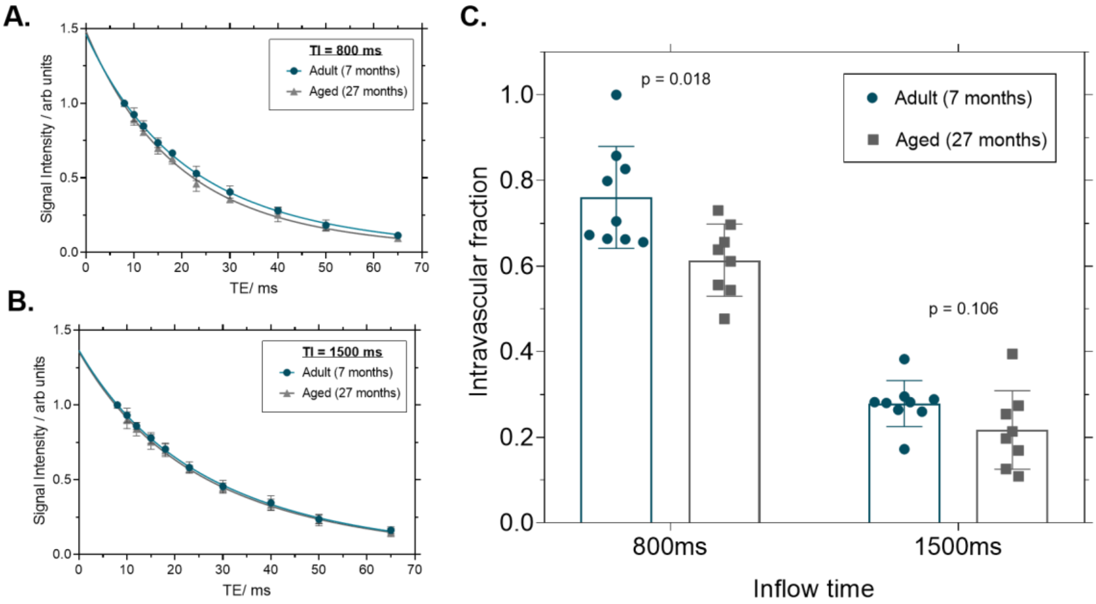

Figure 6.2: Mean cortical ASL signal intensity decay as a function of TE for the adult (blue) and aged (grey) across all mice **A.** TI = 800ms and **B.** TI = 1500ms. C. The intravascular fraction ($\Delta M_{IV} / \Delta M_{IV} + \Delta M_{EV}$) determined for the individual animal at both inflow times, mean and error (± std) and p-values are indicated on the plots.

The intravascular $T2_{IV}$ in the cortical region was measured at 13.5 ± 1.2 ms (TI = 800 ms) and 11.3 ± 4.1 ms (TI = 1500 ms) for the aged mice, compared to 20.6 ± 1.4 ms (TI = 800 ms) and 14.3 ± 4.0 ms (TI = 1500 ms) for the adult mice. Taking the $T2_{IV}$ measurements for individual mice, $T2_{IV}$ is 20.2 ± 5.7 ms at 800 ms and 11.8 ± 4.1 ms for adult mice and 14.6 ± 4.0 ms and 12.0 ± 6.8 ms for aged mice, at 800 ms and 1500 ms respectively for each age group, **Figure 6.4**. It is likely that the observed trend for decreasing $T2_{IV}$ with increasing inflow time is associated with the signal from the intravascular compartment being derived from further down the vasculature tree, from the larger arterioles toward the capillary bed, as the $T2_{IV}$ is an indicator of the level oxygenation in the vascular compartment [116]. Similarly, lower $T2_{IV}$ values in the aged mice may also suggest that oxygen extraction in this group is higher.

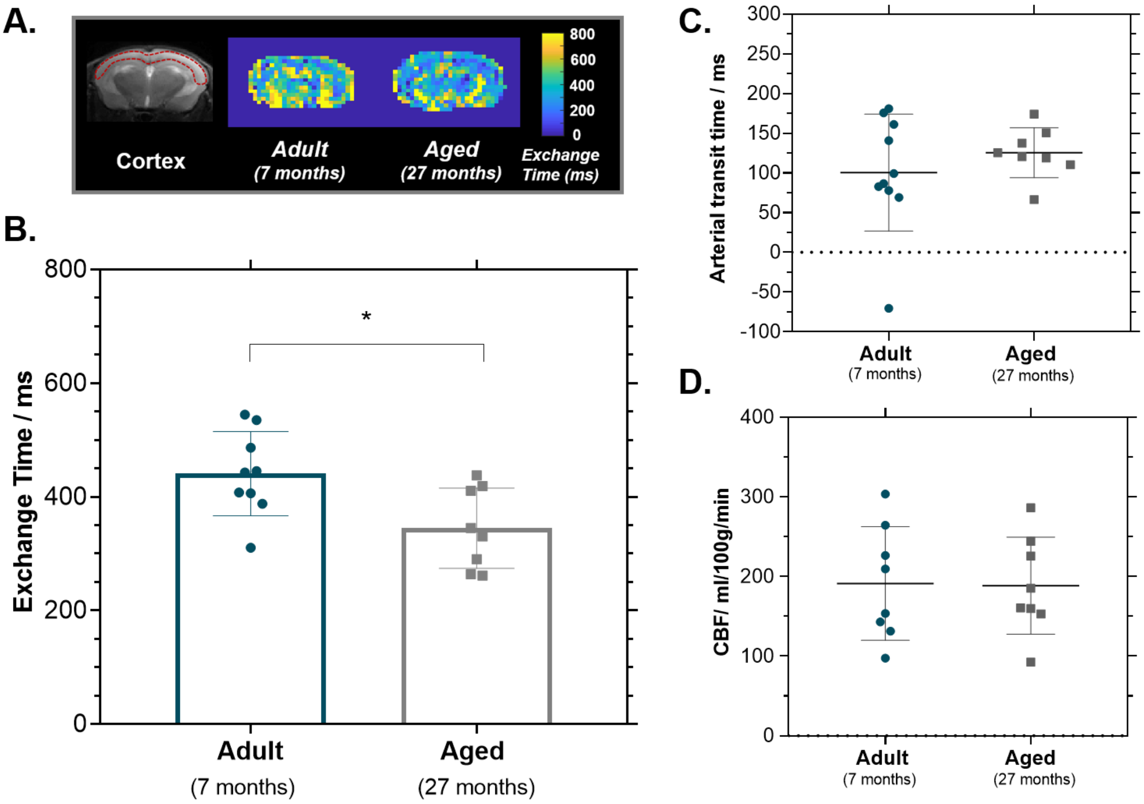

Figure 6.3: Cortical region measurements. **A.** Exchange time maps from a representative adult and aged mice, with an anatomical reference image on the left with the cortical ROI in red. **B.** Cortical exchange time measurements. **C.** Cortical arterial transit time measurements **D.** Cortical cerebral blood flow (CBF) measurements. Each plot shows individual animal measurements along with mean values and the associated error (± std). * indicating $p < 0.05$.

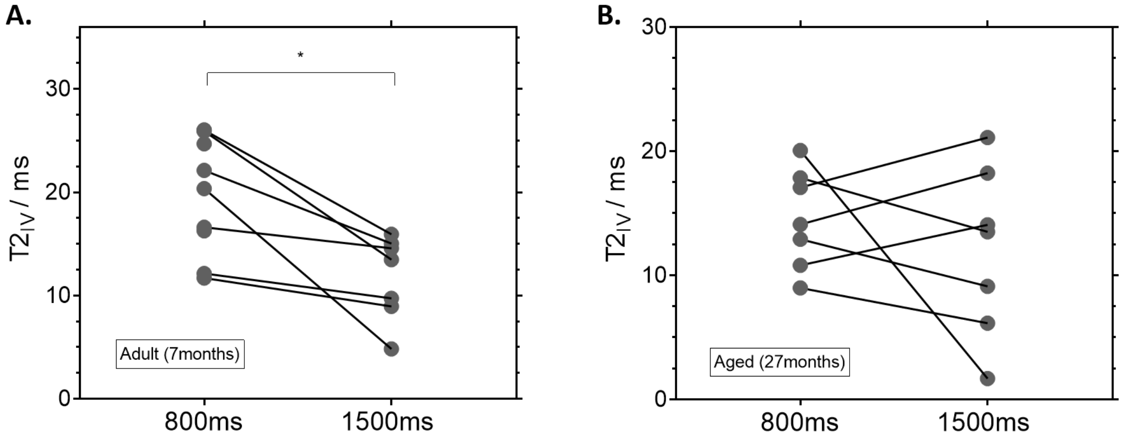

Figure 6.4: Intravascular T2 ($T2_{IV}$) measurements for individual mice at inflow times, 800 ms and 1500 ms **A.** Adult mice **B.** Aged mice. * indicates $p < 0.05$.

In the cortical brain tissue, $T2_{EV}$ was measured at 37.1 ± 1.6ms in the adult mice compared to 35.6 ± 1.5 ms in the aged mice at TI = 800ms, and $T2_{EV}$ was 34.5 ± 1.3 ms in the adult mice compared to 32.8 ± 1.6 ms in the aged mice at TI = 1500ms. Both the inflow time and the age of the mice resulted in a significant source of variation, $p = 0.0002$ and $p = 0.003$ respectively. The decrease in the extravascular tissue T2 with ageing might be related to the extravascular BOLD effect since there is a lower $T2_{IV}$ in the aged mice, also there could be the slight accumulation of iron within the cortical brain tissue with ageing [127].

There is generally an increase in mRNA expression of the measured components of the BBI in the cortex with ageing, **Figure 6.5**. There is an increase (2.1 ± 0.9 fold change) in the mRNA expression of AQP4 in the cortical region of the aged mice compared to the adult mice ($p = 0.083$). This might suggest that there is an increase in the capacity for AQP4-mediated transfer of water across the BBI in the ageing brain. However, there is a significant decrease (0.14 ± 0.09 fold change) in SNTA1 mRNA expression suggesting a down-regulation of the α-syntrophin protein in the ageing mouse brain ($p = 0.012$). The mRNA expression of *Pdgfrβ* also showed a significant increase (1.9 ± 0.4 fold) in the aged mice relative to the adult mice ($p = 0.015$), indicating that there is an upregulation of *Pdgfrβ* as mice age. There is a slight, though non-significant, increase in tight junction protein mRNA expression of occludin (1.4 ± 0.8 fold) and claudin-5 (1.5 ± 0.6 fold) in the aged mice compared to the adult controls, $p > 0.99$ and $p = 0.65$ respectively. This would suggest that the expression of these tight junction proteins is maintained fairly well during the ageing process in the mouse brain.

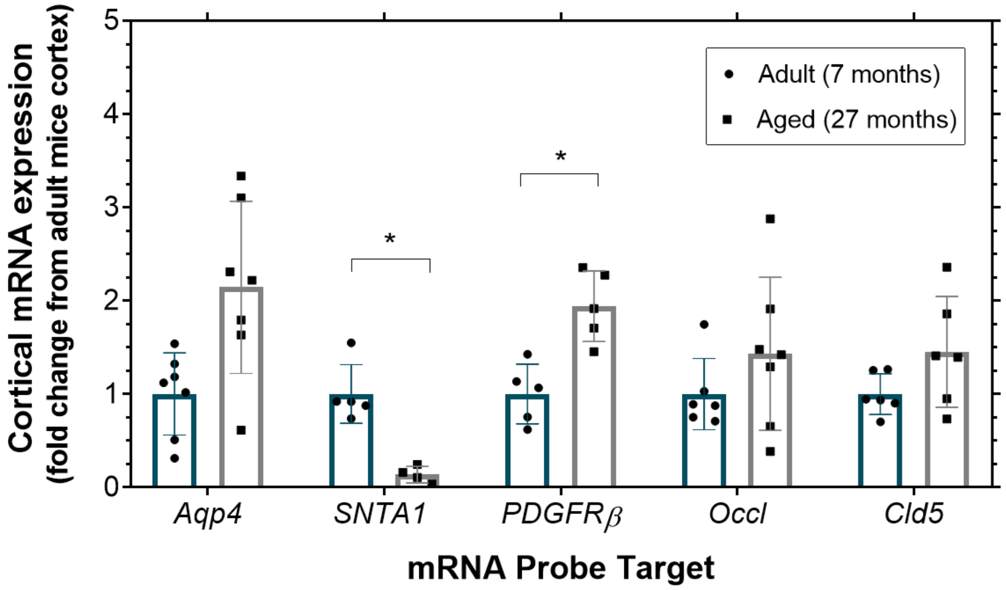

<u>Figure 6.5: Cortical mRNA expression</u> of aquaporin-4 (*Aqp4*), α-syntrophin protein (SNTA1), platelet derived growth factor receptor- β (PDGFRβ), occludin (*Occl*) and Claudin-5 (*Cld5*) with mean values and associated error (± std) displayed as fold change from the cortical region of the adult mice is shown on the plot. * indicates $p < 0.05$ for the adjusted p values.

6.3.2 Cerebellar Brain Region

The ASL signal decay derived from the cerebellum region in the brains of the adult and the aged mice show a good fit to the bi-exponential model at inflow times of 800ms and 1500ms, **Figure 6.6A, B**. The intravascular fraction was significantly lower with the increased inflow time at both age groups of the mice, ($p < 0.0001$), which again highlights the capacity of the technique's ability to detect the dynamics and exchange of the labelled vascular water in the cerebellum region. The intravascular fraction was measured at 0.82 ± 0.14 compared to 0.62 ± 0.15 at 800ms moving to 0.27 ± 0.15 compared to 0.31 ± 0.15 at TI = 1500 ms, in the adult and aged mice respectively (adjusted p values: $p = 0.035$ at 800ms and $p = 0.62$ at 1500ms), **Figure 6.6C**. The intravascular fraction was significantly lower in the aged mice compared to the adult mice at TI = 800 ms. However, when the inflow time is increased to 1500ms there was no significant difference in intravascular fraction with age, ($p = 0.62$).

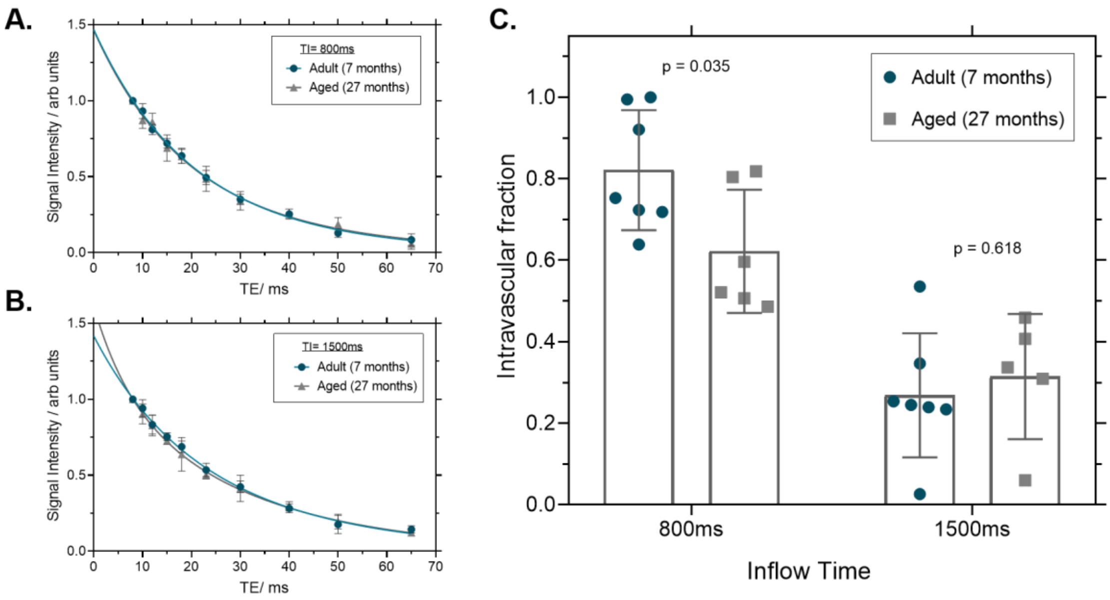

Figure 6.6: Mean cerebellar ASL signal intensity decay as a function of TE for the adult (blue) and aged (grey) across all mice, at inflow times: **A.** TI = 800ms and **B.** TI = 1500ms **C.** The intravascular fraction $(\Delta M_{IV} / \Delta M_{IV} + \Delta M_{EV})$ determined for the individual animal at both inflow times, mean and error (± std) and p-values are indicated on the plots.

The mean cerebellum exchange time was measured at 388 ± 133 ms in the aged mice compared to 366 ± 124 ms in the adult mice, p = 0.78, **Figure 6.7B**. The measurements indicate that there are no significant differences in the vascular water exchange across the BBI in the cerebellum region with ageing. This would suggest that vascular water transfer within the cerebellum is maintained in the ageing process.

The arterial transit time was significantly higher in the cerebellum region of the aged mice (156 ± 8 ms) compared to the adult mice (91 ± 38 ms), p = 0.006, **Figure 6.7C**. This may indicate that there is disruption to the arterial vascular supply to this brain region with ageing. The CBF measurements in the cerebellum brain region were 173 ± 94 ml/ 100g/ min in the aged mice and 173 ± 56 ml/100g/min in the adult mice, which would indicate that perfusion to this brain region is mantinained in the ageing mouse brain.

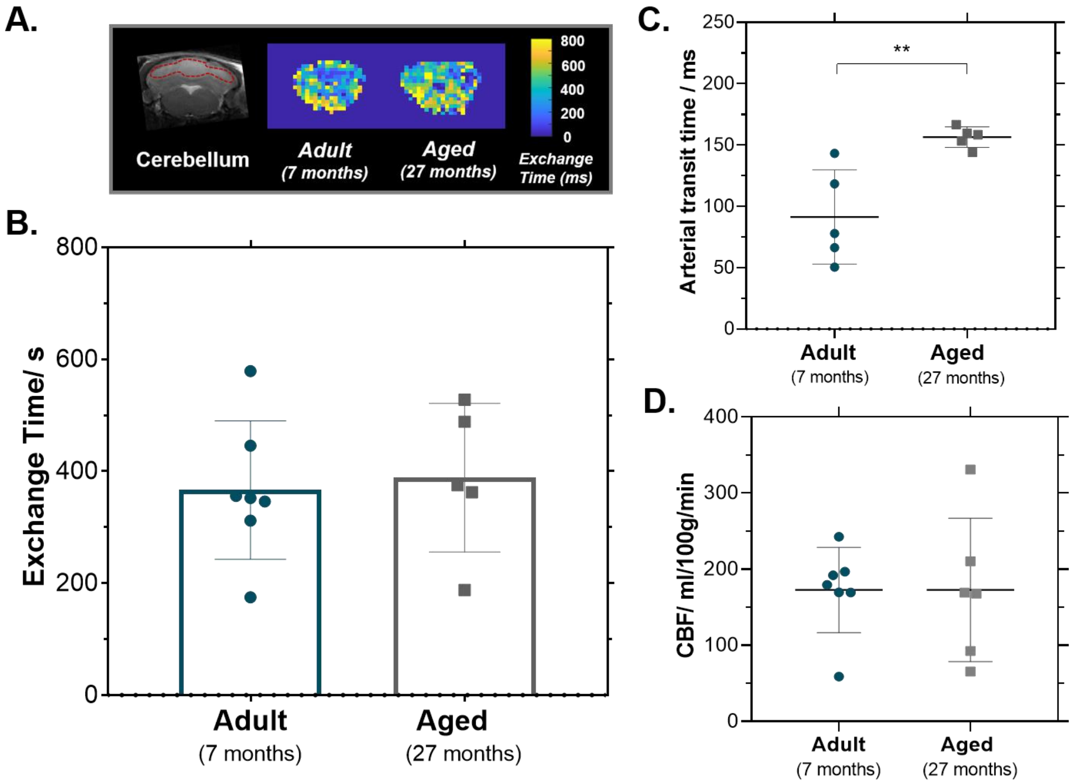

<u>Figure 6.7: Cerebellum measurements</u>. A. Exchange time maps for representative adult and aged mice with anatomical reference on left with ROI in red **B.** Exchange time measurements for individual adult mice and aged mice. **C.** Arterial transit time measurements for individual adult and aged mice **D.** Cerebellar CBF measurements for the individual adult and aged mice. For all plots, the mean value and the associated error (± std) are shown on plot. ** indicates p < 0.01.

The cerebellar tissue $T2_{EV}$ was measured at 33.2 ± 1.3ms and 32.5 ± 2.0 ms at TI = 800 ms, p = 0.480, and 29.4 ± 1.2 ms compared to 29.4 ± 0.8 ms at 1500ms, for adult mice and aged mice respectively at each inflow time. There was a significant inflow time dependent effect ($p < 0.0001$), but no significant differences were measured which respect to the age of the mice (p = 0.53). The intravascular $T2_{IV}$ was measured at 19.5 ± 1.5 ms and 16.4 ± 4.6 ms in the adult mice compared with 15.9 ± 4.5 ms and 6.7 ± 1.9 ms in the aged mice at TI = 800 ms and TI = 1500 ms respectively for each animal group. Similar to the cortical region, the aged mice exhibit a decrease in the intravascular T2 which may reflect a systemic decrease in blood oxygenation with ageing.

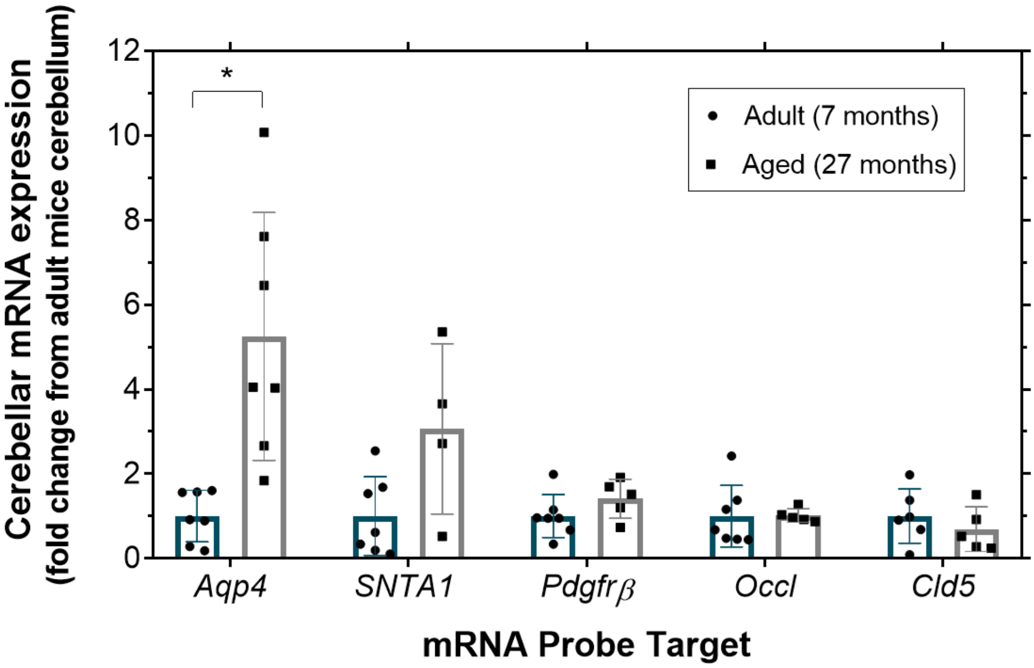

<u>Figure 6.8: Cerebellar mRNA expression</u> of aquaporin-4 (*Aqp4*), α-syntrophin protein (*SNTA1*), platelet derived growth factor receptor-β (*PDGFR-β*), occludin (*Occl*) and Claudin-5 (*Cld5*) in the individual adult mice and aged mice with mean values and associated error (± std) displayed as fold change from the cerebellar region of the adult mice is shown on the plot. * indicates $p < 0.05$ for adjusted p-values.

Overall, there were minimal measurable changes to the molecular components of the BBI in the cerebellum brain region. Except, the mRNA expression of *Aqp4* shows a marked 5.2 ± 2.9 fold increase in the aged mice relative to the adult mice ($p = 0.041$), which demonstrates that the expression of *Aqp4* is significantly upregulated in the cerebellum with ageing. There was also a 3.1 ± 2.0 fold increase in the mRNA expression of α-syntrophin protein (*SNTA1*) in the aged mouse brain, though not significant ($p = 0.65$) There is a slight, but not significant, increase in *Pdgfrβ* mRNA expression (1.4 ± 0.5 fold) in the aged mice compared to the adult control, ($p = 0.89$). The mRNA expression of the tight junction proteins, occludin and claudin-5, displayed no measureable differences in the aged mice with 1.0 ± 0.2 fold, ($p > 0.99$) and 0.7 ± 0.5 fold change, ($p > 0.99$) respectively. This would suggest that the expression of molecular components of the BBI in the cerebellum brain region remains fairly constant with ageing, except for AQP4, **Figure 6.9**.

6.4 Discussion

The multiple echo time (multi-TE) ASL technique was applied to the cortical and cerebellar brain regions of adult and aged mice to assess the BBB permeability to water, via estimates of the exchange time. The mean cortical exchange time was significantly (32%) lower in the aged mouse brain relative to the younger mouse brain, suggesting an increase in the vascular water flux into the extravascular cortical tissue. There is an increase in the mRNA expression of *Aqp4* water channels and *PDGRFβ*, a surrogate marker of pericytes, in the cortical region of the aged brain, which might account for the associated increase of water permeability. On the other hand, there were no measurable differences detected in the mean exchange time in the cerebellum region, despite an increase in AQP4 (but no changes in the other measured molecular components of the BBI). Taken together, this non-contrast technique is sensitive to certain molecular changes in the BBI that may be associated with a change in barrier function detected by an increased BBB permeability to water in the cortex of the ageing brain.

To my knowledge, this is the first demonstration of measurable changes in the BBI permeability to water in the ageing brain, detected using a non-invasive technique. Prior studies assessing BBI permeability in the ageing brain have used plasma/serum ratio (in human studies) and Evans Blue and histological assessment (in animal studies) that have, predominantly, only showed marked differences in BBI permeability with neurodegenerative pathology [67, 176, 177]. To date, non-invasive techniques were only able to detect non-significant trends in BBI permeability in the physiologically aged brain, except within the caudate nucleus using an advanced DCE-MRI technique [2, 176]. The lack of significant change to BBI permeability within the cortical region observed in previous studies may be due to the size of the gadolinium contrast agent (~92 kDa) and Evans Blue dye (~68 kDa) that are only sensitive to relatively gross defects occurring at the BBI. With multi-TE ASL, using labelled blood water (~18 Da) as the endogenous tracer, we are able to probe the natural ingress of the smaller water molecules into the brain tissue.

AQP4 water channels are central to the water transport mechanisms across the BBI, and our previous work demonstrates the contribution of AQP4 to the rate of BBI water permeability [147]. Studies suggest that increased expression of AQP4 is associated with the ageing process and becomes significantly enhanced in AD cases [51, 133, 178]. Here, in concordance with these previous observations, mRNA expression of AQP4 is ~2 fold greater in the cortical region of the aged mouse brain. Interestingly, there is also a significant decrease of the α-syntrophin protein (*SNTA1*), as index of the extent of AQP4 polarisation in the cortical region of the BBI. The reduction in AQP4 polarisation has been associated with ageing, and cognitive decline in AD, in previous studies [51, 133]. These data may suggest that AQP4 expression (or other factors), rather than AQP4 polarisation, would be the dominating contribution to an increase in BBI permeability to water with ageing. Yet, a significant (~5 fold) increase was also found in mRNA expression AQP4 in the cerebellum of the aged mice. In this brain region, there were no significant differences in the mRNA expression of SNTA1 or the cerebellar exchange time measurements, which would indicate that a combination of mechanisms play a role in the water flux across the BBI, and that there may be a regional dependency with ageing.

Several studies suggest that pericytes play an important role in the regulation of the BBI [21, 24]. Platelet-derived growth factor receptor-β (*PDGRβ*) is expressed exclusively on pericytes and smooth muscle cells (at a far lesser frequency), give a surrogate index of the pericyte coverage. In the present study, a ~2-fold increase in the cortical *PDGRβ* mRNA expression was recorded in the aged mouse brain, indicating that an upregulation of *PDGRβ* may occur with ageing. It has been proposed that increased expression of certain proteins including *PDGRβ* is indicative of pericytes changing from a stable resting state, where they surround the basement membrane of both endothelial cells and astrocytes, to a contractile stage when the BBI becomes disrupted [179]. This might suggest that the measured increased BBI water permeability in the present study may be closely related to changes in the pericytes, which have been shown to be an early indicator for change to the BBI leading to cognitive decline [10]. Indeed, recent studies by Zlokovic *et al.* reported an increase in soluble PDGRβ *(sPDGRβ*) in the CSF of individuals with mild cognitive impairment (MCI) [2]. The most recent work this group has found that the quantities of *sPDGRβ* measured in the CSF correlates the extent of cognitive decline in MCI patient [10]. Here, no changes are reported in the cerebellum exchange time measurement where there is also minimal difference in *PDGRβ* mRNA expression with ageing. Currently, there are no non-invasive techniques available to directly detect the degradation of pericytes. However, the multi-TE ASL technique could be applied to pericyte-deficient mice (*Pdgfrβ*$^{+/-}$) to further assess the effect of pericytes of BBI water permeability in different regions of the brain.

The transmembrane proteins, including occludin (*Occl)* and claudin-5 (*Cld5)*, form the TJs between the endothelium cells that play a key role in maintaining the integrity of the BBI. Breaks in the endothelial barrier are associated with a breakdown in TJs and have previously been reported in several studies of ageing using immunohistochemical techniques [176]. Here, the *Occl* and *Cld5* mRNA expression showed an increasing trend with ageing in the cortical region, though not significant, and show minimal difference in the cerebellum brain region. These results suggest there is no measurable difference in mRNA expression of TJ proteins, *Occl* and *Cld-5*. This might suggest that the aged mice do not yet have a physical breakdown to the TJs causing disrupted BBI. Other immunohistochemistry techniques, such as using fluorescence antibodies to identify breaks in the TJs, could be implemented to further assess the physical status of the TJs *in situ* within the BBI.

Altogether, there are several changes to the molecular composition of the BBI that could have an effect on the BBI water permeability. There is an upregulation of mRNA expression of AQP4 which might allow a more rapid exchange of labelled vascular water into the brain parenchyma. There is also an upregulation of *PDGRβ* with ageing in the cortical region, where an increase in BBI water permeability is present, but not the cerebellar brain region. This might suggest that a dysfunction to pericytes might be a key indicator for the change in BBI water permeability. Further studies, such as Western blots, could be performed to target the transition from mRNA expression to protein expression.

Permeability differences measured in AD patients, determined using DCE-MRI techniques via K^{trans} parameter, are typically one (or more) order of magnitude lower than permeability difference measured in brain tumours [4] or following intracerebral haemorrhage [5]. This highlights the necessity of implementing techniques with high sensitivity that have the capacity to detect the permeability differences that arise from ageing leading to MCI or AD. Despite the challenge of relatively small permeability changes in AD, the data presented here suggests that multi-TE ASL is able to detect difference in BBI permeability to water in cortical brain tissue of the aged mouse brain.

There were no detected differences in the arterial transit time (ATT) in the cortical brain region between the aged mouse and the adult mice, suggesting that arterial vascular dynamics in the cortex are preserved during the ageing process. The cortical ATT measurements presented in this study are consistent with previous ATT measurements in aged mice where there were no significant changes in the cortical region using a time-encoded ASL method [180]. In the present study, a significantly longer ATT was measured in the cerebellum region of the aged mice relative to the adult mice. The cortical brain region is supplied by the internal carotid arteries whereas the cerebellum region is supplied by the vertebral arteries which could affect the dynamics of the ATT [156]. This highlights the heterogeneity of vascular supply to different brain regions and the associated effects with ageing.

BBI breakdown causes the brain to be vulnerable to deleterious neurotoxins and pathogens passing into the brain parenchyma [20]. BBI damage leading to increased BBI permeability can be associated with circulatory and perfusion insufficiencies following degradation/detachment of pericytes surrounding the endothelium walls. This series of age-dependent physiological changes is thought to occur before neurodegeneration and cognitive decline [24]. Interestingly, in the present study there were no measurable differences in the CBF in either brain regions with ageing which might imply that the increased water permeability appears before CBF reductions with ageing begin to occur.

There are limited studies that have assessed regional BBI permeability heterogeneities across the brain. The cerebellum brain region has increased expression of *Aqp4* [151], and has previously been identified as a region with increased permeability via the ingress of Evans Blue dye [176]. In the present study, there are no measureable differences in BBI permeability in the cerebellum compared to the cortical region in both age groups, $p = 0.156$ for adult mice and $p = 0.452$ for the aged mice. This highlights that measurements using Evans Blue or using multi-TE ASL are likely to be targeting different vascular permeability pathways.

Previously, changes in BBI permeability in different brain regions have been observed in abnormal physiological conditions such as multiple sclerosis, epilepsy and ischemia [181, 182]. Therefore, it remains unclear whether increased BBB permeability causes certain brain regions to be more susceptible to pathology or whether other changes associated with particular pathology causes BBI breakdown. The multi-TE ASL technique is able to identify changes to the BBI water permeability in the normal ageing process, and therefore this technique might provide a platform that is able to better understand the precise aetiology of changes to BBI water permeability in brain disease.

The ASL signal derived from the cerebellum region shows a trend towards smaller intravascular fraction in the aged mice at TI = 800 ms relative to the adult mice. However, this observation was not conserved at TI = 1500 ms. However, the $T2_{IV}$ in the aged mice is very low (~7 ms), which suggests that a large fraction of the oxygen has been extracted from the vascular compartment at TI = 1500ms, and may even be capturing a venous T2 contribution. Further studies would be necessary to investigate the effects of a very low $T2_{IV}$ on the exchange time measurements and the robustness of the two-compartment kinetic perfusion model.

There is evidence to suggest that the hippocampus and the limbic system have leakier barrier properties in ageing which may make them more vulnerable to BBI breakdown, as measured by DCE-MRI [2, 172]. At present, the multi-TE ASL technique is not able to accurately spatially resolve the hippocampal region. However, future modifications to the imaging sequence or the position/orientation of the imaging slice may make it possible to distinguish smaller and deeper brain regions.

The aged mice used in this study were relatively old (27 months old) compared with the age of mice (14-18 months old) used in some other ageing studies [133, 173]. Research reports that mice at 14-18 months old are comparable age of an adult at 45-55 years old [183]. And mice at over 24 months old would representative of the human equivalent age (~75 years). This age represents the individuals who are at high risk of developing AD [184]. Human ageing studies are always limited by the population variation of physiological age vs real age, as well as the complication of co-existing pathologies. Some of these limitations might be similarly represented in the aged cohort of mice used in this study. Further experiments could be performed on these mice to better characterise the pathological hallmarks, such as amyloid burden/load, and behavioural changes through cognitive tests of mice at the age.

This study demonstrates the potential of the multi-TE ASL technique to detect increased BBI permeability to water in particular brain regions in ageing. This mouse model of ageing would lend itself well to longitudinal studies that could investigate the temporal deterioration of the BBI in both the functional BBI permeability. The multi-TE ASL could also be applied to MCI or AD models to probe the changes that occur in water permeability at the BBI in disease states.

Finally, BBI permeability to water may be a novel therapeutic target that could have the potential to ultimately, if therapeutic intervention was applied early enough, slow down cognitive deterioration. Drugs that are able to alter the vascular/glial compartment and reduce BBI permeability to water may have protective properties that could help to support regions that are most susceptible to BBI damage during the ageing process, and that make the brain vulnerable to an immune response leading to neurodegenerative decline.

6.5 Conclusion

In conclusion, the increase in BBI permeability to water in the cortical region of the ageing mouse brain demonstrates the capacity of the non-invasive imaging technique to detect BBI dysfunction with ageing. The increase in water permeability may be associated with the change in pericyte coverage and alterations in AQP4 expression and polarisation. The cerebellar region shows consistent BBI water permeability measures with ageing which may indicate that the permeability is maintained within this region during the ageing process and it may serve as a control region in future studies. This study demonstrates the scope of using multi-TE ASL to better understand the role of the BBI and water permeability, within different brain regions, with ageing.

6.6 Appendix: Two-Compartment Model

To assess the precision and accuracy of the model in its ability to estimate the parameters, data analysis for the two-compartment model was performed on GraphPad Prism 8.3 using a group-wise fitting of bi-exponential model with individual ΔM_{IV} and ΔM_{EV} values and a shared $T2_{IV}$. For individual animals the best-fit value ± 2σ (95% Confidence Interval (CI)) determined using a least-squares fit are presented in **Table 6.1.**

An individual fitting for each animal was also performed on the same data, this was to return individual values for ΔM_{IV} , ΔM_{EV} and $T2_{IV}$ with ± the best-fit value 2σ (95% CI) determined using a least-squares fit are presented in **Table 6.2.** In the cases where the fitting was unable to calculate a complete confidence interval ± inf has been used to indicate an ambiguous/unbound fitting.

The CIs are consistent across the group for the ΔM_{IV} and ΔM_{EV} values for the group-wise fitting in **Table 6.2**. For the individual animals the CI increases for the longer inflow time of 1500ms. This suggests that there is a reduced sensitivity in measuring the ASL-weighting signal compartments at the longer inflow time.

There is a larger variation in best-fit values for ΔM_{IV} and ΔM_{EV} for the 3-parameter fit for individual animals, compared to the shared fitting, presented **Table 6.2.** Though a best-fit value has been calculated for the individual animals, it was not possible to measure the CI for many of the individuals. This indicates that there is a lack of precision in the fitting for the individual animal, and with these data sets it is most appropriate to use the group-wise fitting to increase the precision of the fitting.

Animal ID	TI = 800 ms			TI = 1500 ms		
	ΔM_{IV}	ΔM_{EV}	Shared $T2_{IV}$ (ms)	ΔM_{IV}	ΔM_{EV}	Shared $T2_{IV}$ (ms)
1	0.95 ± 0.26	0.47 ± 0.22	20.6 ± 2.8	0.41 ± 0.33	0.97 ± 0.30	14.3 ± 8.0
2	0.91 ± 0.26	0.47 ± 0.22		0.39 ± 0.32	0.99 ± 0.30	
3	1.1 ± 0.26	0.28 ± 0.25		0.52 ± 0.36	0.85 ± 0.36	
4	1.2 ± 0.27	0.20 ± 0.22		0.39 ± 0.32	0.98 ± 0.29	
5	0.93 ± 0.25	0.44 ± 0.22		0.35 ± 0.32	1.0 ± 0.29	
6	1.5 ± 0.24	0.01 ± 0.35		0.35 ± 0.30	0.97 ± 0.26	
7	0.96 ± 0.26	0.47 ± 0.23		0.24 ± 0.27	1.1 ± 0.24	
8	1.0 ± 0.26	0.41 ± 0.23		0.39 ± 0.32	1.0 ± 0.29	
9	1.2 ± 0.27	0.25 ± 0.25		0.4 ± 0.36	0.98 ± 0.33	

Table 6.1: Best fit values ± 2σ (95% confidence interval (CI)) for the intravascular (ΔM_{IV}) and extravascular (ΔM_{EV}) ASL signal intensities for individual animals and shared intravascular transverse relaxation ($T2_{IV}$) across group at inflow time (TI) = 800ms and TI = 1500ms.

Animal ID	TI = 800 ms			TI = 1500 ms		
	ΔM_{IV}	ΔM_{EV}	$T2_{IV}$ (ms)	ΔM_{IV}	ΔM_{EV}	$T2_{IV}$ (ms)
1	1.4 ± inf	$4.2x10^{-5}$ ± inf	26.0 ± 6.3	0.42 ± 0.22	0.97 ± inf	13.5 ± 11.8
2	1.3 ± inf	$2.6x10^{-5}$ ± inf	26.0 ± inf	0.38 ± inf	0.98 ± inf	15.9. ± 11.0
3	0.84 ± 0.14	0.69 ± 0.20	12.2 ± 4.9	0.44 ± 0.21	1.0 ± 0.13	9.7 ± 6.3
4	1.0 ± 0.3	0.47 ± inf	16.6 ± 5.3	0.41 ± inf	0.95 ± inf	14.2 ± 12.1
5	0.72 ± 0.13	0.81 ± 0.16	11.7 ± 4.9	0.48 ± 1.02	1.0 ± inf	9.0 ± 14.4
6	1.1 ± 0.26	0.46 ± inf	16.3 ± 7.3	1.30. ± inf	$3.0x10^{-6}$ ± inf	28.7 ± inf
7	1.5 ± 0.45	$8.4x10^{-6}$ ± inf	20.4 ± 7.2	0.53 ± inf	1.1 ± inf	4.8 ± inf
8	1.4 ± 0.26	$3.2x10^{-7}$ ± inf	26.0 ± 3.8	~	~	~
9	1.1 ± inf	0.30 ± inf	22. 1 ± 6.3	0.46 ± inf	0.94 ± inf	15. 1 ± 11.5

Table 6.2: Best fit values ± 2σ (95% confidence interval (CI)) for the intravascular (ΔM_{IV}) and extravascular (ΔM_{EV}) ASL signal intensities and intravascular transverse relaxation ($T2_{IV}$) from a 3-parameter fit for individual animals at inflow time (TI) = 800ms and TI = 1500ms.

Chapter 7

Discussion & Future Work

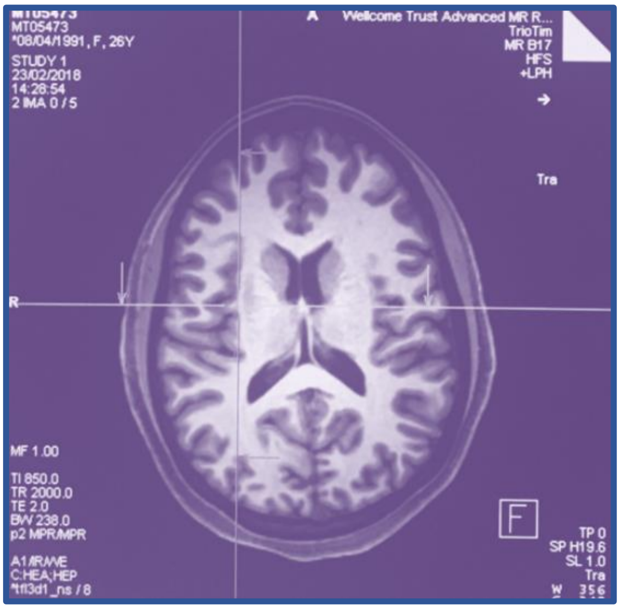

Anatomical MR image, human brain

7.1 Discussion

The aim of this thesis was to develop and implement a non-invasive multiple echo time (multi-TE) arterial spin labelled (ASL) technique to assess blood-brain interface (BBI) permeability to water within the mouse brain. The application of the technique in the mouse brain has enabled a rigorous *in-vivo* investigation of the biological components that influence BBI permeability to water, in highly controlled experimental conditions.

The application of the multi-TE ASL method to several mouse models has demonstrated the ability of the technique to measure both an increase and a reduction of BBI water permeability, in different conditions. It highlights the versatility of multi-TE ASL, using endogenous water as a tracer being sensitive to both conditions, as either a decrease or an increase in water permeability can be relevant to particular pathological processes. Many techniques are only sensitive to gross increases in BBI permeability to larger contrast agents that occur when there has been physical damage to the BBI. However, BBI disruption which is more localised to specific transporters, such as aquaporin-4 (AQP4), could lead to more subtle changes that might occur at relatively early time-points within particular neurodegenerative diseases.

In this work, the multi-TE ASL technique has been implemented in two high field 9.4T preclinical imaging systems with consistent estimates of BBI permeability to water. This provides evidence to support the validity and consistency of the technique within the mouse brain, even when using subtly different imaging protocols.

The mouse models used in the studies of this thesis have subtle phenotypic variation in their brain: the removal of AQP4, the reduction of AQP4 polarisation and normal physiological ageing. There were few measurable changes in the cerebral perfusion in these models. This may suggest that alterations to water permeability might occur ahead of changes to the cerebral blood flow (CBF) as the knockout mice and the aged mice may model aspects of the early stages of neurodegenerative disease, but further work will need to be performed to better understand the relationship between CBF and such non-invasive ASL based measures of BBI permeability to water.

Aquaporin-4 (AQP4) water channels have been a primary focus within this work because of the emerging evidence of their role in brain clearance pathways, such as the glymphatic system. A further motivation for targeting these water channels was the lack of non-invasive techniques that are sensitive to the function of AQP4. This work has demonstrated that the multi-TE ASL technique is sensitive to changes in AQP4 expression, as measured by a significant (31%) increase in the exchange time, as an index of BBI water permeability in AQP4-deficient mice. This result is in line with the hypothesised reduction in the intra-to-extravascular water transport pathways with the removal of AQP4 water channels. Recently, there have been other new studies corroborating the reduction in BBI permeability in AQP4-deficient mice using MRI techniques [185].

To further assess the sensitivity of the multi-TE ASL technique sensitivity to the polarisation of AQP4, the cortical and cerebellar brain regions of α-Syntrophin-deficient (*Syn*$^{-/-}$) mice, which have a reduction of AQP4 solely from at the astrocytic endfeet located facing the blood vessels, were used to measure BBI permeability to water. A lower BBI permeability was found in the *Syn*$^{-/-}$ mice compared to controls within the cerebellum region, but not in the cortex. A reduction in CBF of the *Syn*$^{-/-}$ mice was measured in the cortical region, which may be compensating for the lack of AQP4 channels at the BBI. This study highlights the regional heterogeneity within the brain, related to variations of AQP4 polarisation across different brain regions.

At present there is a lack of studies that have investigated regional differences in BBI permeability. MRI offers the capability of brain-wide measurements, however improvements in the MRI sequences must be implemented to improve the SNR to enable robust acquisitions in smaller brain regions, for example regions within the limbic system. In this work, there were consistent results from the cortical brain region and the technique was extended to the cerebellum due to the high expression of AQP4 within this brain region. However, no marked differences were found in the MRI measures of BBI water permeability between the cortical and the cerebellar brain region in WT animals. Other studies have reported there to be an increased permeability in white matter regions. Therefore, future studies could be performed at higher spatial resolution together with improvements to the analysis pipeline in registering the images to a mouse brain atlas to better differentiate the regions of grey matter and white matter. Technical improvements must also be implemented to obtain more robust measurements within white matter regions. Regional BBI water permeability measurements could be important, especially in neurodegenerative diseases that appear to preferentially affect specific brain regions such as the hippocampus. The acquisition of robust measurements in several different brain regions might be very useful, especially when translating the technique to the human brain. In particular, regions that consistently shows stable water permeability measures could act as a control/reference region to normalise water permeability in individuals to reduce inter-subject variability.

The two-compartment kinetic perfusion model brings limitations for the assessment of the BBI permeability to water. The first assumption is that the brain tissue consists of only two-compartments, and that the water transfer between other sub-compartments, such as between the plasma and the red-blood cells in the blood or the intracellular and extracellular compartments in the tissue, is very fast or an extremely small contribution. The second assumption of the exchange time measurements is that the labelled vascular water is solely moving into the extravascular tissue compartment. Emerging work from Hangzhang Lu’s group using phase-contrast ASL techniques would suggest that novel water permeability information can be acquired from the signal that has not been transferred into the tissue and can be detected in the sagittal sinus vein [105]. Extended theoretical frameworks might elucidate some novel findings from the multi-TE ASL data acquired in this work.

Finally, aged mice showed a 32% increase in BBI permeability to water in the cortical brain region when assessed using multi-TE ASL. The increased water permeability was also reflected by an increase in mRNA expression of AQP4 in the aged mouse brain. This points towards AQP4 having a role in increasing the water permeability. However, a larger increase in AQP4 mRNA expression was found in the cerebellum brain region of the aged mice but there were no significant changes in the BBI water permeability in this region. Interestingly, changes were also found in the pericyte marker, PDGFRβ, within the cortical region which has been previously shown to reflect dysfunction in the pericytes [186]. Multi-TE ASL could be applied to a pericyte-deficient mouse brain to better understand the role of pericytes in BBI water permeability and the potential importance of these changes with respect to the influence of AQP4. Further immunohistological tests could be performed to assess the deposition of amyloid-β in the ageing mouse brain.

Overall, this multi-TE ASL technique is sensitive to subtle changes to the BBI that are associated with water permeability. The work in this thesis demonstrates the potential of the non-invasive technique for clinical implementation to assess the potentially early pathological changes that may be present in those with neurodegenerative disease.

7.2 Future Work

The work presented in this thesis has demonstrated that the multi-TE ASL technique is able to detect both an increase and reduction in water permeability across the BBI that is associated with some of the biological mechanisms found in neurodegenerative conditions. The changes to water permeability that have been detected were subtle, due to the differences in the expression/polarisation of AQP4 and also with ageing, relative to the larger expected differences in other pathologies, such as stroke or brain tumours. Future investigation could characterise the changes to water permeability that are associated with a larger physical assault to the BBI or indeed, non-disruptive dysfunction caused by inflammation. There is also scope to characterising the evolution of a pathology longitudinally in mouse models, given the non-invasive and non-contrast aspect of this technique.

The studies presented here have highlighted that there is an association between AQP4 and the BBI water permeability measured using multi-TE ASL. Considering the emerging evidence of the role of the AQP4 in the glymphatic system, it would be interesting to explore the effects of altering the BBI integrity and the associated impact that it may have on the glymphatic function. It is likely that two pathways, BBI water permeability and the glymphatic system, may work in parallel, but this hypothesis is yet to be explored.

The multi-TE ASL technique, particularly with the protocol developed on the 9.4T Bruker system with the shorter echo time, shows novel results in consistently demonstrating that there is a reduction on $T2_{IV}$ when the inflow time is increased. Theoretically, the $T2_{IV}$ is derived from the vascular compartment and therefore the relaxation rate would be dependent on the oxygenation of the blood that contains the labelled water. The wild-type cohort in both the AQP4 polarisation study and also the adult mice in the ageing study show a marked decrease in the $T2_{IV}$ value with increased TI. This might reflect the oxygen extraction at various points along the vascular tree. If these measurements, taken at a range of inflow times, were coupled with invasive measurements of the local oxygenation, the relationship between the $T2_{IV}$ measurements with local tissue oxygenation could be robustly characterised. This raises the exciting possibility that the multi-TE ASL technique could have a further application as a non-invasive measurement of local oxygenation. It would also be of particular interest to apply this approach to probe different brain regions, such as the cerebellum, which appears to have extremely low blood oxygenation (low $T2_{IV}$ values) or high oxygen extraction.

Future work should focus on methods to validate the multi-TE ASL technique. This could be using ^{15}O-labelled water as a PET tracer to model the kinetics of the water permeability. It would be beneficial to implement a standard DCE-MRI technique alongside the multi-TE ASL protocol in the mice to assess BBI permeability to larger tracers, for example in the model of ageing. Further, there is motivation to implement a DW-ASL imaging protocol to measure BBI water permeability as a comparison between the multi-TE ASL technique developed in this work, given the emerging DW-ASL studies on the human brain.

Finally, there is much scope to implement these techniques on a 3T clinical scanner for application to the human brain which may benefit several patient groups. This work has demonstrated that this approach may be valuable for the early detection of neurodegenerative disease. It could also serve as tool to better understand neuromyelitis optica (NMO) spectrum disorder, an autoimmune disease that attacks the AQP4 channels within the optic nerve which remains poorly understood. It could also have application to assess the extent of injury of certain brain region following stroke. Overall, there are many pathologies could be probed using multi-TE ASL to assess water permeability across the BBI.

7.3 Final Summary

To conclude, the work in this thesis demonstrated that multi-TE ASL is a promising tool for probing the integrity and permeability of the BBI to water. The development of this technique for application to the mouse brain has enabled specific biological changes at the BBI to be assessed, particularly relating to subtle processes associated with ageing. These studies have highlighted that the technique is sensitive to AQP4 water channels which has implications in AD. Importantly, it is a non-invasive tool that shows potential for clinical translation for the early detection and understanding neurodegenerative disease.

References

1. Zlokovic, B.V., *Neurovascular pathways to neurodegeneration in Alzheimer's disease and other disorders.* Nat Rev Neurosci, 2011. **12**(12): p. 723-38.
2. Montagne, A., et al., *Blood-brain barrier breakdown in the aging human hippocampus.* Neuron, 2015. **85**(2): p. 296-302.
3. van de Haar, H.J., et al., *Blood-Brain Barrier Leakage in Patients with Early Alzheimer Disease.* Radiology, 2016. **281**(2): p. 527-535.
4. Larsson, H.B., et al., *Measurement of brain perfusion, blood volume, and blood-brain barrier permeability, using dynamic contrast-enhanced T(1)-weighted MRI at 3 tesla.* Magn Reson Med, 2009. **62**(5): p. 1270-81.
5. Aksoy, D., et al., *Magnetic resonance imaging profile of blood-brain barrier injury in patients with acute intracerebral hemorrhage.* J Am Heart Assoc, 2013. **2**(3): p. e000161.
6. Patterson, C., *World Alzheimer Report 2018* Alzheimer's Disease International, 2018.
7. Jack, C.R., Jr., et al., *Hypothetical model of dynamic biomarkers of the Alzheimer's pathological cascade.* Lancet Neurol, 2010. **9**(1): p. 119-28.
8. Jack, C.R., Jr., et al., *Tracking pathophysiological processes in Alzheimer's disease: an updated hypothetical model of dynamic biomarkers.* Lancet Neurol, 2013. **12**(2): p. 207-16.
9. Montagne, A., et al., *Brain imaging of neurovascular dysfunction in Alzheimer's disease.* Acta Neuropathol, 2016. **131**(5): p. 687-707.
10. Nation, D.A., et al., *Blood–brain barrier breakdown is an early biomarker of human cognitive dysfunction.* Nature Medicine, 2019. **25**(2): p. 270-276.
11. Cai, Z., et al., *Role of Blood-Brain Barrier in Alzheimer's Disease.* J Alzheimers Dis, 2018. **63**(4): p. 1223-1234.
12. Pun, P.B., J. Lu, and S. Moochhala, *Involvement of ROS in BBB dysfunction.* Free Radic Res, 2009. **43**(4): p. 348-64.
13. Erdő, F., L. Denes, and E. de Lange, *Age-associated physiological and pathological changes at the blood–brain barrier: A review.* Journal of Cerebral Blood Flow & Metabolism, 2016. **37**(1): p. 4-24.
14. Erdő, F., L. Denes, and E. de Lange, *Age-associated physiological and pathological changes at the blood-brain barrier: A review.* Journal of cerebral blood flow and metabolism : official journal of the International Society of Cerebral Blood Flow and Metabolism, 2017. **37**(1): p. 4-24.
15. Balda, M.S., et al., *Multiple domains of occludin are involved in the regulation of paracellular permeability.* Journal of Cellular Biochemistry, 2000. **78**(1): p. 85-96.
16. Furuse, M., et al., *Occludin: a novel integral membrane protein localizing at tight junctions.* J Cell Biol, 1993. **123**(6 Pt 2): p. 1777-88.
17. Greene, C., N. Hanley, and M. Campbell, *Claudin-5: gatekeeper of neurological function.* Fluids and barriers of the CNS, 2019. **16**(1): p. 3-3.
18. Nitta, T., et al., *Size-selective loosening of the blood-brain barrier in claudin-5-deficient mice.* J Cell Biol, 2003. **161**(3): p. 653-60.

19. Bauer, H.-C., et al., *"You Shall Not Pass"-tight junctions of the blood brain barrier.* Frontiers in neuroscience, 2014. **8**: p. 392-392.
20. Sweeney, M.D., A.P. Sagare, and B.V. Zlokovic, *Blood–brain barrier breakdown in Alzheimer disease and other neurodegenerative disorders.* Nature Reviews Neurology, 2018. **14**: p. 133.
21. Daneman, R., et al., *Pericytes are required for blood-brain barrier integrity during embryogenesis.* Nature, 2010. **468**(7323): p. 562-6.
22. Bell, R.D. and B.V. Zlokovic, *Neurovascular mechanisms and blood–brain barrier disorder in Alzheimer's disease.* Acta Neuropathologica, 2009. **118**(1): p. 103-113.
23. Armulik, A., et al., *Pericytes regulate the blood-brain barrier.* Nature, 2010. **468**(7323): p. 557-61.
24. Bell, R.D., et al., *Pericytes control key neurovascular functions and neuronal phenotype in the adult brain and during brain aging.* Neuron, 2010. **68**(3): p. 409-27.
25. Abbott, N.J., L. Rönnbäck, and E. Hansson, *Astrocyte–endothelial interactions at the blood–brain barrier.* Nature Reviews Neuroscience, 2006. **7**(1): p. 41-53.
26. Agre, P., et al., *Aquaporin water channels--from atomic structure to clinical medicine.* J Physiol, 2002. **542**(Pt 1): p. 3-16.
27. Mathiisen, T.M., et al., *The perivascular astroglial sheath provides a complete covering of the brain microvessels: an electron microscopic 3D reconstruction.* Glia, 2010. **58**(9): p. 1094-103.
28. Nagelhus, E.A., et al., *Aquaporin-4 Water Channel Protein in the Rat Retina and Optic Nerve: Polarized Expression in Müller Cells and Fibrous Astrocytes.* The Journal of Neuroscience, 1998. **18**(7): p. 2506-2519.
29. Abbott, N.J., *Evidence for bulk flow of brain interstitial fluid: significance for physiology and pathology.* Neurochem Int, 2004. **45**(4): p. 545-52.
30. Sykova, E. and C. Nicholson, *Diffusion in brain extracellular space.* Physiol Rev, 2008. **88**(4): p. 1277-340.
31. Manley, G.T., et al., *Aquaporin-4 deletion in mice reduces brain edema after acute water intoxication and ischemic stroke.* Nat Med, 2000. **6**(2): p. 159-63.
32. Papadopoulos, M.C., et al., *Aquaporin-4 facilitates reabsorption of excess fluid in vasogenic brain edema.* Faseb j, 2004. **18**(11): p. 1291-3.
33. Nagelhus, E.A. and O.P. Ottersen, *Physiological Roles of Aquaporin-4 in Brain.* Physiological Reviews, 2013. **93**(4): p. 1543-1562.
34. Ma, T., et al., *Generation and phenotype of a transgenic knockout mouse lacking the mercurial-insensitive water channel aquaporin-4.* The Journal of clinical investigation, 1997. **100**(5): p. 957-962.
35. Fan, Y., et al., *Sex- and region-specific alterations of basal amino acid and monoamine metabolism in the brain of aquaporin-4 knockout mice.* J Neurosci Res, 2005. **82**(4): p. 458-64.
36. Haj-Yasein, N.N., et al., *Glial-conditional deletion of aquaporin-4 (Aqp4) reduces blood-brain water uptake and confers barrier function on perivascular astrocyte endfeet.* Proc Natl Acad Sci U S A, 2011. **108**(43): p. 17815-20.

37. Papadopoulos, M.C. and A.S. Verkman, *Aquaporin water channels in the nervous system.* Nature Reviews Neuroscience, 2013. **14**(4): p. 265-277.
38. Papadopoulos, M.C. and A.S. Verkman, *Aquaporin-4 Gene Disruption in Mice Reduces Brain Swelling and Mortality in Pneumococcal Meningitis.* Journal of Biological Chemistry, 2005. **280**(14): p. 13906-13912.
39. Filippidis, A., R. Carozza, and H. Rekate, *Aquaporins in Brain Edema and Neuropathological Conditions.* International Journal of Molecular Sciences, 2016. **18**(1): p. 55.
40. Banks, W.A., et al., *Lipopolysaccharide-induced blood-brain barrier disruption: roles of cyclooxygenase, oxidative stress, neuroinflammation, and elements of the neurovascular unit.* J Neuroinflammation, 2015. **12**: p. 223.
41. Zhao, Z., et al., *Establishment and Dysfunction of the Blood-Brain Barrier.* Cell, 2015. **163**(5): p. 1064-1078.
42. Varatharaj, A. and I. Galea, *The blood-brain barrier in systemic inflammation.* Brain Behav Immun, 2017. **60**: p. 1-12.
43. Banks, W.A., et al., *Lipopolysaccharide-induced blood-brain barrier disruption: roles of cyclooxygenase, oxidative stress, neuroinflammation, and elements of the neurovascular unit.* Journal of Neuroinflammation, 2015. **12**(1): p. 223.
44. Erickson, M.A., et al., *Lipopolysaccharide impairs amyloid beta efflux from brain: altered vascular sequestration, cerebrospinal fluid reabsorption, peripheral clearance and transporter function at the blood-brain barrier.* J Neuroinflammation, 2012. **9**: p. 150.
45. Iliff, J.J., et al., *A Paravascular Pathway Facilitates CSF Flow Through the Brain Parenchyma and the Clearance of Interstitial Solutes, Including Amyloid* Science Translational Medicine, 2012. **4**(147): p. 147ra111-147ra111.
46. Jessen, N.A., et al., *The Glymphatic System: A Beginner's Guide.* Neurochemical Research, 2015. **40**(12): p. 2583-2599.
47. Mestre, H., et al., *Aquaporin-4 dependent glymphatic solute transport in rodent brain.* bioRxiv, 2017.
48. Iliff, J.J., et al., *Brain-wide pathway for waste clearance captured by contrast-enhanced MRI.* Journal of Clinical Investigation, 2013. **123**(3): p. 1299-1309.
49. Plog, B.A. and M. Nedergaard, *The Glymphatic System in Central Nervous System Health and Disease: Past, Present, and Future.* Annu Rev Pathol, 2017.
50. Silberstein, C., et al., *Membrane organization and function of M1 and M23 isoforms of aquaporin-4 in epithelial cells.* Am J Physiol Renal Physiol, 2004. **287**(3): p. F501-11.
51. Zeppenfeld, D.M., et al., *Association of Perivascular Localization of Aquaporin-4 With Cognition and Alzheimer Disease in Aging Brains.* JAMA Neurology, 2017. **74**(1): p. 91.
52. Amiry-Moghaddam, M., et al., *An alpha-syntrophin-dependent pool of AQP4 in astroglial end-feet confers bidirectional water flow between blood and brain.* Proc Natl Acad Sci U S A, 2003. **100**(4): p. 2106-11.
53. Vindedal, G.F., et al., *Removal of aquaporin-4 from glial and ependymal membranes causes brain water accumulation.* Mol Cell Neurosci, 2016. **77**: p. 47-52.

54. Govindpani, K., et al., *Vascular Dysfunction in Alzheimer's Disease: A Prelude to the Pathological Process or a Consequence of It?* J Clin Med, 2019. **8**(5).
55. Iturria-Medina, Y., et al., *Early role of vascular dysregulation on late-onset Alzheimer's disease based on multifactorial data-driven analysis.* Nat Commun, 2016. **7**: p. 11934.
56. Ujiie, M., et al., *Blood-brain barrier permeability precedes senile plaque formation in an Alzheimer disease model.* Microcirculation, 2003. **10**(6): p. 463-70.
57. Saunders, N.R., et al., *The rights and wrongs of blood-brain barrier permeability studies: a walk through 100 years of history.* Front Neurosci, 2014. **8**: p. 404.
58. Bechmann, I., I. Galea, and V.H. Perry, *What is the blood-brain barrier (not)?* Trends Immunol, 2007. **28**(1): p. 5-11.
59. Goldmann, E.E., *Die aussere und innere Sekretion des gesunden und kranken Organismus im Liche der "vitalen Farbung".* Beitr. Klin. Chir., 1909. **64**: p. 192-265.
60. Goldmann, E., *Vitalfärbungen am Zentralnervensystem. Beitrag zur Physiologie des Plexus choroideus und der Hirnhäute.* Hirschwald, Berlin, 1913.
61. Lee, S., et al., *Real-time in vivo two-photon imaging study reveals decreased cerebro-vascular volume and increased blood-brain barrier permeability in chronically stressed mice.* Scientific reports, 2018. **8**(1): p. 13064-13064.
62. Cho, E.E., et al., *Two-Photon Fluorescence Microscopy Study of Cerebrovascular Dynamics in Ultrasound-Induced Blood—Brain Barrier Opening.* Journal of Cerebral Blood Flow & Metabolism, 2011. **31**(9): p. 1852-1862.
63. Dong, X., *Current Strategies for Brain Drug Delivery.* Theranostics, 2018. **8**(6): p. 1481-1493.
64. Crone, C. and S.P. Olesen, *Electrical resistance of brain microvascular endothelium.* Brain Res, 1982. **241**(1): p. 49-55.
65. Jamieson, J.J., et al., *Role of iPSC-derived pericytes on barrier function of iPSC-derived brain microvascular endothelial cells in 2D and 3D.* Fluids and Barriers of the CNS, 2019. **16**(1): p. 15.
66. Katt, M.E., et al., *The role of mutations associated with familial neurodegenerative disorders on blood–brain barrier function in an iPSC model.* Fluids and Barriers of the CNS, 2019. **16**(1): p. 20.
67. Farrall, A.J. and J.M. Wardlaw, *Blood-brain barrier: ageing and microvascular disease--systematic review and meta-analysis.* Neurobiol Aging, 2009. **30**(3): p. 337-52.
68. Mecocci, P., et al., *Blood-brain-barrier in a geriatric population: barrier function in degenerative and vascular dementias.* Acta Neurologica Scandinavica, 1991. **84**(3): p. 210-213.
69. Cortes-Canteli, M., et al., *Fibrinogen and altered hemostasis in Alzheimer's disease.* Journal of Alzheimer's disease : JAD, 2012. **32**(3): p. 599-608.
70. Cortes-Canteli, M., et al., *Fibrinogen and beta-amyloid association alters thrombosis and fibrinolysis: a possible contributing factor to Alzheimer's disease.* Neuron, 2010. **66**(5): p. 695-709.

71. Starr, J.M., et al., *Blood–brain barrier permeability in Alzheimer's disease: a case–control MRI study.* Psychiatry Research: Neuroimaging, 2009. **171**(3): p. 232-241.
72. Weiss, N., et al., *The blood-brain barrier in brain homeostasis and neurological diseases.* Biochimica et Biophysica Acta (BBA) - Biomembranes, 2009. **1788**(4): p. 842-857.
73. Piert, M., et al., *Diminished glucose transport and phosphorylation in Alzheimer's disease determined by dynamic FDG-PET.* J Nucl Med, 1996. **37**(2): p. 201-8.
74. Syvänen, S. and J. Eriksson, *Advances in PET imaging of P-glycoprotein function at the blood-brain barrier.* ACS chemical neuroscience, 2013. **4**(2): p. 225-237.
75. Nakamura, Y., et al., *Development of a Novel Ligand, [11C]TGN-020, for Aquaporin 4 Positron Emission Tomography Imaging.* ACS Chemical Neuroscience, 2011. **2**(10): p. 568-571.
76. Avsenik, J., S. Bisdas, and K.S. Popovic, *Blood-brain barrier permeability imaging using perfusion computed tomography.* Radiol Oncol, 2015. **49**(2): p. 107-14.
77. Bisdas, S., et al., *Computed Tomography Assessment of Cerebral Perfusion Using a Distributed Parameter Tracer Kinetics Model: Validation with H2(15)O Positron Emission Tomography Measurements and Initial Clinical Experience in Patients with Acute Stroke.* Journal of Cerebral Blood Flow & Metabolism, 2007. **28**(2): p. 402-411.
78. Barnes, S.R., et al., *Optimal acquisition and modeling parameters for accurate assessment of low Ktrans blood-brain barrier permeability using dynamic contrast-enhanced MRI.* Magnetic resonance in medicine, 2016. **75**(5): p. 1967-1977.
79. Tofts, P.S. and A.G. Kermode, *Measurement of the blood-brain barrier permeability and leakage space using dynamic MR imaging. 1. Fundamental concepts.* Magn Reson Med, 1991. **17**(2): p. 357-67.
80. Patlak, C.S., R.G. Blasberg, and J.D. Fenstermacher, *Graphical evaluation of blood-to-brain transfer constants from multiple-time uptake data.* J Cereb Blood Flow Metab, 1983. **3**(1): p. 1-7.
81. Heye, A.K., et al., *Tracer kinetic modelling for DCE-MRI quantification of subtle blood-brain barrier permeability.* Neuroimage, 2016. **125**: p. 446-455.
82. Sourbron, S.P. and D.L. Buckley, *Tracer kinetic modelling in MRI: estimating perfusion and capillary permeability.* Phys Med Biol, 2012. **57**(2): p. R1-33.
83. Ewing, J.R., et al., *Model selection in magnetic resonance imaging measurements of vascular permeability: Gadomer in a 9L model of rat cerebral tumor.* J Cereb Blood Flow Metab, 2006. **26**(3): p. 310-20.
84. Schwarzbauer, C., et al., *Quantitative magnetic resonance imaging of capillary water permeability and regional blood volume with an intravascular MR contrast agent.* Magnetic Resonance in Medicine, 1997. **37**(5): p. 769-777.
85. Rooney, W.D., et al., *Mapping human brain capillary water lifetime: high-resolution metabolic neuroimaging.* NMR in biomedicine, 2015. **28**(6): p. 607-623.

86. Anderson, V.C., et al., *The blood-brain barrier and microvascular water exchange in Alzheimer's disease.* Cardiovascular psychiatry and neurology, 2011. **2011**: p. 615829-615829.
87. Kim, Y.R., et al., *In vivo quantification of transvascular water exchange during the acute phase of permanent stroke.* Magnetic Resonance in Medicine, 2008. **60**(4): p. 813-821.
88. Donahue, K.M., R.M. Weisskoff, and D. Burstein, *Water diffusion and exchange as they influence contrast enhancement.* Journal of Magnetic Resonance Imaging, 1997. **7**(1): p. 102-110.
89. Huang, S., et al., *Cerebral blood volume affects blood-brain barrier integrity in an acute transient stroke model.* J Cereb Blood Flow Metab, 2013. **33**(6): p. 898-905.
90. Dickie, B.R., et al., *Water-exchange MRI detects subtle blood-brain barrier breakdown in Alzheimer's disease rats.* Neuroimage, 2018. **184**: p. 349-358.
91. Gulani, V., et al., *Gadolinium deposition in the brain: summary of evidence and recommendations.* The Lancet Neurology. **16**(7): p. 564-570.
92. Detre, J.A., et al., *Perfusion imaging.* Magn Reson Med, 1992. **23**(1): p. 37-45.
93. Alsop, D.C. and J.A. Detre, *Reduced transit-time sensitivity in noninvasive magnetic resonance imaging of human cerebral blood flow.* J Cereb Blood Flow Metab, 1996. **16**(6): p. 1236-49.
94. Zhou, J., et al., *Two-compartment exchange model for perfusion quantification using arterial spin tagging.* J Cereb Blood Flow Metab, 2001. **21**(4): p. 440-55.
95. Parkes, L.M. and P.S. Tofts, *Improved accuracy of human cerebral blood perfusion measurements using arterial spin labeling: accounting for capillary water permeability.* Magn Reson Med, 2002. **48**(1): p. 27-41.
96. Wang, J., et al., *When Perfusion Meets Diffusion: in vivo Measurement of Water Permeability in Human Brain.* Journal of Cerebral Blood Flow & Metabolism, 2006. **27**(4): p. 839-849.
97. St Lawrence, K.S., J.A. Frank, and A.C. McLaughlin, *Effect of restricted water exchange on cerebral blood flow values calculated with arterial spin tagging: a theoretical investigation.* Magn Reson Med, 2000. **44**(3): p. 440-9.
98. Zhao, Z.A., et al., *Perivascular AQP4 dysregulation in the hippocampal CA1 area after traumatic brain injury is alleviated by adenosine A2A receptor inactivation.* Sci Rep, 2017. **7**(1): p. 2254.
99. Kety, S.S., *The theory and applications of the exchange of inert gas at the lungs and tissues.* Pharmacol Rev, 1951. **3**(1): p. 1-41.
100. Silva, A.C., D.S. Williams, and A.P. Koretsky, *Evidence for the Exchange of Arterial Spin-Labeled Water with Tissue Water in Rat Brain from Diffusiom-Sensitized Measurements of Perfusion.* Magnetic Resonance in Medicine, 1999. **38**: p. 232-237.
101. Shao, X., et al., *Mapping water exchange across the blood–brain barrier using 3D diffusion - prepared arterial spin labeled perfusion MRI.* Magnetic Resonance in Medicine, 2018.

102. Kim, T. and S.-G. Kim, *Quantification of cerebral arterial blood volume using arterial spin labeling with intravoxel incoherent motion-sensitive gradients.* Magnetic Resonance in Medicine, 2006. **55**(5): p. 1047-1057.
103. Duong, T.Q. and S.G. Kim, *In vivo MR measurements of regional arterial and venous blood volume fractions in intact rat brain.* Magn Reson Med, 2000. **43**(3): p. 393-402.
104. Wengler, K., et al., *3D MRI of whole-brain water permeability with intrinsic diffusivity encoding of arterial labeled spin (IDEALS).* Neuroimage, 2019. **189**: p. 401-414.
105. Lin, Z., et al., *Non-contrast MR imaging of blood-brain barrier permeability to water.* Magn Reson Med, 2018.
106. Lin, Z., et al. *Imaging disruption of blood-brain-barrier (BBB) in Mild Cognitive Impairment with using contrast agent*. in *International Society for Magnetic Resonance in Medicine* 2018. Paris, France.
107. Liu, P., J. Uh, and H. Lu, *Determination of spin compartment in arterial spin labeling MRI.* Magnetic Resonance in Medicine, 2011. **65**(1): p. 120-127.
108. Gregori, J., et al., *T2-based arterial spin labeling measurements of blood to tissue water transfer in human brain.* Journal of Magnetic Resonance Imaging, 2013. **37**(2): p. 332-342.
109. Wells, J.A., et al., *Measuring Biexponential Transverse Relaxation of the ASL Signal at 9.4 T to Estimate Arterial Oxygen Saturation and the Time of Exchange of Labeled Blood Water into Cortical Brain Tissue.* Journal of Cerebral Blood Flow & Metabolism, 2013. **33**(2): p. 215-224.
110. Wells, J.A., et al., *MRI of cerebral micro-vascular flow patterns: A multi-direction diffusion-weighted ASL approach.* Journal of Cerebral Blood Flow & Metabolism, 2016. **37**(6): p. 2076-2083.
111. Sperling, R.A., et al., *Toward defining the preclinical stages of Alzheimer's disease: recommendations from the National Institute on Aging-Alzheimer's Association workgroups on diagnostic guidelines for Alzheimer's disease.* Alzheimers Dement, 2011. **7**(3): p. 280-92.
112. Yang, J., et al., *Loss of astrocyte polarization in the tg-ArcSwe mouse model of Alzheimer's disease.* J Alzheimers Dis, 2011. **27**.
113. Xu, Z., et al., *Deletion of aquaporin-4 in APP/PS1 mice exacerbates brain Aβ accumulation and memory deficits.* Molecular Neurodegeneration, 2015. **10**(1): p. 58.
114. Koretsky, A.P., *Early development of arterial spin labeling to measure regional brain blood flow by MRI.* Neuroimage, 2012. **62**(2): p. 602-7.
115. Jezzard, P., M.A. Chappell, and T.W. Okell, *Arterial spin labeling for the measurement of cerebral perfusion and angiography.* J Cereb Blood Flow Metab, 2017: p. 271678x17743240.
116. Lee, S.P., et al., *Diffusion-weighted spin-echo fMRI at 9.4 T: microvascular/tissue contribution to BOLD signal changes.* Magn Reson Med, 1999. **42**(5): p. 919-28.
117. Wells, J.A., et al., *The importance of RF bandwidth for effective tagging in pulsed arterial spin labeling MRI at 9.4T.* NMR in Biomedicine, 2012. **25**(10): p. 1139-1143.

118. McRobbie D. W. and Moore E. A., *MRI From Picture to Proton* ed. 2nd. 2006 Cambridge University Press.
119. Buxton, R.B., *Quantifying CBF with arterial spin labeling.* J Magn Reson Imaging, 2005. **22**(6): p. 723-6.
120. Wells, J.A., et al., *In vivo imaging of tau pathology using multi-parametric quantitative MRI.* Neuroimage, 2015. **111**: p. 369-78.
121. Buxton, R.B., et al., *A general kinetic model for quantitative perfusion imaging with arterial spin labeling.* Magn Reson Med, 1998. **40**(3): p. 383-96.
122. Wang, J., et al., *Comparison of quantitative perfusion imaging using arterial spin labeling at 1.5 and 4.0 Tesla.* Magnetic Resonance in Medicine, 2002. **48**(2): p. 242-254.
123. Herscovitch, P. and M.E. Raichle, *What is the correct value for the brain--blood partition coefficient for water?* J Cereb Blood Flow Metab, 1985. **5**(1): p. 65-9.
124. Dobre, M.C., K. Ugurbil, and M. Marjanska, *Determination of blood longitudinal relaxation time (T1) at high magnetic field strengths.* Magn Reson Imaging, 2007. **25**(5): p. 733-5.
125. Vazquez, A.L., et al., *Changes in cerebral arterial, tissue and venous oxygenation with evoked neural stimulation: implications for hemoglobin-based functional neuroimaging.* J Cereb Blood Flow Metab, 2010. **30**(2): p. 428-39.
126. Kara, F., et al., *In vivo measurement of transverse relaxation time in the mouse brain at 17.6 T.* Magn Reson Med, 2013. **70**(4): p. 985-93.
127. Pirpamer, L., et al., *Determinants of iron accumulation in the normal aging brain.* Neurobiol Aging, 2016. **43**: p. 149-55.
128. St. Lawrence, K.S., D. Owen, and D.J.J. Wang, *A two-stage approach for measuring vascular water exchange and arterial transit time by diffusion-weighted perfusion MRI.* Magnetic Resonance in Medicine, 2012. **67**(5): p. 1275-1284.
129. Tiwari, Y.V., et al., *Magnetic resonance imaging of blood–brain barrier permeability in ischemic stroke using diffusion-weighted arterial spin labeling in rats.* Journal of Cerebral Blood Flow & Metabolism, 2016: p. 0271678X1667338.
130. Akaike, H., *A new look at the statistical model identification.* IEEE Transactions on Automatic Control, 1974. **19**(6): p. 716-723.
131. Chen, J.-Q., et al., *Effects of Aquaporin 4 Knockdown on Brain Edema of the Uninjured Side After Traumatic Brain Injury in Rats.* Medical Science Monitor : International Medical Journal of Experimental and Clinical Research, 2016. **22**: p. 4809-4819.
132. Manley, G.T., et al., *New insights into water transport and edema in the central nervous system from phenotype analysis of aquaporin-4 null mice.* Neuroscience, 2004. **129**(4): p. 983-91.
133. Kress, B.T., et al., *Impairment of paravascular clearance pathways in the aging brain.* Ann Neurol, 2014. **76**(6): p. 845-61.
134. MacAulay, N. and T. Zeuthen, *Water transport between CNS compartments: contributions of aquaporins and cotransporters.* Neuroscience, 2010. **168**(4): p. 941-956.

135. Tait, M.J., et al., *Water movements in the brain: role of aquaporins.* Trends in Neurosciences, 2008. **31**(1): p. 37-43.
136. Amiry-Moghaddam, M., et al., *An α-syntrophin-dependent pool of AQP4 in astroglial end-feet confers bidirectional water flow between blood and brain.* Proceedings of the National Academy of Sciences, 2003. **100**(4): p. 2106-2111.
137. Thrane, A.S., et al., *Critical role of aquaporin-4 (AQP4) in astrocytic Ca2+ signaling events elicited by cerebral edema.* Proc Natl Acad Sci USA, 2011. **108**(2): p. 846-51.
138. Livak, K.J. and T.D. Schmittgen, *Analysis of relative gene expression data using real-time quantitative PCR and the 2(-Delta Delta C(T)) Method.* Methods, 2001. **25**(4): p. 402-8.
139. Amiry-Moghaddam, M. and O.P. Ottersen, *The molecular basis of water transport in the brain.* Nature Reviews Neuroscience, 2003. **4**(12): p. 991-1001.
140. Saadoun, S., et al., *AQP4 gene deletion in mice does not alter blood-brain barrier integrity or brain morphology.* Neuroscience, 2009. **161**(3): p. 764-72.
141. Badaut, J., et al., *Brain water mobility decreases after astrocytic aquaporin-4 inhibition using RNA interference.* J Cereb Blood Flow Metab, 2011. **31**(3): p. 819-31.
142. Nedergaard, M., *Neuroscience. Garbage truck of the brain.* Science, 2013. **340**(6140): p. 1529-30.
143. Palomares, J.A., et al., *Water Exchange across the Blood-Brain Barrier in Obstructive Sleep Apnea: An MRI Diffusion-Weighted Pseudo-Continuous Arterial Spin Labeling Study.* Journal of Neuroimaging, 2015. **25**(6): p. 900-905.
144. Wang, J., et al., *Diffusion-Weighted Perfusion MRI: Initial Experience in Application to Brain Tumor* Proc 15th Intl Soc Mag Reson Med, 2007: p. 2974.
145. Xie, L., et al., *Sleep drives metabolite clearance from the adult brain.* Science, 2013. **342**.
146. Ewing, J.R., Y. Cao, and J. Fenstermacher, *Single-coil arterial spin-tagging for estimating cerebral blood flow as viewed from the capillary: relative contributions of intra- and extravascular signal.* Magn Reson Med, 2001. **46**(3): p. 465-75.
147. Ohene, Y., et al., *Non-invasive MRI of brain clearance pathways using multiple echo time arterial spin labelling: an aquaporin-4 study.* NeuroImage, 2019. **188**: p. 515-523.
148. Wilhelm, I., et al., *Heterogeneity of the blood-brain barrier.* Tissue Barriers, 2016. **4**(1): p. e1143544.
149. He, X., M.E. Raichle, and D.A. Yablonskiy, *Transmembrane dynamics of water exchange in human brain.* Magn Reson Med, 2012. **67**(2): p. 562-71.
150. Hoddevik, E.H., et al., *Factors determining the density of AQP4 water channel molecules at the brain-blood interface.* Brain structure & function, 2017. **222**(4): p. 1753-1766.
151. Hubbard, J.A., et al., *Expression of the Astrocyte Water Channel Aquaporin-4 in the Mouse Brain.* ASN Neuro, 2015. **7**(5): p. 175909141560548.

152. Motulsky, H. and R. E Brown, *Detecting Outliers When Fitting Data With Nonlinear Regression—a New Method Based on Robust Nonlinear Regression and the False Discovery Rate*. Vol. 7. 2006.

153. Hladky, S.B. and M.A. Barrand, *Fluid and ion transfer across the blood–brain and blood–cerebrospinal fluid barriers; a comparative account of mechanisms and roles.* Fluids and Barriers of the CNS, 2016. **13**(1): p. 19.

154. Thulborn, K.R., et al., *Oxygenation dependence of the transverse relaxation time of water protons in whole blood at high field.* Biochim Biophys Acta, 1982. **714**(2): p. 265-70.

155. Vaishnavi, S.N., et al., *Regional aerobic glycolysis in the human brain.* Proc Natl Acad Sci U S A, 2010. **107**(41): p. 17757-62.

156. Dorr, A., J.G. Sled, and N. Kabani, *Three-dimensional cerebral vasculature of the CBA mouse brain: a magnetic resonance imaging and micro computed tomography study.* Neuroimage, 2007. **35**(4): p. 1409-23.

157. Aoki, K., et al., *Enhanced expression of aquaporin 4 in human brain with infarction.* Acta Neuropathol, 2003. **106**(2): p. 121-4.

158. Smith, A.J. and A.S. Verkman, *The "glymphatic" mechanism for solute clearance in Alzheimer's disease: game changer or unproven speculation?* Faseb j, 2017.

159. Neely, J.D., et al., *Syntrophin-dependent expression and localization of Aquaporin-4 water channel protein.* Proc Natl Acad Sci U S A, 2001. **98**(24): p. 14108-13.

160. Amiry-Moghaddam, M., et al., *Delayed K+ clearance associated with aquaporin-4 mislocalization: Phenotypic defects in brains of -syntrophin-null mice.* Proceedings of the National Academy of Sciences, 2003. **100**(23): p. 13615-13620.

161. Ismail, O., *Investigating Glymphatic Function in Alzheimer's Disease Pathology* in *Centre for Advanced Biomedical Imaging*. 2019, UCL.

162. Adams, M.E., et al., *Absence of alpha-syntrophin leads to structurally aberrant neuromuscular synapses deficient in utrophin.* J Cell Biol, 2000. **150**(6): p. 1385-98.

163. Dmytrenko, L., et al., *The Impact of Alpha-Syntrophin Deletion on the Changes in Tissue Structure and Extracellular Diffusion Associated with Cell Swelling under Physiological and Pathological Conditions.* PLOS ONE, 2013. **8**(7): p. e68044.

164. Wong, S.M., et al., *Blood-brain barrier impairment and hypoperfusion are linked in cerebral small vessel disease.* Neurology, 2019. **92**(15): p. e1669-e1677.

165. Eidsvaag, V.A., et al., *Human and mouse cortical astrocytes differ in aquaporin-4 polarization toward microvessels.* Glia, 2017. **65**(6): p. 964-973.

166. Gakuba, C., et al., *General Anesthesia Inhibits the Activity of the "Glymphatic System".* Theranostics, 2018. **8**(3): p. 710-722.

167. Munting, L.P., et al., *Influence of different isoflurane anesthesia protocols on murine cerebral hemodynamics measured with pseudo-continuous arterial spin labeling.* NMR in Biomedicine, 2019. **32**(8): p. e4105.

168. Phipps, L. *Risk Factors*. Alzheimer's Disease 2019 May 2018 [cited 2019 27/07/2019]; Available from: https://www.alzheimersresearchuk.org/about-dementia/types-of-dementia/alzheimers-disease/risk-factors/.

169. Hebert, L.E., et al., *Alzheimer disease in the United States (2010-2050) estimated using the 2010 census.* Neurology, 2013. **80**(19): p. 1778-83.

170. Morris, J.C. and D.Q. McManus, *The neurology of aging: normal versus pathologic change.* Geriatrics, 1991. **46**(8): p. 47-8, 51-4.

171. Shigenaga, M.K., T.M. Hagen, and B.N. Ames, *Oxidative damage and mitochondrial decay in aging.* Proc Natl Acad Sci U S A, 1994. **91**(23): p. 10771-8.

172. Ivanidze, J., et al., *Dynamic Contrast-Enhanced MRI Reveals Unique Blood-Brain Barrier Permeability Characteristics in the Hippocampus in the Normal Brain.* American Journal of Neuroradiology, 2019. **40**(3): p. 408-411.

173. Ahlemeyer, B., et al., *Endogenous Murine Amyloid-beta Peptide Assembles into Aggregates in the Aged C57BL/6J Mouse Suggesting These Animals as a Model to Study Pathogenesis of Amyloid-beta Plaque Formation.* J Alzheimers Dis, 2018. **61**(4): p. 1425-1450.

174. Forster, M.J., et al., *Age-related losses of cognitive function and motor skills in mice are associated with oxidative protein damage in the brain.* Proceedings of the National Academy of Sciences of the United States of America, 1996. **93**(10): p. 4765-4769.

175. Fahlstrom, A., H. Zeberg, and B. Ulfhake, *Changes in behaviors of male C57BL/6J mice across adult life span and effects of dietary restriction.* Age (Dordr), 2012. **34**(6): p. 1435-52.

176. Goodall, E.F., et al., *Age-associated changes in the blood-brain barrier: comparative studies in human and mouse.* Neuropathology and Applied Neurobiology, 2018. **44**(3): p. 328-340.

177. Bors, L., et al., *Age-dependent changes at the blood-brain barrier. A Comparative structural and functional study in young adult and middle aged rats.* Brain Research Bulletin, 2018. **139**: p. 269-277.

178. Moftakhar, P., et al., *Aquaporin expression in the brains of patients with or without cerebral amyloid angiopathy.* J Neuropathol Exp Neurol, 2010. **69**.

179. Yao, Y., et al., *Astrocytic laminin regulates pericyte differentiation and maintains blood brain barrier integrity.* Nat Commun, 2014. **5**: p. 3413.

180. Hirschler, L., et al., *Transit time mapping in the mouse brain using time-encoded pCASL.* NMR in Biomedicine: p. e3855-n/a.

181. van Vliet, E.A., et al., *Longitudinal assessment of blood-brain barrier leakage during epileptogenesis in rats. A quantitative MRI study.* Neurobiol Dis, 2014. **63**: p. 74-84.

182. Cavaglia, M., et al., *Regional variation in brain capillary density and vascular response to ischemia.* Brain Res, 2001. **910**(1-2): p. 81-93.

183. Hagen, C. *When are mice considered old?* The Jackson Laboratory 2017 [cited 2019 24/04/2019]; Available from: https://www.jax.org/news-and-insights/jax-blog/2017/november/when-are-mice-considered-old.

184. Alz.org. *Cause and Risk factors*. 2019 [cited 2019 1/06/2019]; Available from: https://www.alz.org/alzheimers-dementia/what-is-alzheimers/causes-and-risk-factors.

185. Zhang, Y., et al., *Increased cerebral vascularization and decreased water exchange across the blood-brain barrier in aquaporin-4 knockout mice.* PLOS ONE, 2019. **14**(6): p. e0218415.

186. Sengillo, J.D., et al., *Deficiency in Mural Vascular Cells Coincides with Blood–Brain Barrier Disruption in Alzheimer's Disease.* Brain Pathology, 2013. **23**(3): p. 303-310.